INVESTIGATION OF COMPOSITE MATERIALS USING DIGITAL VOLUME CORRELATION

ABHINAV GOYAL

A THESIS SUBMITTED TO THE FACULTY OF GRADUATE STUDIES IN PARTIAL FUFILLMENT OF THE REQUIREMENTS FOR THE DEGREE OF MASTER OF APPLIED SCIENCE

Graduate Program in Mechanical Engineering

York University

Toronto, Ontario

December 2022

ii Abstract

Composites are growing at a rapid pace for its use in industry such as automobiles because of its high strength to weight ratio and better damage tolerance than traditional materials. The composite structure is non-homogenous and anisotropic. The mechanical behavior of the microstructure is complex under loading. The traditional measurement technique such as strain gauge and extensometer provide limited information. Therefore, to understand the internal structure under loading conditions, there is a need for full field internal displacement and strain field. Digital Volume Correlation (DVC) is a measurement technique which generates a 3D displacement and strain field for the sample under loading. Fused filament fabrication (FFF) and hybrid braided composites has limited research to understand the microstructure behavior non-destructively. Therefore, thesis will explore the application of DVC on FFF and Hybrid braided composites under tensile loading.

iii Acknowledgement

Words cannot express my gratitude to my supervisor Dr. Garrett Melenka, for providing me the opportunity to pursue my graduate studies at York University. His invaluable patience and guidance helped me develop my research skills. His “open door policy” has always helped me to reach out him at any odd hours of the day. I would like to thank him for being a role model and grateful to have him as my supervisor.

Next, I would like to thank all my labmates and technicians in mechanical engineering department for providing me the technical support on different machines in the lab. Also, their innumerable advice would be helpful in every point of my life.

Lastly, I would like to dedicate the thesis to my parents for their constant support and sacrifice for me to achieve my ambitions.

iv Table of Contents

v List of Tables

vi List of Figures

vii List of Abbreviations

2D	Two Dimensional
2D DIC	2D Digital Image Correlation
3D	Three Dimensional
3D DIC	3D Digital Image Correlation
ABS	Acrylonitrile Butadiene Styrene
ALDVC	Adaptive Lagrangian Digital Volume Correlation
AM	Additive Manufacturing
CAD	Computer Aided Design
CC	Cross Correlation
CCD	Charged Couple Device
CF	Carbon Fibre
CLPT	Classical Laminate Plate Theory
CMC	Ceramic Matrix Composite
CMOS	Complementary Metal Oxide Semiconductor
CT	Computed Tomography
Cu	Copper
DSLR	Digital Single-Lens Reflex
DVC	Digital Volume Correlation
FEA	Finite Element Analysis
FFF	Fused Filament Fabrication

FIDVC	Fast-Iterative Digital Volume Correlation
FOV	Field Of View
Micro-CT	Micro-Computed Tomography
MMC	Metal Matrix Composite
MRI	Magnetic Resonance Imaging
MTS	Material Testing Stage
NCC	Normalized Cross Correlation
PDMS	Polydimethylsiloxane
PLA	Polylactic Acid
PMC	Polymer Matrix Composite
ROI	Region of Interest
VOI	Volume of Interest
ZNCC	Zero-Normalized Cross Correlation

viii List of Variables

θ	Angle
µ	Micro
%	Percentage
ε	Strain
ρ_1	Void Density
σ	Stress
ν	Poisson Ratio
[A]	Extensional Stiffness Matrix
[B]	Coupling Stiffness Matrix
$[C^G]$	Stiffness Averaging Equation
[D]	Bending Stiffness Matrix
d	Diameter
E	Strain tensor
f	fibre
F	Force
$\bar{F}$	Reference Image Normalized Greyscale Intensity
$F(x_i, y_i)$	Reference Image Greyscale Intensity
$F(x_i, y_j, z_k)$	Reference Volume Greyscale Intensity
G	Shear Modulus

$\bar{G}$	Deformed Image Normalized Greyscale Intensity
$G(x_i^*, y_i^*)$	Deformed Image Greyscale Intensity
$G(x_i', y_j', z_k')$	Deformed Volume Greyscale Intensity
L	Length
m	Matrix (Composites)
$[\bar{Q}]$	Transformed Stiffness Matrix
[S]	Compliance Matrix
[T]	Rotation Matrix
u	Displacement
V_f	Volume Fraction

Chapter 1 Introduction

1.1 Motivation

With the advancement in the composite materials field, the use of composites in industry is growing at a rapid pace. The estimated market size for composite materials in 2021 was USD 89.32 billion[1]. It is expected to reach USD 163.9 billion by the end of 2030. Automotive and transportation, Electrical and electronics, and wind energy have more than 50% market share in the field of composite materials. There is increasing usage of composite materials due to their high strength-to-weight ratio and high stiffness over traditional materials[2]. Braided composites are the subset of composites where braids are made up of interwoven yarns impregnated with a matrix material. The structure of the braids leads to high damage tolerance and structural stability[3]. It is used in systems like jet engine stator vanes, fan blades and shafts. Hybrid composites are a mixture of two or more fibres within the matrix phase. Hybrid fibre composites have many advantages over non-hybrid composites, such as low cost for high stiffness, increase in tensile strength and better damage tolerance[4]. Additive manufacturing (AM) is another form of composites under which Fused Filament Fabrication (FFF) is most widely used. The specimen is manufactured layer by layer from the filament passed through a heated nozzle. The advantage is speedy manufacturing time which helps with the prototyping process[5].

FFF and hybrid composites have a complex microstructure. With the increasing use of composites, there is a need to understand the microstructure under various loading conditions. The traditional measuring techniques, such as strain gauges, are not helpful and provide insufficient results for composites. An advanced measuring technique like Digital Image Correlation (DIC) provides a good full-field displacement and strain map for surface measurement[6]. It can also

detect in-plane and out-of-plane displacement using 3D-DIC[7]. But DIC is limited to surface measurement. It is challenging to map the crack initiation based on the surface measurement technique. Also, the layers inside might have a different strain behaviour which DIC cannot detect.

Digital Volume Correlation (DVC) is similar to DIC but in a 3D space[8]. With the advancement in Micro-CT, it can be used to capture the specimen's internal geometry under loading[9]. With the dataset's help, DVC can generate 3D full-field deformation and strain field. This would help understand the behaviour of internal microstructure and lead to better analytical and numerical models.

1.2 Thesis Objective

The objective of the thesis is to validate DVC method to generate internal displacement and strain map for different materials. DVC is a relatively new measurement technique in engineering and this is a developing strain measurement technique. The first sample is copper metal filled PLA printed using fused filament fabrication. Different infill percentages of 20, 40, 60 and 80 samples would be loaded in tension and the internal strains would be compared. The rich dataset from Micro-CT will be used to extract porosity and copper particle distribution for the sample. The second study will focus on carbon-aramid hybrid braided composite. The sample would be loaded in tension for multiple loadings and with the help of DVC, internal displacement and strain maps would be compared. Also, the artificial seeding is compared with non-seeded sample to find the effectiveness of the particles.

1.3 Thesis Outline

The Thesis is organized into five chapters. Chapter 2 deals with the literature review. The chapter discusses the fundamentals of composites, braided composites, hybrid textiles and FFF

composites. It also discusses the Micro-CT and its applications. Furthermore, it introduces the concept of measuring techniques such as DIC and DVC and their applications. The chapter focuses on identifying the gaps in the literature for FFF and hybrid braided composites. The gaps identified in this chapter will then be addressed in Chapters 3 and 4.

Chapter 3 introduces the application of DVC for 3D-printed FFF structures. The structure comprises of PLA material with copper particles and different infill percentages of 20, 40, 60 and 80. The displacement and strain map is generated and discussed, which is further compared with the analytical model.

Chapter 4 focuses on understanding hybrid braided composite structures using DVC. The displacement and strain maps are generated and discussed. The results also compare the effectiveness of tracking particles against the natural contrast in the study.

The conclusion and future work of the study is provided in Chapter 5.

1.4 References

[1] "Global Composites Market Size, Share & Growth Report, 2030." https://www.grandviewresearch.com/industry-analysis/composites-market (accessed Nov. 10, 2022).

[2] A. K. Kaw, "Mechanics of Composite Materials," Nov. 2005, doi: 10.1201/9781420058291.

[3] C. Ayranci and J. Carey, "2D braided composites: A review for stiffness critical applications," *Compos. Struct.*, vol. 85, no. 1, pp. 43–58, Sep. 2008, doi: 10.1016/J.COMPSTRUCT.2007.10.004.

[4] Y. Swolfs, L. Gorbatikh, and I. Verpoest, “Fibre hybridisation in polymer composites: A review,” *Compos. Part A Appl. Sci. Manuf.*, vol. 67, pp. 181–200, Dec. 2014, doi: 10.1016/J.COMPOSITESA.2014.08.027.

[5] S. Singh, G. Singh, C. Prakash, and S. Ramakrishna, “Current status and future directions of fused filament fabrication,” *J. Manuf. Process.*, vol. 55, pp. 288–306, Jul. 2020, doi: 10.1016/J.JMAPRO.2020.04.049.

[6] H. Schreier, J. J. Orteu, and M. A. Sutton, “Image correlation for shape, motion and deformation measurements: Basic concepts, theory and applications,” *Image Correl. Shape, Motion Deform. Meas. Basic Concepts,Theory Appl.*, pp. 1–321, 2009, doi: 10.1007/978-0-387-78747-3/COVER.

[7] A. Armanfard and G. W. Melenka, “Experimental evaluation of carbon fibre, fibreglass and aramid tubular braided composites under combined tension–torsion loading,” *Compos. Struct.*, vol. 269, p. 114049, Aug. 2021, doi: 10.1016/J.COMPSTRUCT.2021.114049.

[8] B. K. Bay, T. S. Smith, D. P. Fyhrie, and M. Saad, “Digital volume correlation: Three-dimensional strain mapping using X-ray tomography,” *Exp. Mech. 1999 393*, vol. 39, no. 3, pp. 217–226, 1999, doi: 10.1007/BF02323555.

[9] L. Vásárhelyi, Z. Kónya, Kukovecz, and R. Vajtai, “Microcomputed tomography–based characterization of advanced materials: a review,” *Materials Today Advances*, vol. 8. Elsevier Ltd, p. 100084, Dec. 01, 2020, doi: 10.1016/j.mtadv.2020.100084.

Chapter 2 Literature Review

2.1 Composite Materials

Composite materials are rapidly growing in the field of material science and engineering. Composite materials consist of two or more elements are combined macroscopically [1]. The physical and chemical properties of the composites are unique and different from the constituent material properties. The major component in composite materials are fibres and matrix. Generally, the fibres control the mechanical and physical properties of the composites. The matrix binds the fibres together and help in transferring the loads between the fibres. The composite materials have high stiffness and toughness with a better strength-to-weight ratio properties as compared to traditional materials [2], [3]. Due to these properties, they are being widely used in aeronautics, automobile, construction, sports and robotics [4], [5].

2.2 Classification of Composite Materials

There are different ways of classification of composite materials. This chapter will focus on two main categories for classifying composite materials based on the reinforcement and on the matrix material. There are three main types of reinforcements for composite materials: fibre reinforced, particulate reinforced, and flakes reinforced composites as shown in Figure 2-1. Fibre reinforced composites are further divided into continuous fibre (Figure 2-1(a)) and short fibre (Figure 2-1(b)) composites. They generally have a very high aspect ratio as compared to other reinforcements. Aspect ratio is the ratio of length (L) to the diameter (d) of the fibre. Continuous fibre has a high aspect ratio as compared to the short fibre composite. This leads to high mechanical properties in continuous fibre as the load is taken by the fibres unlike in short fibre composite where the matrix takes the load in shear [6]. Particulate reinforced composites are small particles dispersed randomly in the matrix phase as shown in Figure 2-1(c). They have a very low cost of

production and are used where there is a requirement for high levels of wear resistance, such as concrete for road construction [7], [8]. Particulate composites are easier to implement for polymer manufacturing such as injection moulding or 3D printing. Flakes reinforced composite contains flat pieces which are unique as shown in Figure 2-1(d).

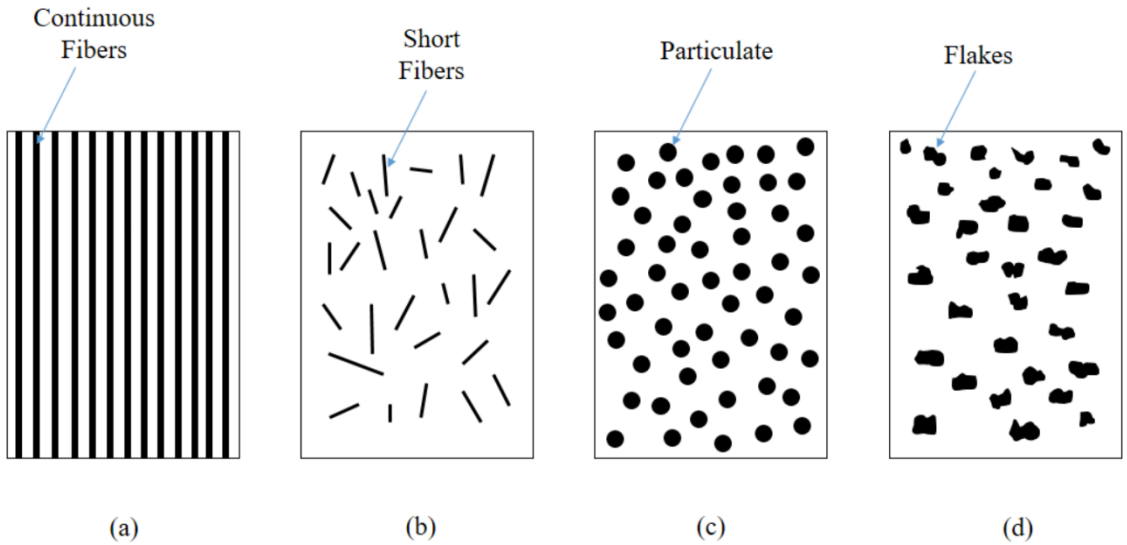

Figure 2-1: Schematic of the different reinforcement types(a) shows the long continuous fibres aligned along the length (b) shows the short fibres which are randomly oriented (c) small particles in random positions (d) Flakes.

There are three matrix phase-based classifications, namely, polymer matrix composite (PMC), ceramic matrix composite (CMC) and metal matrix composite (MMC). PMC is the most widely used amongst the three. They are further divided into two types: thermosetting plastics and thermoplastic. The thermosets have primary molecular bonds and are held together by strong cross-links, while thermoplastics have secondary bonds. Thermosets are generally mixed from the individual components, which are resin and hardener, in a fixed proportion based. In comparison, thermoplastic is available as sheets, powders or pellets. Also, thermosets cannot be melted and

reformed whereas thermoplastics can be reshaped. Thermosets are generally preferred due to their higher strength and resistance to high temperatures [9]. Also, PMCs cost less as compared to CMCs and MMCs because they are easy to handle. CMCs use types of ceramics composed of carbon, silicon carbide, aluminum oxide, and silicon nitride as the matrix. As compared to other matrix-based composites, the CMCs matrix fails first before reinforcement under the loading condition. It offers low density and very high strength. MMCs are generally composed of metals such as aluminum, magnesium, copper and titanium. They are mostly used in automobiles and aerospace field, since they offer superior strength, reduced density and high stiffness. This thesis will focus on PMC materials as these are most commonly used in most structural settings.

2.3 Braided Composites

Braided composites are a category of composite materials that feature long continuous fibre in an interwoven structure [10]. They belong to the family of textile composites. Textile composites are a combination of matrix and textile reinforcements such as woven, knitted and braided fabrics. Braids can be categorized into two types: 2D braids and 3D braids. 2D braids are fibres interlaced together along the longitudinal axis in one plane which will be the focus of the thesis as shown in Figure 2-2. 2D braids are further divided into biaxial and triaxial braids. Due to the yarns undulating under and over, they have high damage tolerance and less stiff than the traditional laminates [10]. Biaxial braids have 2 yarns interlaced together at an angle to longitudinal direction as shown in Figure 2-2 while triaxial braids have a third yarn which is placed in the longitudinal direction of the braids. 3D braids are divided into solid, two-step, four-step and multistep. They are used for high strength and stiffness applications.

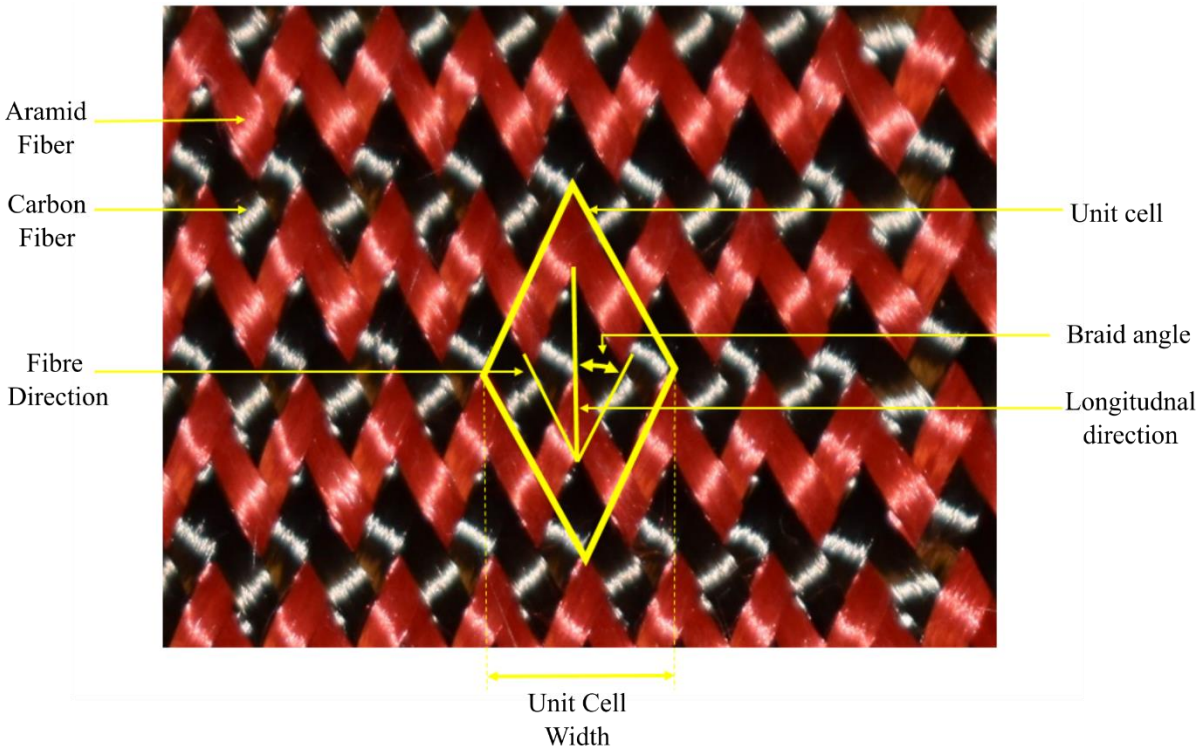

Figure 2-2: Schematic of carbon-aramid biaxial hybrid braided composites which shows the unit cell and its geometrical parameters.

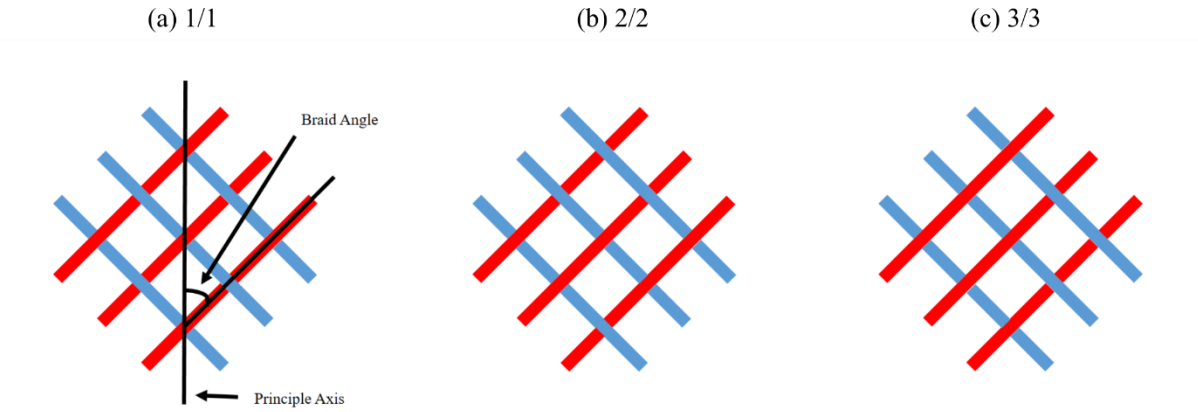

Figure 2-3: Braid unit cell geometries (a) Diamond (b) Regular (c) Hercules showing the braid architecture and braid angle.

The braids are further categorized based on braiding pattern, as shown in Figure 2-3, three most common braiding pattern are: diamond (1/1), regular (2/2) and Hercules (3/3). Diamond are braids in which one yarn overlap one yarn; the regular are braids in which one yarn overlaps two yarns and is the most highly used among the three and the last one is Hercules which are braids in which one yarn overlaps three yarns [11], [12]. Braided composites are commonly used for pressure vessels, columns, bicycle and shafts [13]–[15]. A maypole braider is used to produce 2D braids with the aforementioned patterns [16], [17]. While 3D braids are manufactured using Cartesian or rotary braiding machines. Braids can be manufactured in flat, tubular and three-dimensional shapes.

The geometry of a unit cell (shown in Figure 2-2) of the braid is important to understand since it affects the mechanical strength. Braid pattern, as discussed above, is one of the parameters which affects the mechanical strength. The braid angle (θ), which is the angle between the yarn and the longitudinal direction of the braid, is the most important parameter which affects its strength [1]. If the braid angle is closer to the longitudinal direction, its tensile strength will increase, while if it's closer to the other end, the tensile strength will decrease. But there is a limit to the braid angle range, which is known as jam angle. At this point, the braids will not be able to change the angle further under loading conditions. The practical range of braid angle is 20° to 70° [16].Yarn width is the width of a single yarn in the braid, and can also have an effect on the mechanical properties.

Materials generally used for braids are glass fibre, carbon fibre or aramid fibre. Carbon fibre generally have a high tensile modulus but low damage tolerance and low elongation. Due to which, researchers are incorporating other materials to compensate some of the properties of

carbon fibre. Carbon-aramid hybrid composite has been a good alternative as aramid increases the damage tolerance as well as provides higher elongation [18].

2.4 Hybrid Textiles

Hybrid textiles are made up of two or more fibres combined within a matrix phase as shown in Figure 2-2. They can be inter-layer or intra-layer. Interlayer are layers of different fibre materials stacked over each other but not mixed in the same layer. Intralayer is mix of different fibre materials in the same layer as shown in Figure 2-2.The mechanical behaviour of single material in composite with matrix are understood under loading conditions. With the introduction of another fibre, the mechanical behaviour of composites become more complex and thus there is a need to understand the behaviour. Kretis *et al.* was the first author to compile a review paper focusing on mechanical properties of the hybrid composites in 1987 [19]. There can be various combination of hybrid composites such as carbon-glass or carbon-aramid but the focus for the current study is only carbon-aramid hybrid composite. Few researchers have focused on the mechanical behaviour of hybrid composites under loading. The tensile properties of the hybrid composites are mostly for the unidirectional composites [20]. The hybrid effect for multidirectional composites are reported by few researchers and the results for few of the publications on hybrid effect are doubtful [21]. Rajasekar B *et al.* studied the mechanical properties of intra-ply carbon-aramid/epoxy composite laminates [22]. They found that the hybrid composite laminate provided better tensile strength as compared to aramid/epoxy composite but slightly lower than carbon/epoxy composite. Many of the authors focused on the mechanical behaviour of carbon-aramid hybrid composite for impact loads and residual strength. Wagih *et al.* in their study of post impact flexural behaviour of carbon-aramid hybrid braided composite found that post impact loading increases with the introduction of aramid fibres as compared to carbon/epoxy composites [23]. Similarly, Pincheira *et al.* found with

addition of aramid fibre in carbon fibre composite the impact and fracture resistance increase significantly. Also, there is an increase in ultimate strain and through thickness compression strength [24]. As can be seen from above literature, there is not much research on the understanding of microstructural behaviour of hybrid composites under loading conditions and will be focus of the study.

2.5 Fused Filament Fabrication Composite

Additive Manufacturing (AM) is one of the fastest growing manufacturing fields due to its ability to generate accurate composite parts from solid models as well as automated fast manufacturing of structures. Fused Filament Fabrication (FFF) is one of the methods in AM. FFF is an AM process where a filament is passed through a heated nozzle to form a solid body as shown in Figure 2-4 [25]. The key components of FFF machine are extruder, nozzle, printing bed and roller. Geometry is created from the layer-by-layer deposition of molten thermoplastic filament onto a build plate. FFF is widely used for part replacements, prototypes, making moulds, and even load-bearing structures like in the field of aeronautics [26], construction [27] and biomedicine [28]–[30]. The materials commonly used are thermoplastic polymers like Polylactic Acid (PLA) or acrylonitrile butadiene styrene (ABS), both of which do not have high strength capacity. Various studies have been done to reinforce PLA or ABS with reinforced materials with fibres or metal particles to improve the strength further [31]–[33]. FFF method develops structure layer-by-layer, which is the same as composite laminate materials, which is manufactured layer over layer to form a load bearing structure. Also, the microstructure of FFF can have raster angle which is similar to the fibre orientation angle in composite laminates, an example of which is shown in Figure 2-5. The raster angle has similar effect on the structure mechanical properties as fibre orientation angle in composite laminates. Also, FFF can be reinforced with fibres and metal particles similar to

composite to increase mechanical properties. This shows that FFF can be assumed to be a composite and, requires the similar understanding of microstructure under loading.

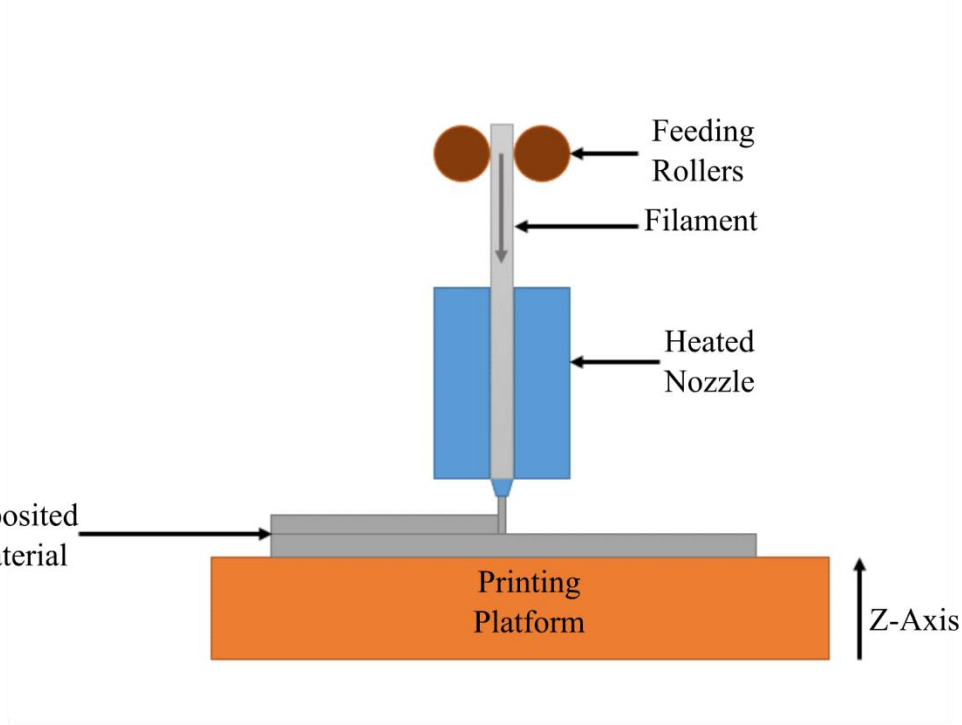

Figure 2-4: Schematic of Fused Filament Fabrication process with deposition of filament on printing platform through heated nozzle.

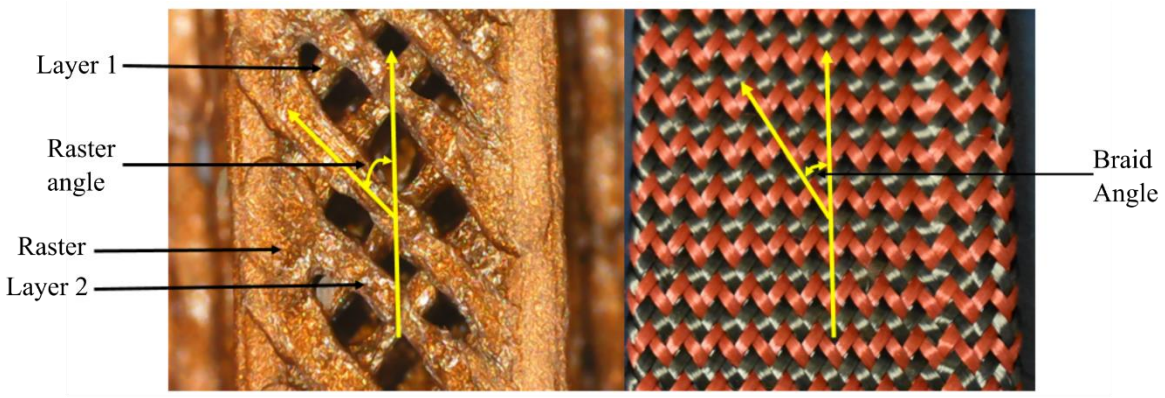

Figure 2-5: Comparison of FFF (left) and Composite (Right) with similar geometrical properties.

For the thesis, the focus will be on metal particle reinforced FFF composites. The addition of thermoplastic matrix material improves the tensile strength, wear resistance and dielectric permittivity [34], [35]. With particle reinforced composites, there are many factors which effects the mechanical properties of the composite such as particle size, particle loading, interfacial adhesion, and surface treatment [34]. It is difficult to isolate the role of the above factors due to their interplay in determining the overall mechanical behaviour [36]. Because of these factors, it is difficult to predict and characterize the mechanical properties of the FFF composites. Therefore, a suitable measurement method is needed to characterize the mechanical behaviour of FFF composites.

2.6 Micro-CT

Braided composite and reinforced FFF structures have a complex internal microstructure as shown in Figure 2-5. It is important to understand the geometry non-destructively as the internal geometry affects the mechanical behavior of these materials. This is where the Micro-CT plays an important function. The data from Micro-CT can be further utilised for measuring displacement and strain which will be discussed further.

Micro-CT is a non-destructive method that uses X-rays to image the internal microstructure of an object [37]. The X-ray beams are ejected through the X-ray tube towards the sample. Based on the attenuation coefficient of the material, which is the measure of how easily beams are absorbed and transmitted with different intensities. The detectors are placed at the end, which collect the transmitted X-rays, which provides a 2D projection of the sample as shown in Figure 2-6. The sample is rotated 180 or 360 degrees to acquire sufficient projections from different angles to resolve the 3D geometry.

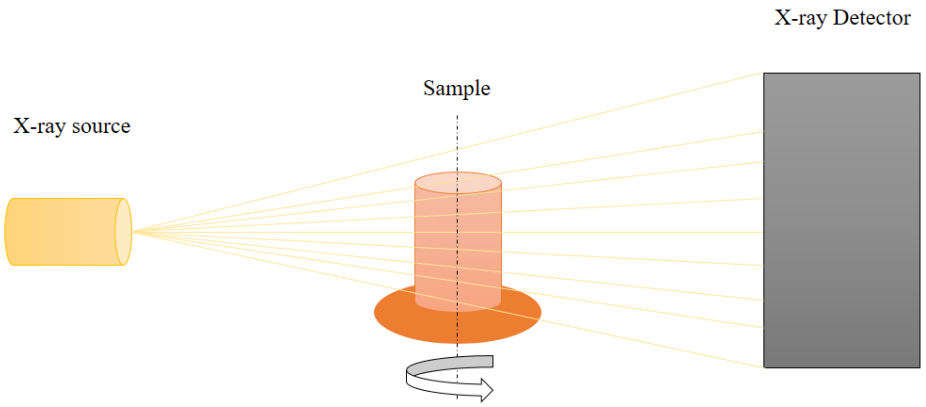

Figure 2-6: Schematic of Micro-CT showing the emission of X-rays which is passing through sample and collection by the detectors.

After the projections are collected, an image reconstruction process is used to give a stack of the cross-sectional image of the sample. Software such as NRecon(version 1.7.1.0, Bruker, Belgium), which is a reconstruction software, uses the Fourier Slice Theorem to reconstruct the projections into the volumetric image dataset [38]. Noise can be introduced in the data, for example ring artifacts, beam hardening, Poisson noise, or metal artifacts [38]–[41].

Micro-CT has been extensively used for many applications in AM, more specifically for FFF. There are many reasons to the need of the Micro-CT process, such as process induced porosity, or defects due to non-optimal build parameters which can affect the mechanical properties of the specimen cannot be measured through traditional methods. Therefore, Micro-CT can be used to understand the defects and porosity. Timpano *et al.* used Micro-CT to investigate the copper-filled PLA specimen printed using FFF [42]. The author segmented the PLA and copper

particles from the Micro-CT data and found the size and count of the copper particles in the specimen. They also found the cross-sectional dimensions area of the specimen. To assess the printing post-manufacturing, air gap measurements were made. For 100% infill percentage, they found the air gap of 0.025, 0.020 and 0.017 mm^3 under tensile loading of 100, 150 and 200 N, respectively. The results show as the load is increased the air gap decreases which leads to increase in stiffness of the specimen. The air gaps were between the shell layers and the infill of the material or between the rasters.

Murali *et al.* investigated the internal microstructure of PLA samples printed using FFF [43]. They used two different infill patterns, gyroid and cubic subdivision, with 50% infill density. The pore distribution for the gyroid pattern was found to be more uniform than the cubic subdivision pattern. They found 70.01% porosity for the cubic subdivision sample higher than the gyroid sample, which was around 38.5%. They found difference of up to 20% in the calculation of porosity from Micro-CT with theoretical method because of the defects in the manufacturing. This study gives a good idea of how Micro-CT can be used to assess the actual porosity by non-destructive means.

Many authors have used Micro-CT to understand the microstructure of the FFF printed specimen reinforced with particles or fibres. This can help increase the strength of the FFF specimen and further increase its applicability for load-bearing structures. Sommacal *et al.* used Micro-CT to understand the voids in a 3d printed carbon reinforced PEEK sample and its filament [44]. They used 5 samples with different printing parameters. The Micro-CT data was segmented to find the voids, short fibres & resin, and their distribution across the sample. The feedstock material had a high void content of 19.9% and randomly distributed. Also, they found that the

voids originally present in the feedstock were still present after printing, and the printing parameters did not make much difference.

Yu *et al.* used Micro-CT to understand the internal microstructure of fibres and voids for basalt fibre-reinforced PLA specimens manufactured using 3d printing [45]. They used image segmentation to find the volume fraction of fibres, voids and matrix phase for 4 specimens with different fibre stacking. They also found the distribution of the fibre diameter and fibre length as volume fraction percentages. With the help of visualizing the fibre orientation and voids, they could establish the cause of voids. Also, the author concluded that the effect of printing direction can enable to customize the elastic modulus, shear modulus and Poisson's ratio of the specimen.

Micro-CT can be helpful to characterize the internal geometry of composites. It can be used to understand the interfacial bonding characteristics, void content as well as damage detection by non-destructive means. Geometry measurement for the braided as well as textile composites can be useful for improving the accuracy of analytical and numerical models. Melenka *et al.* in their study, used Micro-CT to identify and measure braid yarn fibres of regular 2x2 cellulose fibres embedded in a bio-based resin for two samples with 45° and 55° braid angles [46]. They used an XFibre extension for fibre identification. Other properties were also investigated such as Fibre Tortuosity, Fibre curved length and Fibre Orientation Angle.

Gu *et al.* examined four 2D carbon fibre braided composite using Micro-CT to understand the torsional progressive damage and failure mechanism [47]. The samples had different braiding angles, i.e. 30°, 45°, 55° and 60°. The author calculated the volume of damages and torsional damage morphologies. They found damage volume of 30° and 60° samples higher than the others. They were able to find damage characteristics such as delamination, debonding between yarns, matrix cracking, fibre bridging, etc, on different samples using Micro-CT data.

Similarly, Shi *et al.* for their low-velocity impact experiment on an inter-ply biaxial-uniaxial braided tube, employed Micro-CT to evaluate the crack locations as well as to characterize the damage mechanism [48]. The author was able to identify the damage characteristics such as delamination, yarn splitting, resin crack and inter-yarn debonding through the Micro-CT dataset.

In terms of hybrid composites and Micro-CT, limited research has been explored to understand the characteristics. Yin *et al*. investigated carbon-aramid hybrid woven composites using Micro-CT for crack initiation and failure mechanisms [49]. They manufactured two specimens, the first one where carbon fibre orients along the loading direction and the second sample where aramid fibre orients along the loading direction. They examined the Micro-CT data to characterize the internal damage initiation and progression of failure. They found that for the first specimen, kink bands are the initiation of damage which causes matrix cracking. Further, at the failure stage, delamination, tow debonding and fibre breakage were observed. For the second sample, damage initiate due to tow stripping and at the failure stage, delamination, fibre fracture and matrix cracking were observed.

The damage characterisation of composite materials was explored by the above authors using Micro-CT. For the study of strain measurement using non-destructive optical measurement techniques, the damage initiation and characterisation findings from Micro-CT can help understand the strain results and better FEA models can be developed.

As can be seen from the above literature, Micro-CT can provide a wealth of information for both FFF and braided composites. The porosity analysis and geometry measurement are an important aspect for the final objectives of the thesis. As well as the Micro-CT data obtained can be further used for strain measurement technique which will be discussed below. Internal strain

measurement is required for both FFF and braided composites due to the complexity of the internal structure of both materials.

2.7 Digital Image Correlation (DIC)

The traditional strain measuring instruments such as strain gauges are suitable for homogenous and isotropic materials. But with the composite materials, which are non-homogenous and orthotropic, strain gauges do not provide enough information[50]. Some of the common failures such as fibre breakage and delamination can happen at any point in the specimen and strain gauge will not be able to capture the information. Full field strain measurement through optical measurement techniques like Digital Image Correlation (DIC) can help capture all the information to characterize the mechanical behaviour accurately.

DIC is an advanced non-contact optical measurement technique which measures the full field surface deformation and generates strain fields for the sample [51]. The measurement technique uses charged couple device (CCD) camera, complementary metal oxide semiconductor (CMOS) or a digital single-lens reflex (DSLR) to measure the deformation and generate strain fields. The DIC process is called 2D DIC or 3D DIC, depending on the number of cameras used. 2D DIC uses single camera to measure in-plane displacement measurement while 3D DIC uses two cameras to measure the in-plane and out of the plane displacement measurement. The process involves experiment design, experiment setup and image processing.

The DIC experiment design has many parameters; firstly, region of interest and 2D or 3D strain for the specimen. Region of interest (ROI) is an important parameter which will dictate other parameters for the design [51]. Based on ROI, the camera field of view as well as the depth of field is calculated as shown in Figure 2-7. Based on 2D or 3D strain, number of cameras is decided.

Further, many more parameter such as exposure time, sampling rate, lens aperture, lighting is finalized.

With the experiment setup, the first step is to speckle the specimen. It is the most important part of the measurement technique, and the results will depend on it. The specimen is coated with black paint and white paint is used for random speckling over the black paint specimen or vice versa as shown in Figure 2-7 [52]. The speckle can be created using various techniques such as air brush, sponge or roller [53]. The size of the speckling depends on the expected deformation of the specimen as well as the field of view [54]. The speckles act as a marker to track the displacement of the specimen. It is expected to have at least 5 pixels in diameter to have enough contrast.

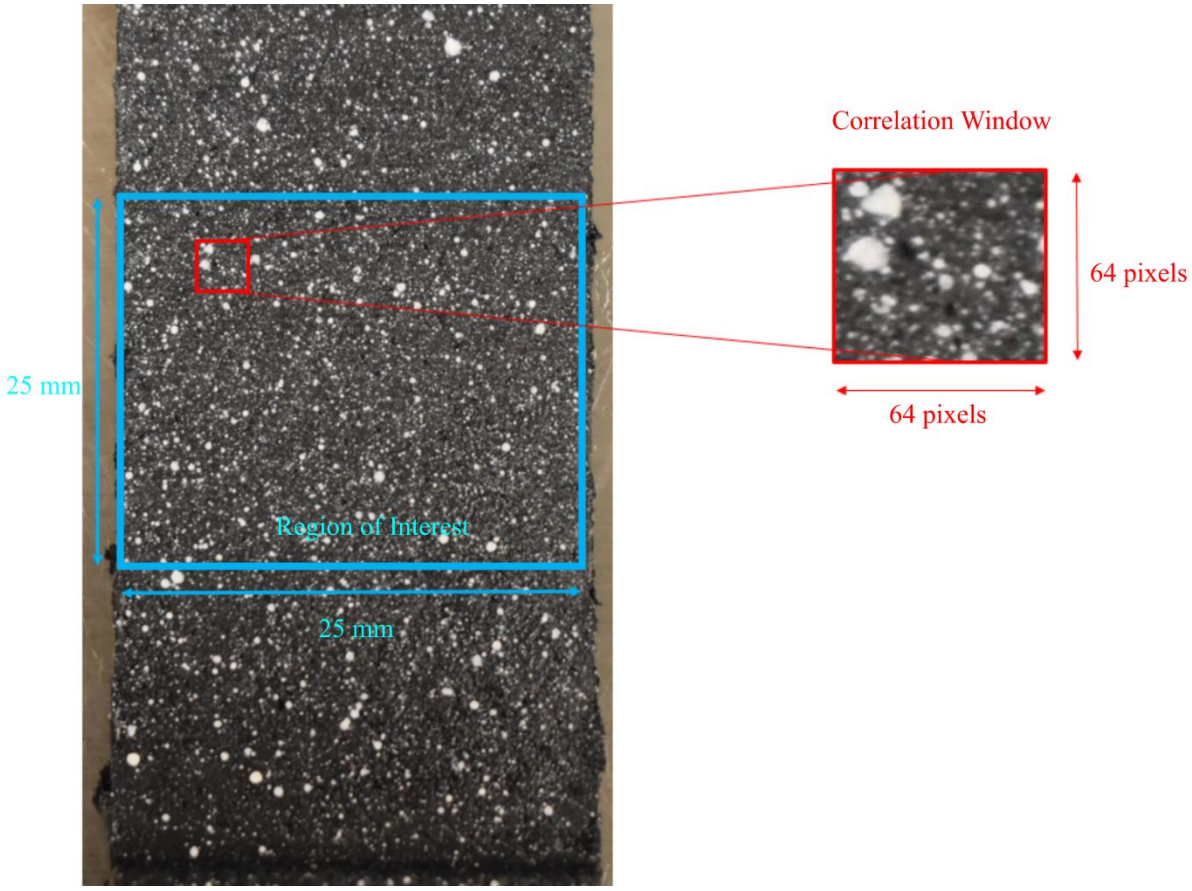

Figure 2-7: Speckle pattern for a flat hybrid braided composite which shows the Region of Interest and the correlation window size for DIC.

The second step is to have the specimen and DIC setup ready according to the experiment design. The Figure 2-8 shows the specimen with the DIC setup. The camera lens calibration is important to have the expected field of view. The camera distance, lens magnification, and depth of view must be calibrated to get the expected field of view. Also, the lighting equipment needs to be placed properly so that enough details can be captured if there is a high strain rate as well as the surface should not be reflective. Furthermore, the image calibration is required to convert pixel

dimension into physical dimension. The position of the calibrator should coincide with the position of the sample and the setup should not be moved.

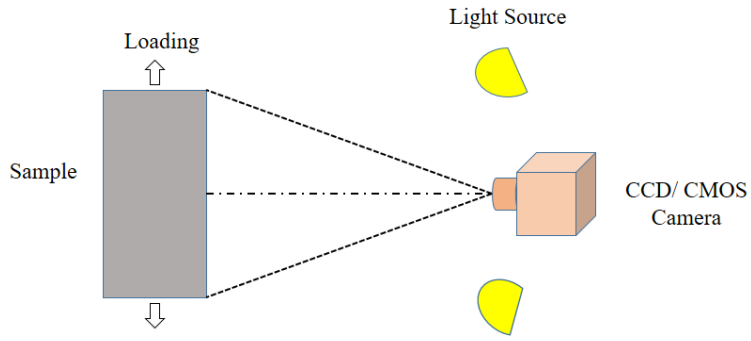

Figure 2-8: Schematic of DIC system which shows the sample under loading. The light source is provided for proper lighting on the surface along with the camera to capture the details which will be used further for correlation.

The DIC data is collected and further processed. The first step is to select the subset size over the ROI, subset size is basically the search window in which the reference as well deformed image set, will be discretized into a grid as shown in Figure 2-9. The reference subset is compared with the subsets from the deformed subset. The speckle pattern in each subset acts as tracker particles whose movement is measured to find the displacement. The comparison of the subset between reference and deformed is made using a cross-correlation method. A few of the cross-correlation methods are cross-correlation (CC), Normalized cross-correlation (NCC) and Zero mean normalized cross-correlation (ZNCC)[55]. The grayscale intensity of the reference image is denoted by $F(x_i, y_i)$ for the coordinates (x_i, y_i), and the grayscale intensity of the deformed image is denoted by $G(x_i^*, y_i^*)$ for the coordinates(x_i^*, y_i^*). $(\bar{F})$ and $(\bar{G})$ are the normalized greyscale intensities for the reference and deformed images. The Equations (2-1) & (2-2) below shows the formulation behind different cross-correlation criterion.

$$CC = \sum_{i=-M}^{M} \sum_{j=-M}^{M} [\ F(x_i, y_i)\ G(x_i^*, y_i^*)] \tag{2-1}$$

$$NCC = \sum_{i=-M}^{M} \sum_{j=-M}^{M} [\frac{F(x_i, y_i)\ G(x_i^*, y_i^*)}{\bar{F}\bar{G}}] \tag{2-2}$$

The above equations are used to solve the displacement, the CC values for each subset correlation are plotted, and the peak correlation value gives the position of deformed subset from the reference subset. Also, sub-pixel displacement calculation is made to find displacement less than a resolution of integer pixel. Generally, interpolation methods are used to find the sub-pixel displacement. Some of the widely used are Newton-Raphson iteration and gradient-based methods [56], [57].

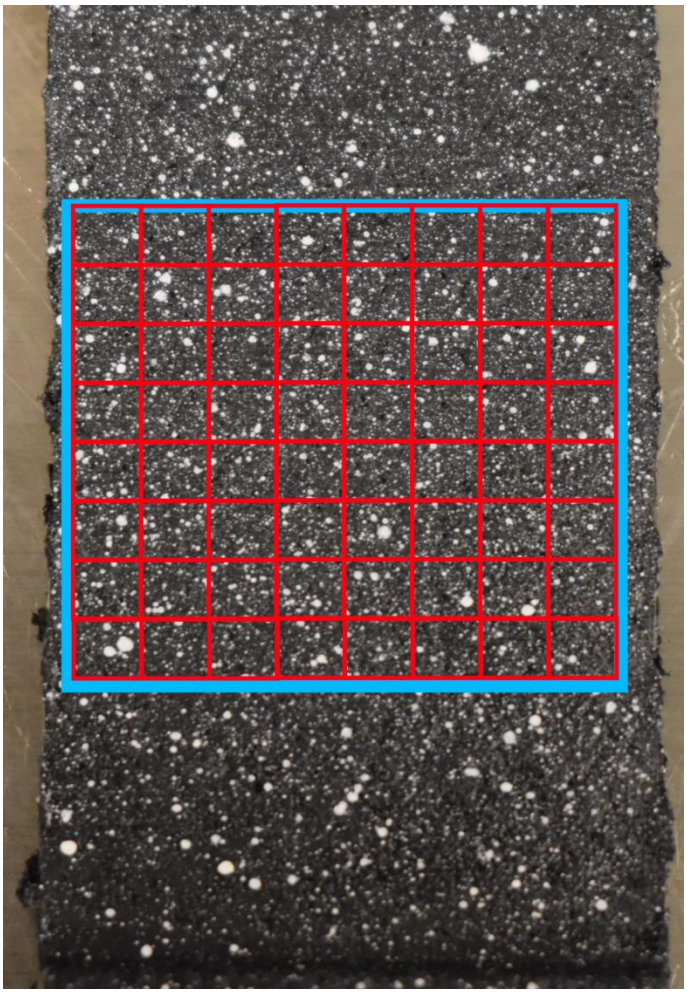

Figure 2-9: Discretization of Region of Interest into grids.

To calculate strain, the numerical differentiation of the displacement is performed [52]. Due to this, the noises from the displacement get amplified and smoothing filters are used to reduce the noise. Various strain formulations can be computed based on the material and the observed deformation.

DIC has been used to understand the effect of various printing parameters of FFF composites for full-field surface displacement and strain mapping. The traditional strain gauge and extensometers are limited by the deformation at specific locations and require direct contact with the sample. Gonabadi *et al.* studied the effect of build orientation and infill density and pattern

using DIC [58]. The specimen was based on ASTM D638 and ASTM D5379 for tensile and shear tests respectively. They used a single CCD camera with a spatial resolution of 5.5 µm/pixel to acquire images during tensile and shear testing. The authors found that 0° on-edge build orientation, which is a specimen manufactured on the edge of the sides with the plate support instead of a face, has better mechanical properties than other build orientations. Large variation was observed in the mechanical properties for different build orientations. The strain map showed high strain localization at the end of the gauge length. But the mechanical behaviour for different infill patterns was similar. The increase in infill density leads to an increase in tensile properties in a quadratic manner.

Zaldivar *et al.* investigated the effects of the print orientation of ULTEM 9085 resin material. They used a Stratasys fused deposition modelling 400 printer [59]. The dogbone coupons are based on ASTM D638-10 Type 1. They manufactured 6 orientations, i.e. flat 0°, flat 90°, edge, upright, edge 45° and flat 45°. ARAMIS DIC system with two-megapixel cameras was used during the tensile test. The deformation field generated through DIC showed that, based on the various build orientations, the parts were highly anisotropic. And the microstructure shows that the FDM part behaves more like composite structures than isotropic cast resins.

Leung *et al.* studied a tubular braided composite using a stereo DIC technique and an optical microscope and measured the change in braid radius and braid angle during tension [60]. They studied the change in radius for unit cells in 3 regions of the tube on the surface. They used two 1376 x 1040 pixel CCD cameras attached to stereomicroscope. The approximate field of view was 5.5 mm x 4 mm. They found under axial loading the radius decreases in order of 100 µm. The author concluded that the change in radius and braid angle could affect the elastic modulus by 10%.

Cerbu *et al.* used DIC for hybrid carbon-aramid composites under tensile and bending loading to get the mechanical characteristics for numerical simulation as well as analytical modelling [18]. They used Nikon D7200 camera for capturing specimen image, with the image resolution of 6000 x 4000 pixels. The author was able to validate the numerical simulation with the experimental results with the recorded maximum errors between experimental and theoretical were 0.19% and 0.15% for the tensile and flexural modulus respectively. The strain map results did not indicate any different behaviour for the different fibres in hybrid composites.

Armanfard *et al*. used 3D-DIC to evaluate the behaviour of carbon fibre, glass fibre and aramid braided composite tubes under combined tension-torsion loading [61]. 3D-DIC uses two sets of cameras to capture the in the plane and out of the plane strain which is not possible with 2D-DIC. The author used two high resolution cameras with 2464 x 2056 pixels and pixel size of 3.45 µm with a stereo angle of 17°. The approximate field of view was 115 x 94 mm^2. The shear strain field generated using 3D DIC showed non-uniform strain distribution due to the woven structure of the braided composites. It was found that with increasing torsional load under combined loading, buckling initiates at the maximum shear stress point in the braid. But, with composites the behaviour inside the layers can be different from the surface behaviour. Defects such as delamination, crack initiation could not be studied by the author with the surface measurement 3D-DIC technique.

DIC is a useful and accurate tool to measure the surface deformation and generate full field strain map of composites. Also, the results obtained provide a lot more information as compared to traditional measuring technique. But DIC has its own limitations. For example, DIC can only measure surface level displacement and strain. Since composite materials can have different microstructural mechanical behaviour from surface mechanical behaviour which DIC may not be

able to capture. The next section will focus on the advanced measurement technique Digital Volume Correlation (DVC) which can capture volumetric displacement and strain. Figure 2-10(a) shows a Micro-CT volume view of braided composite specimen. Unlike DIC, full internal volume strain can be generated for the Volume of Interest as shown in Figure 2-10(b). Also, strain of multiple slices can be viewed for the specimen which can be seen in Figure 2-10(c), and it can be helpful for understanding mechanical behaviour of anisotropic materials.

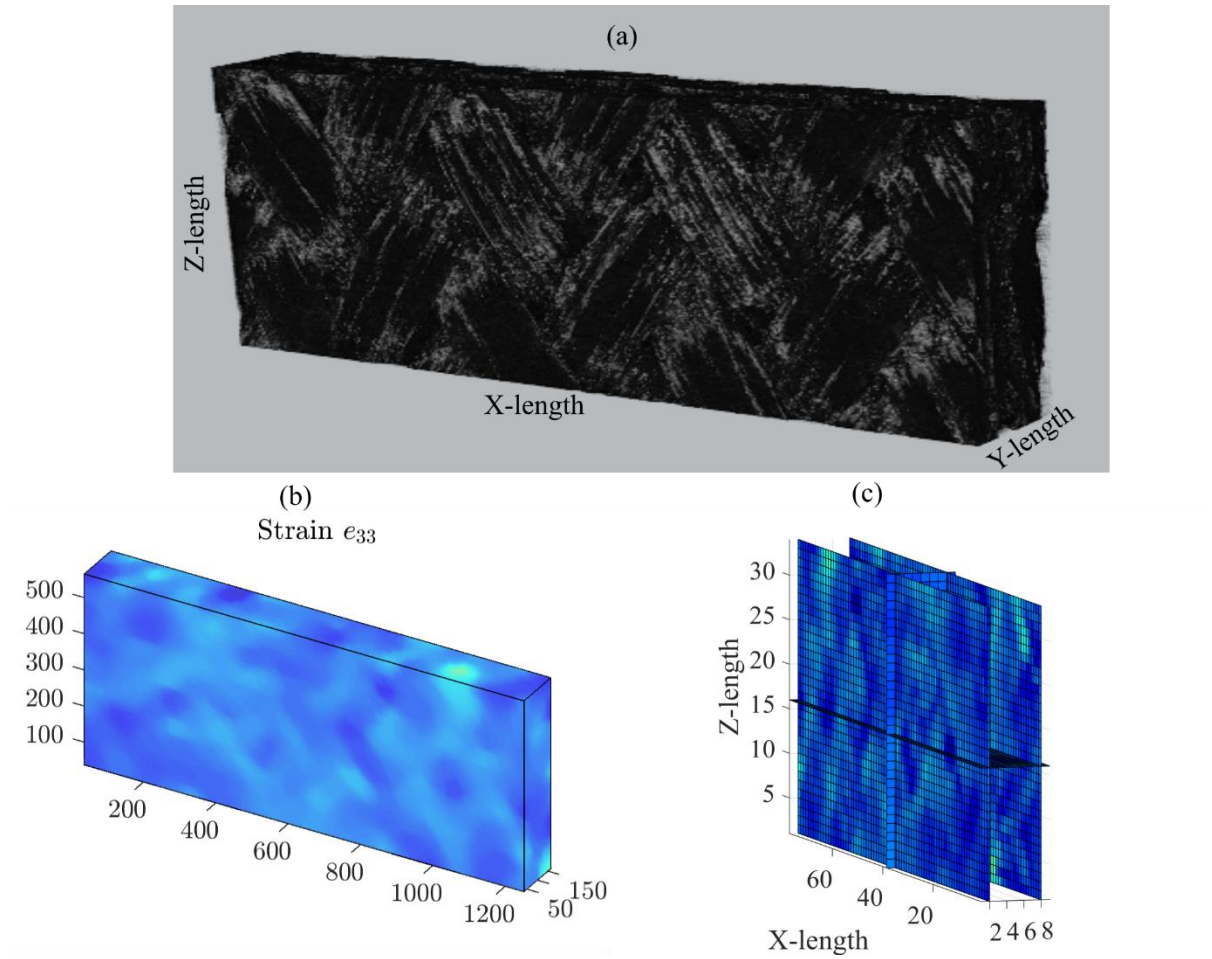

Figure 2-10: (a) Micro-CT volume view of braided composite(b) Volumetric Strain of the braided composite specimen (c) multiple slices strain across the thickness of the specimen.

2.8 Digital Volume Correlation (DVC)

DVC is an advanced measurement technique to measure the 3D deformation and strain of an object; DVC is similar to DIC but in a 3D space. DVC can use volumetric data such as X-ray CT or magnetic resonance imaging (MRI) data to measure deformation and generate full field internal strain map [62], [63].

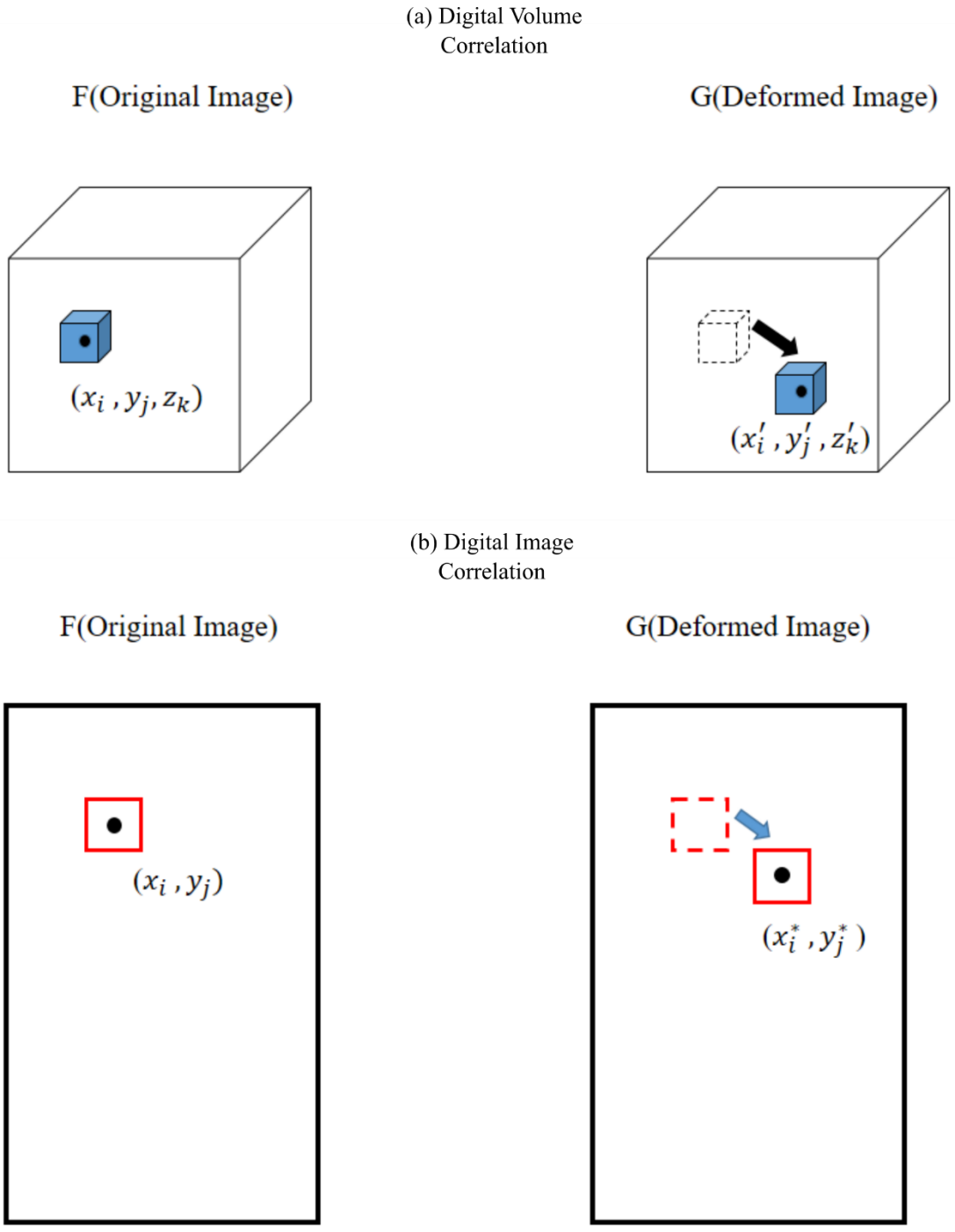

Figure 2-11: (a) Schematic of sub-volume displacement of the sample before loading and after loading (b) Schematic of sub-square displacement of the sample before loading and after loading.

To measure the displacement, the reference and deformed image volume stack is defined. The subset is a 3D cube unlike a 2D square in DIC. The subset size and subset spacing divides the image into grids over the volume. To compare the subsets from the reference and deformed image stack, the speckle pattern is added inside the specimen or natural contrast between the layers which acts as marker to find the displacement is used. DVC has the same formulation as DIC for calculating displacement but in a 3D space. The reference subset is compared with the subsets in deformed image stack, based on cross correlation method. This gives correlation value for all the subsets compared and the correlation peak gives the best possible match of reference subset in the deformed volume. The position of both the subsets can help calculate the displacement as shown in Figure 2-11. It uses the cross-correlation method to compare subsets as in DIC (like equations (2-1 and (2-2 above) but in a 3D space. $F(x_i, y_j, z_k)$ represents the grey scale intensity of the reference subvolume and $G(x_i', y_j', z_k')$ represents the greyscale intensity of the deformed sub-volume. The formulations are given below.

$$CC = \sum_i \sum_j \sum_k [F(x_i, y_j, z_k) G(x_i', y_j', z_k')] \tag{2-3}$$

$$NCC = \frac{\sum_i \sum_j \sum_k [F(x_i, y_j, z_k) G(x_i', y_j', z_k')]}{\sqrt{\sum_i \sum_j \sum_k F(x_i, y_j, z_k)^2 \sum_i \sum_j \sum_k G(x_i', y_j', z_k')^2}} \tag{2-4}$$

Bay *et al.* was the first researcher to develop DVC displacement across the volume [64]. He tested two samples, the first within the elastic range with nominal strain of 0.004 and 0.008. The second was beyond the initial stages of yield with nominal strain of 0.006 and 0.018. They

used sum of squares displacement correlation method for calculating displacement. They found the local strains to be significant times greater than the nominal strain level for both the samples.

DVC is an evolving field and so are the algorithms used for this analysis process. Some of the commercial software such as LaVision StrainMaster DVC & Correlated Solutions VIC-Volume are expensive to use which makes it difficult for researchers to work with DVC. There are numerous open source software available such as uFreckles, Tomowarp2, FIDVC, SPAM, and ALDVC [65]–[68]. For the current scope of study, ALDVC software will be discussed. ALDVC is a MATLAB based DVC program. The program compares the original and deformed images to find the 3D deformation and strain values of the specimen. The program is different from other DVC packages, which utilize local or global-based methods to find the displacement and strain values. Local-based methods correlate each volumetric subset independently which is fast but kinematic compatibility is achieved with global methods at a cost of high computational power and time. FIDVC and TomoWarp2 are a few open-source DVC software with local correlation approach [69]. ALDVC uses both the local and global methods, local to correlate a single volumetric subset that is independent of other subsets and a global method for the subsets to be kinematically compatible. It uses the Alternating Direction method of Multipliers (ADMM) to divide the correlation into two subproblems. The first one focuses on the local based method, which is done in parallel with other subset and the second subproblem focuses on global method for kinematic compatibility. This helps to find displacement and strain values for big volume specimens at a low computational cost as well as less time.

Before moving to the application of DVC, it is important to understand the effect of contrast enhancement techniques. Until now, researchers are divided into using seeding particles or natural contrast for correlation. The Figure 2-12 shows the difference between the copper and non-copper

specimen internally. Croom *et al*. are the first group to look into the effect of natural pattern for DVC [70]. They used synthetic foams with different volume fractions under compression. They found that before the pattern deteriorated by 30-40% results for DVC were accurate.

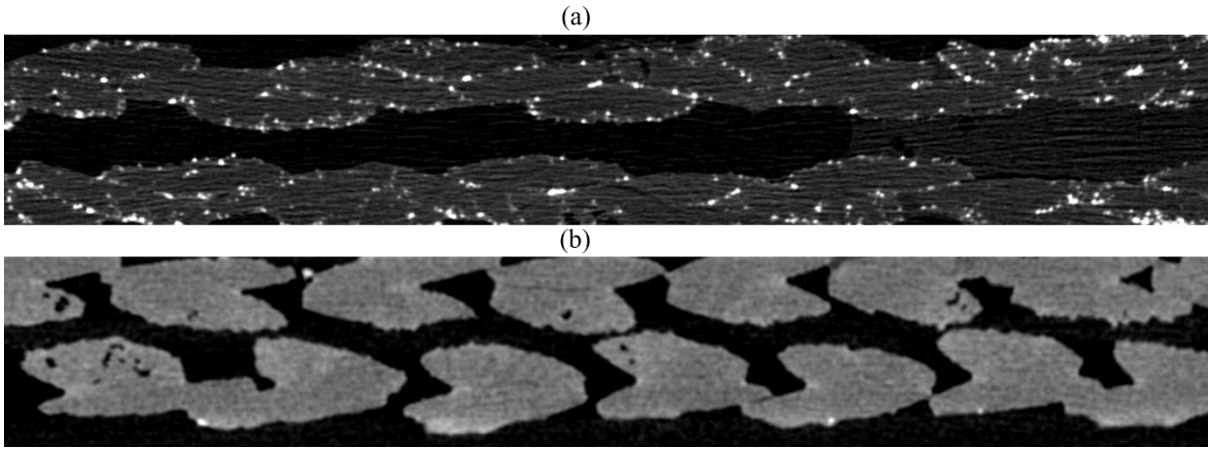

Figure 2-12: Shows the comparison of (a) copper seeded vs (b) natural contrast hybrid braided specimen.

Croom *et al*. also investigated the effect of seeded particles on DVC [71]. They used synthetic foam filled with hollow glass microballoons and the sample was put under compression. They found even after 40% of microballoons collapsed, the DVC results were still quite accurate. Timpano *et al.* is another author who explored the effect of artificial contrast enhancement to an epoxy resin [72]. The study investigated particles with different sizes of 10, 25, 50 and 200 µm embedded into epoxy resin under loading to find optimal DVC datasets. The different materials used were copper, zirconium and aluminum nitride. The author found 25 µm copper particle size to give the best results under loading for DVC measurement technique. The current studies in literature all have either focused on natural contrast or speckle pattern within test samples. But there has been no research comparing the speckle pattern with the natural contrast pattern for a similar sample which will be explored in this thesis.

DVC for FFF composites can help to understand the effect of process parameters on the microstructure which is not possible with DIC and the traditional strain gauge measuring instruments. Wang *et al.* was the first one to examine the behaviour of AM structure using DVC for 3D printed porous structure [73]. The sample was made into an hourglass structure with stereolithography method. They conducted a uniaxial compression on the sample with a preloading compressive loading of 10N. The strain was increased from 4% to 20% with step increments. The volume of interest of the sample was 33.2 mm x 33.2 mm x 32.4 mm with a voxel size of 55.3 µm. They used zero-mean normalized cross-correlation method to find displacement and 3D pointwise least-square approach to find the six Cauchy strain fields from the displacement field for each loading stage. They found high tensile strain on the top/bottom edge of the hourglass and high compressive and shear strain on the side walls of the structure. Also, as the load increases the strain localization becomes more significant.

Melenka *et al*. did a preliminary study on use of DVC for tubular braided composites [74]. He used a 45° regular braid which was made from cellulose fibres and impregnated with a bio-based resin. The sample was placed under a compressive load of 244.6N and further using DVC, the 3D displacement and strain fields were generated. This shows the potential of DVC for full-field internal displacement and strain maps. Timpano *et al.* used DVC to generate internal full field deformation and strain maps for the copper filled PLA specimen manufactured using fused filament fabrication [42]. Samples were designed based on ASTM D638-14 Type V. The sample was loaded in tension for preload of 100 N and step load of 150N and 200N. They used Skyscan 1272 Micro-CT with resolution of 4904 x 3290 pixel and pixel size of 1.6 µm. The author used open-source DVC software called FIDVC which is based on MATLAB. They used subset size as small as 32 cubic voxels to find the displacement. And the strain values were calculated with

Lagrangian linear elastic strain formulation. They downsampled the dataset to decrease computational time. The author observed the development of diagonal strain bands across the specimen, and the strain bands were aligned in the direction of internal rasters of the sample. This is the only study which focused on the application of DVC for FFF composites and the results of which showed the capability of DVC to map internal strain fields. For the composite structures, the application of DVC has primarily focused on characterizing the complex failure mechanism and its progression. Holmes *et al.* examined the deformation and damage characterisation of woven fibre reinforced composite with the help of DIC and DVC [75]. The woven fibre is a pre-consolidated single layer 2/2 twill glass fibre/polypropylene composite. The sample was loaded in tension, and preloading & post loading micro-CT dataset was collected. They used a voxel size of 9.77 µm/voxel. They used open-source DVC software called ALDVC. They chose subset size of 30 cubic voxels with spacing of 10 voxels. They relied on the internal natural contrast of the specimen to find displacement. They were able to identify areas with high out of plane strain, and the initiation of damage characteristics with cracks and delamination.

Mehdikhani *et al.* investigated the micro as well as meso damage analysis of carbon fibre composites using DVC [76]. The material used for the study was carbon fibre/epoxy composite with a stacking sequence of $[90_4/0_5]_s$. The field of view with the Micro-CT scan was 2016 x 2016 x 1716 voxels with pixel size of 1.1 µm. They relied on the natural contrast of the fibres to calculate displacement. The sample was loaded in tension. Their analysis of digitally deformed data showed that a smaller FE element are more beneficial for the crack morphology but is more expensive computationally. They found that the subset-based DVC can detect different damage mechanisms such as matrix cracks, ply delamination and ply splits while FE based DVC allows

better characterization of damage. Also, DVC can determine the directionality as well as mode of damage even if no crack initiates.

Liu *et al.* examined the failure of 3d braided SiC_f/SiC composites under flexural loading using DVC [77]. The two specimen was pre-loaded with 30N and then with higher loads. The pixel size was 7.2µm and volume of interest was 1700 x 630 xx 850 voxels. They used LaVision StrainMaster DVC software for the DVC analysis. The author was able to map the displacement and strain fields for the two samples. They found the damage initiated at the tensile part of the specimen. Also, a progressive quasi-brittle failure was observed.

As can be seen from the above studies, DVC provides a significant amount of information of the microstructure of composite structures. For AM, full field strain and displacement map were generated which showed the high strain region. For the composite materials, it was used for internal displacement and strain map generation. It was also useful in characterizing the damage within the sample.

2.9 Conclusions

DVC is relatively a new measurement technique. As can be seen, Timpano *et al*. research on metal filled PLA printed FFF specimen using DVC is the only paper which utilized DVC for the investigation of FFF composite [42]. Wang *et al*. also used DVC but in the field of stereolithography for a porous structure [73]. The current literature for AM is limited which deals with the microstructure behaviour using measurement techniques and there is a lot of scope to understand the AM composites. The effect of process parameters is understood from the surface measurement techniques, but with the application of DVC, the effect on the microstructure can be understand and better analytical models can be developed. Since, Timpano *et al*. researched with 100% infill density, the study for thesis would be to understand the microstructure behaviour for

different infill percentage using DVC which would further validate the measurement technique. Chapter 3 of the thesis will be focusing on the application of DVC for FFF composites. It will focus on understanding the microstructure behaviour of 20, 40, 60 and 80 infill percentage for copper particle reinforced PLA sample.

In terms of composite materials, there is limited research with respect to the DVC measurement method. Specifically for braided composites, Melenka *et al.* studied the braided composites with DVC but the application was limited [74]. Hybrid composites are an emerging field due to the advantages discussed above. Currently, the understanding for hybrid composite mechanisms is still evolving and have been explored from traditional measurement techniques. For hybrid braided composites, Cerbu *et al.* and few others have worked with DIC but no research has been done with DVC [78]. Using DVC for hybrid braided composites can provide wealth of information on the microstructure under loading, interaction between the hybrid fibres and many more. As can be seen from the literature on contrast pattern for DVC, the research is divided between natural contrast and artificial seeding. Croom *et al*. and Timpano *et al*. did investigate the effect of contrast pattern but none of the studies compares both of the pattern together [70], [72]. Therefore, the chapter 4 of the thesis will focus on the following gaps. First is the investigation of carbon-aramid hybrid braided composite under tensile loading using DVC. And the second objective would be to study the effect of natural pattern and artificial seeding for DVC and the recommendation based on the results.

2.10 References

[1] A. K. Kaw, “Mechanics of Composite Materials,” Nov. 2005, doi: 10.1201/9781420058291.

[2] D. K. Hale, “The physical properties of composite materials,” *J. Mater. Sci. 1976 1111*, vol.

11, no. 11, pp. 2105–2141, 1976, doi: 10.1007/PL00020339.

[3] R. M. Jones, “Mechanics Of Composite Materials,” Oct. 2018, doi: 10.1201/9781498711067.

[4] P. K. Saha, “Introduction to Composite Materials for Aerospace,” *Aerosp. Manuf. Process.*, pp. 149–180, Oct. 2016, doi: 10.1201/9781315367965-13/INTRODUCTION-COMPOSITE-MATERIALS-AEROSPACE-PRADIP-SAHA.

[5] F. C. (Flake C. . Campbell, “Structural composite materials,” p. 612, 2010.

[6] F. Rezaei, R. Yunus, and N. A. Ibrahim, “Effect of fiber length on thermomechanical properties of short carbon fiber reinforced polypropylene composites,” *Mater. Des.*, vol. 30, no. 2, pp. 260–263, Feb. 2009, doi: 10.1016/J.MATDES.2008.05.005.

[7] S. Gopalakrishnan and N. Murugan, “Production and wear characterisation of AA 6061 matrix titanium carbide particulate reinforced composite by enhanced stir casting method,” *Compos. Part B Eng.*, vol. 43, no. 2, pp. 302–308, Mar. 2012, doi: 10.1016/J.COMPOSITESB.2011.08.049.

[8] M. C. Tanzi, S. Farè, and G. Candiani, “Foundations of biomaterials engineering,” *Found. Biomater. Eng.*, pp. 1–572, Jan. 2019, doi: 10.1016/C2015-0-05967-6.

[9] Z. M. Dang, J. K. Yuan, J. W. Zha, T. Zhou, S. T. Li, and G. H. Hu, “Fundamentals, processes and applications of high-permittivity polymer–matrix composites,” *Prog. Mater. Sci.*, vol. 57, no. 4, pp. 660–723, May 2012, doi: 10.1016/J.PMATSCI.2011.08.001.

[10] J. P. Carey, “Introduction to braided composites,” *Handb. Adv. Braided Compos. Mater. Theory, Prod. Test. Appl.*, pp. 1–21, Jan. 2017, doi: 10.1016/B978-0-08-100369-5.00001-

5.

[11] G. W. Melenka and C. Ayranci, “Advanced measurement techniques for braided composite structures: A review of current and upcoming trends,” doi: 10.1177/0021998320903105.

[12] G. W. Melenka and J. P. Carey, “Experimental analysis of diamond and regular tubular braided composites using three-dimensional digital image correlation,” *J. Compos. Mater.*, vol. 51, no. 28, pp. 3887–3907, Dec. 2017, doi: 10.1177/0021998317695418/ASSET/IMAGES/LARGE/10.1177_0021998317695418-FIG2.JPEG.

[13] D. S. Brookstein, “Processing advanced braided composites,” *Adv. Compos. Process. Technol.*, pp. 33–36, 1988.

[14] N. Casale, D. Bristow, and C. M. Pastore, “Design and fabrication of a braided composite monocoque bicycle frame,” *High-tech fibrous Mater. (ACS Symp. Ser. 457)*, 1991, doi: 10.1021/BK-1991-0457.CH006.

[15] W. Hao, Z. Huang, L. Zhang, G. Zhao, and Y. Luo, “Study on the torsion behavior of 3-D braided composite shafts,” *Compos. Struct.*, vol. 229, p. 111384, Dec. 2019, doi: 10.1016/J.COMPSTRUCT.2019.111384.

[16] G. W. Melenka *et al.*, “Manufacturing processes for braided composite materials,” *Handb. Adv. Braided Compos. Mater. Theory, Prod. Test. Appl.*, pp. 47–153, Jan. 2017, doi: 10.1016/B978-0-08-100369-5.00003-9.

[17] C. Ayranci and J. Carey, “2D braided composites: A review for stiffness critical applications,” *Compos. Struct.*, vol. 85, no. 1, pp. 43–58, Sep. 2008, doi:

10.1016/J.COMPSTRUCT.2007.10.004.

[18] C. Cerbu, S. Ursache, M. F. Botis, and A. Hadăr, “Simulation of the Hybrid Carbon-Aramid Composite Materials Based on Mechanical Characterization by Digital Image Correlation Method,” *Polym. 2021, Vol. 13, Page 4184*, vol. 13, no. 23, p. 4184, Nov. 2021, doi: 10.3390/POLYM13234184.

[19] I. Emami Tabrizi, B. Alkhateab, J. Seyyed Monfared Zanjani, and M. Yildiz, “Using digital image correlation for in situ strain and damage monitoring in hybrid fiber laminates under in-plane shear loading,” *Polym. Compos.*, vol. 42, no. 8, pp. 4029–4042, Aug. 2021, doi: 10.1002/PC.26114.

[20] C. C. Chamis, R. F. Lark, and J. H. Sinclair, *Mechanical property characterization of intraply hybrid composites*. ASTM International, 1981.

[21] Y. Swolfs, L. Gorbatikh, and I. Verpoest, “Fibre hybridisation in polymer composites: A review,” *Compos. Part A Appl. Sci. Manuf.*, vol. 67, pp. 181–200, Dec. 2014, doi: 10.1016/J.COMPOSITESA.2014.08.027.

[22] B. Ruban Rajasekar, R. Asokan, M. Senbagan, R. Karthika, K. Sivajyothi, and N. Sharma, “Evaluation on mechanical properties of intra-ply hybrid carbon-aramid/epoxy composite laminates,” *Mater. Today Proc.*, vol. 5, no. 11, pp. 25323–25330, Jan. 2018, doi: 10.1016/J.MATPR.2018.10.335.

[23] A. Wagih, T. A. Sebaey, A. Yudhanto, and G. Lubineau, “Post-impact flexural behavior of carbon-aramid/epoxy hybrid composites,” *Compos. Struct.*, vol. 239, p. 112022, May 2020, doi: 10.1016/J.COMPSTRUCT.2020.112022.

[24] G. Pincheira, C. Canales, C. Medina, E. Fernández, and P. Flores, “Influence of aramid fibers on the mechanical behavior of a hybrid carbon–aramid–reinforced epoxy composite,” *Proc. Inst. Mech. Eng. Part L J. Mater. Des. Appl.*, vol. 232, no. 1, pp. 58–66, Jan. 2018, doi: 10.1177/1464420715612827/ASSET/IMAGES/LARGE/10.1177_1464420715612827-FIG2.JPEG.

[25] S. Singh, G. Singh, C. Prakash, and S. Ramakrishna, “Current status and future directions of fused filament fabrication,” *J. Manuf. Process.*, vol. 55, pp. 288–306, Jul. 2020, doi: 10.1016/J.JMAPRO.2020.04.049.

[26] L. Jyothish Kumar and C. G. Krishnadas Nair, “Current trends of additive manufacturing in the aerospace industry,” in *Advances in 3D Printing and Additive Manufacturing Technologies*, Springer Singapore, 2016, pp. 39–54.

[27] P. Wu, J. Wang, and X. Wang, “A critical review of the use of 3-D printing in the construction industry,” *Autom. Constr.*, vol. 68, pp. 21–31, Aug. 2016, doi: 10.1016/J.AUTCON.2016.04.005.

[28] J. S. Chohan and R. Singh, “Enhancing dimensional accuracy of FDM based biomedical implant replicas by statistically controlled vapor smoothing process,” *Prog. Addit. Manuf. 2016 11*, vol. 1, no. 1, pp. 105–113, Apr. 2016, doi: 10.1007/S40964-016-0009-4.

[29] I. El-Katatny, S. H. Masood, and Y. S. Morsi, “Error analysis of FDM fabricated medical replicas,” doi: 10.1108/13552541011011695.

[30] D. Wu, A. Spanou, A. Diez-Escudero, and C. Persson, “3D-printed PLA/HA composite structures as synthetic trabecular bone: A feasibility study using fused deposition

modeling," *J. Mech. Behav. Biomed. Mater.*, vol. 103, p. 103608, Mar. 2020, doi: 10.1016/J.JMBBM.2019.103608.

[31] G. W. Melenka, B. K. O. Cheung, J. S. Schofield, M. R. Dawson, and J. P. Carey, "Evaluation and prediction of the tensile properties of continuous fiber-reinforced 3D printed structures," *Compos. Struct.*, vol. 153, pp. 866–875, 2016, doi: 10.1016/j.compstruct.2016.07.018.

[32] H. He and K. Molnár, "Fabrication of 3D printed nanocomposites with electrospun nanofiber interleaves," *Addit. Manuf.*, vol. 46, p. 102030, Oct. 2021, doi: 10.1016/J.ADDMA.2021.102030.

[33] M. Mohammadizadeh and I. Fidan, "Tensile Performance of 3D-Printed Continuous Fiber-Reinforced Nylon Composites," *J. Manuf. Mater. Process. 2021, Vol. 5, Page 68*, vol. 5, no. 3, p. 68, Jun. 2021, doi: 10.3390/JMMP5030068.

[34] I. Blanco, "The Use of Composite Materials in 3D Printing," *J. Compos. Sci. 2020, Vol. 4, Page 42*, vol. 4, no. 2, p. 42, Apr. 2020, doi: 10.3390/JCS4020042.

[35] N. Shahrubudin, T. C. Lee, and R. Ramlan, "An Overview on 3D Printing Technology: Technological, Materials, and Applications," *Procedia Manuf.*, vol. 35, pp. 1286–1296, Jan. 2019, doi: 10.1016/J.PROMFG.2019.06.089.

[36] S. Y. Fu, X. Q. Feng, B. Lauke, and Y. W. Mai, "Effects of particle size, particle/matrix interface adhesion and particle loading on mechanical properties of particulate–polymer composites," *Compos. Part B Eng.*, vol. 39, no. 6, pp. 933–961, Sep. 2008, doi: 10.1016/J.COMPOSITESB.2008.01.002.

[37] L. Vásárhelyi, Z. Kónya, Kukovecz, and R. Vajtai, “Microcomputed tomography–based characterization of advanced materials: a review,” *Materials Today Advances*, vol. 8. Elsevier Ltd, p. 100084, Dec. 01, 2020, doi: 10.1016/j.mtadv.2020.100084.

[38] M. J. Paulus, S. S. Gleason, S. J. Kennel, P. R. Hunsicker, and D. K. Johnson, “High Resolution X-ray Computed Tomography: An Emerging Tool for Small Animal Cancer Research,” *Neoplasia*, vol. 2, no. 1–2, pp. 62–70, Jan. 2000, doi: 10.1038/SJ.NEO.7900069.

[39] N. Rana, D. Rawat, M. Parmar, D. Dhawan, A. Bhati, and B. Mittal, “Evaluation of external beam hardening filters on image quality of computed tomography and single photon emission computed tomography/computed tomography,” *J. Med. Phys.*, vol. 40, no. 4, p. 198, Oct. 2015, doi: 10.4103/0971-6203.170790.

[40] G. Ruben, L. C. P. Croton, D. M. Paganin, K. S. Morgan, and M. J. Kitchen, “Ring artifact suppression in X-ray computed tomography using a simple, pixel-wise response correction,” *Opt. Express, Vol. 27, Issue 10, pp. 14231-14245*, vol. 27, no. 10, pp. 14231–14245, May 2019, doi: 10.1364/OE.27.014231.

[41] D. N. H. Thanh, V. B. S. Prasath, and L. M. Hieu, “A review on CT and X-ray images denoising methods,” *Inform.*, vol. 43, no. 2, pp. 151–159, 2019, doi: 10.31449/INF.V43I2.2179.

[42] C. S. Timpano and G. W. Melenka, “Digital volume correlation analysis of polylactic acid based fused filament fabrication printed composites:,” *https://doi.org/10.1177/00219983211020500*, May 2021, doi: 10.1177/00219983211020500.

[43] A. Murali, M. A. Vakkattil, and R. Parameswaran, “Investigating the Effect of Processing

Parameters on Mechanical Behavior of 3D Fused Deposition Modeling Printed Polylactic Acid," *J. Mater. Eng. Perform.*, pp. 1–14, Aug. 2022, doi: 10.1007/S11665-022-07188-3/TABLES/6.

[44] S. Sommacal, A. Matschinski, K. Drechsler, and P. Compston, "Characterisation of void and fiber distribution in 3D printed carbon-fiber/PEEK using X-ray computed tomography," *Compos. Part A Appl. Sci. Manuf.*, vol. 149, p. 106487, Oct. 2021, doi: 10.1016/J.COMPOSITESA.2021.106487.

[45] S. Yu, H. Bale, S. Park, J. Y. Hwang, and S. H. Hong, "Anisotropic microstructure dependent mechanical behavior of 3D-printed basalt fiber-reinforced thermoplastic composites," *Compos. Part B Eng.*, vol. 224, p. 109184, Nov. 2021, doi: 10.1016/J.COMPOSITESB.2021.109184.

[46] G. W. Melenka and A. Gholami, "Fiber identification of braided composites using micro-computed tomography," *Compos. Commun.*, vol. 27, p. 100813, Oct. 2021, doi: 10.1016/J.COCO.2021.100813.

[47] Y. Gu *et al.*, "Torsion damage mechanisms analysis of two-dimensional braided composite tubes with digital image correction and X-ray micro-computed tomography," *Compos. Struct.*, vol. 256, p. 113020, Jan. 2021, doi: 10.1016/J.COMPSTRUCT.2020.113020.

[48] L. Shi, Z. Wu, X. Cheng, Z. Pan, and Y. Yuan, "Transverse impact response of hybrid biaxial/uniaxial braided composite tubes," *Eng. Struct.*, vol. 244, p. 112816, Oct. 2021, doi: 10.1016/J.ENGSTRUCT.2021.112816.

[49] H.-F. Yin, W. Zhou, P.-F. Zhang, and L.-H. Ma, "Flexural progressive damage and failure behavior of carbon-aramid/epoxy hybrid woven composites," doi:

10.1177/0021998320962187.

[50] R. A. Naik, P. G. Ifju, and J. E. Masters, “Effect of Fiber Architecture Parameters on Deformation Fields and Elastic Moduli of 2-D Braided Composites,” *http://dx.doi.org/10.1177/002199839402800705*, vol. 28, no. 7, pp. 656–681, Jul. 2016, doi: 10.1177/002199839402800705.

[51] H. Schreier, J. J. Orteu, and M. A. Sutton, “Image correlation for shape, motion and deformation measurements: Basic concepts, theory and applications,” *Image Correl. Shape, Motion Deform. Meas. Basic Concepts,Theory Appl.*, pp. 1–321, 2009, doi: 10.1007/978-0-387-78747-3/COVER.

[52] B. Pan, K. Qian, H. Xie, and A. Asundi, “Two-dimensional digital image correlation for in-plane displacement and strain measurement: a review,” *Meas. Sci. Technol.*, vol. 20, no. 6, p. 062001, Apr. 2009, doi: 10.1088/0957-0233/20/6/062001.

[53] Y. L. Dong and B. Pan, “A Review of Speckle Pattern Fabrication and Assessment for Digital Image Correlation,” *Exp. Mech. 2017 578*, vol. 57, no. 8, pp. 1161–1181, May 2017, doi: 10.1007/S11340-017-0283-1.

[54] D. Lecompte *et al.*, “Quality assessment of speckle patterns for digital image correlation,” *Opt. Lasers Eng.*, vol. 44, no. 11, pp. 1132–1145, Nov. 2006, doi: 10.1016/J.OPTLASENG.2005.10.004.

[55] B. Pan, “Recent Progress in Digital Image Correlation,” *Exp. Mech.*, vol. 51, no. 7, pp. 1223–1235, Sep. 2011, doi: 10.1007/S11340-010-9418-3/FIGURES/6.

[56] B. Pan, H. M. Xie, B. Q. Xu, and F. L. Dai, “Performance of sub-pixel registration

algorithms in digital image correlation," *Meas. Sci. Technol.*, vol. 17, no. 6, p. 1615, May 2006, doi: 10.1088/0957-0233/17/6/045.

[57] H. A. Bruck, S. R. McNeill, M. A. Sutton, and W. H. Peters, "Digital image correlation using Newton-Raphson method of partial differential correction," *Exp. Mech. 1989 293*, vol. 29, no. 3, pp. 261–267, Sep. 1989, doi: 10.1007/BF02321405.

[58] H. Gonabadi, A. Yadav, and S. J. Bull, "The effect of processing parameters on the mechanical characteristics of PLA produced by a 3D FFF printer," *Int. J. Adv. Manuf. Technol.*, vol. 111, no. 3–4, pp. 695–709, Nov. 2020, doi: 10.1007/S00170-020-06138-4/FIGURES/12.

[59] R. J. Zaldivar, D. B. Witkin, T. McLouth, D. N. Patel, K. Schmitt, and J. P. Nokes, "Influence of processing and orientation print effects on the mechanical and thermal behavior of 3D-Printed ULTEM® 9085 Material," *Addit. Manuf.*, vol. 13, pp. 71–80, Jan. 2017, doi: 10.1016/J.ADDMA.2016.11.007.

[60] C. K. Leung, G. W. Melenka, D. S. Nobes, and J. P. Carey, "The effect on elastic modulus of rigid-matrix tubular composite braid radius and braid angle change under tensile loading," *Compos. Struct.*, vol. 100, pp. 135–143, Jun. 2013, doi: 10.1016/J.COMPSTRUCT.2012.12.038.

[61] A. Armanfard and G. W. Melenka, "Experimental evaluation of carbon fibre, fibreglass and aramid tubular braided composites under combined tension–torsion loading," *Compos. Struct.*, vol. 269, p. 114049, Aug. 2021, doi: 10.1016/J.COMPSTRUCT.2021.114049.

[62] A. Buljac *et al.*, "Digital Volume Correlation: Review of Progress and Challenges," *Exp. Mech.*, vol. 58, no. 5, pp. 661–708, Jun. 2018, doi: 10.1007/s11340-018-0390-7.

[63] B. Pan and B. Wang, “Some recent advances in digital volume correlation,” *Opt. Lasers Eng.*, vol. 135, p. 106189, Dec. 2020, doi: 10.1016/J.OPTLASENG.2020.106189.

[64] B. K. Bay, T. S. Smith, D. P. Fyhrie, and M. Saad, “Digital volume correlation: Three-dimensional strain mapping using X-ray tomography,” *Exp. Mech. 1999 393*, vol. 39, no. 3, pp. 217–226, 1999, doi: 10.1007/BF02323555.

[65] J. Réthoré, S. Roux, and F. Hild, “From pictures to extended finite elements: extended digital image correlation (X-DIC),” *Comptes Rendus Mécanique*, vol. 335, no. 3, pp. 131–137, Mar. 2007, doi: 10.1016/J.CRME.2007.02.003.

[66] E. Bar-Kochba, J. Toyjanova, E. Andrews, K. S. Kim, and C. Franck, “A Fast Iterative Digital Volume Correlation Algorithm for Large Deformations,” *Exp. Mech.*, vol. 55, no. 1, pp. 261–274, Jan. 2015, doi: 10.1007/s11340-014-9874-2.

[67] J. Yang, L. Hazlett, A. K. Landauer, and C. Franck, “Augmented Lagrangian Digital Volume Correlation (ALDVC),” *Exp. Mech.*, vol. 60, no. 9, pp. 1205–1223, Nov. 2020, doi: 10.1007/s11340-020-00607-3.

[68] “Welcome to spam’s documentation! — spam 0.6.1.3 documentation.” https://ttk.gricad-pages.univ-grenoble-alpes.fr/spam/index.html (accessed Nov. 23, 2022).

[69] E. Tudisco, E. Andò, R. Cailletaud, and S. A. Hall, “TomoWarp2: A local digital volume correlation code,” *SoftwareX*, vol. 6, pp. 267–270, Jan. 2017, doi: 10.1016/J.SOFTX.2017.10.002.

[70] B. P. Croom, H. Jin, B. Mills, and X. Li, “Effect of Fragile Speckle Patterns on Accuracy of Digital Volume Correlation,” *Exp. Mech.*, vol. 59, no. 7, pp. 991–1005, Sep. 2019, doi:

10.1007/S11340-019-00512-4/FIGURES/12.

[71] B. P. Croom *et al.*, “Interlaboratory Study of Digital Volume Correlation Error Due to X-Ray Computed Tomography Equipment and Scan Parameters: an Update from the DVC Challenge,” *Exp. Mech.*, vol. 61, no. 2, pp. 395–410, Feb. 2021, doi: 10.1007/S11340-020-00653-X/FIGURES/10.

[72] C. S. Timpano and G. W. Melenka, “Artificial seeding for micro-computed tomography image contrast enhancement for digital volume correlation,” *Compos. Part B Eng.*, vol. 215, p. 108809, Jun. 2021, doi: 10.1016/J.COMPOSITESB.2021.108809.

[73] B. Wang, L. Sun, and B. Pan, “Mapping internal deformation fields in 3D printed porous structure with digital volume correlation,” *Polym. Test.*, vol. 78, Sep. 2019, doi: 10.1016/j.polymertesting.2019.105945.

[74] G. Melenka, *Digital Volume Correlation Analysis of Braided Composites*. 2018.

[75] J. Holmes, S. Sommacal, Z. Stachurski, R. Das, and P. Compston, “Digital image and volume correlation with X-ray micro-computed tomography for deformation and damage characterisation of woven fibre-reinforced composites,” *Compos. Struct.*, vol. 279, p. 114775, Jan. 2022, doi: 10.1016/J.COMPSTRUCT.2021.114775.

[76] M. Mehdikhani *et al.*, “Digital volume correlation for meso/micro in-situ damage analysis in carbon fiber reinforced composites,” *Compos. Sci. Technol.*, vol. 213, p. 108944, Sep. 2021, doi: 10.1016/J.COMPSCITECH.2021.108944.

[77] C. Liu, Y. Chen, D. Shi, J. Marrow, X. Jing, and X. Yang, “In situ investigation of failure in 3D braided SiCf/SiC composites under flexural loading,” *Compos. Struct.*, vol. 270, p.

114067, Aug. 2021, doi: 10.1016/J.COMPSTRUCT.2021.114067.

[78] C. Cerbu, S. Ursache, M. F. Botis, and A. Hadăr, “Simulation of the Hybrid Carbon-Aramid Composite Materials Based on Mechanical Characterization by Digital Image Correlation Method,” *Polym. 2021, Vol. 13, Page 4184*, vol. 13, no. 23, p. 4184, Nov. 2021, doi: 10.3390/POLYM13234184.

Chapter 3 Mapping Internal Strain Fields of Fused Filament Fabrication Metal Filled Polylactic Acid Structure Using Digital Volume Correlation

3.1 Introduction

With the increasing use of fused filament fabrication (FFF) in various industries, FFF has become the most widely used 3D printing process [1]. FFF is an additive manufacturing (AM) process where a filament is passed through a heated nozzle to form a solid body. Geometry is created from layer-by-layer deposition of molten thermoplastic filament onto a build plate. FFF is widely used for part replacements, prototypes, moulds, and even load-bearing structures like in the field of aeronautics [2], construction [3] and biomedicine [4]–[6]. The materials commonly used are thermoplastic polymers like Polylactic Acid (PLA) or acrylonitrile butadiene styrene (ABS), both of which do not have high strength capacity. Various studies have been done to reinforce PLA or ABS with reinforced materials with fibres or metal particles to improve the strength further [7]. Haijun He *et al.* fabricated a 3D printed nanocomposite using the FFF technique; both the filament and the nanofibres were manufactured with PLA, the latter through electrospinning [8]. It was found that tensile strength of 3d printed nanocomposite with 10.1% nanofibre content increases from 55.6 to 64.8 Mpa, an increase of 16.55%. Mohammadizadeh *et al.* studied on tensile strength of 3D printed fibre reinforced nylon composites [9]. And it was found that carbon fibre (CF) reinforced 3D with a volume fraction of 60% has a tensile strength of 446.87 MPa, which is an increase of 2231% from the strength of nylon and also greater than the strength of Aluminium 6061 which is 290 MPa. These studies clearly show how the introduction of reinforcements improves the strength drastically of FFF structures.

3D printed parts with reinforced material require an understanding of internal microstructure for which Micro-Computed Tomography (Micro-CT) is ideally suited. Micro-CT

is a non-destructive method that uses X-rays to image the internal microstructure of an object [10]. The X-ray beams are ejected through the X-ray tube towards the sample. The resulting image is based on the attenuation coefficient of material. The attenuation coefficient is the measure of how easily beams are absorbed and transmitted with different intensities [11]. The detectors are placed at the end, which collect the transmitted X-rays, which is the 2D projection of the sample. The sample is rotated 180 or 360 degrees to acquire numerous projections from different angles. After the projections are collected, an image reconstruction process is used to give a stack of a cross-sectional image of the sample. S Sommacal *et al.* used Micro-CT to understand the voids in a 3D printed carbon reinforced PEEK sample and the filament feedstock [12]. The paper finds that the printing process had a minor effect in removing the voids present in the filaments. However, the depositional printing process greatly affected the internal microstructure in terms of void and fibres distribution. Yu *et al.* examined the microstructure of basalt fibre reinforced PLA using Micro-CT [13]. The result shows the effect of printing direction on the voids formation as well as microstructural anisotropy which can lead to customized elastic modulus depending upon the printing direction.

AM parts have complex structures with different printing parameters. Printing parameters include raster orientation, infill percentage, and layer height. Due to these factors, the mechanical properties of AM parts are highly dependent on printing parameters [14], [15]. To understand the behaviour of printing parameters on loading conditions, various surface measurement techniques like Digital Image Correlation (DIC) have been used [16], [17]. DIC is a contact-free optical measurement technique to measure a specimen's outer surface deformation and strain fields. However, DIC has limitations. For example, surface deformation behaviour does not correlate with the internal microstructure of the FFF part. H Gonabadi *et al.* studied the effect of build orientation

and infill density and pattern using DIC [18]. They used a single camera for the acquisition of images during tensile and shear testing. The authors found that 0° on-edge build orientation, which is a specimen manufactured on the edge of the sides with the plate support instead of a face, has better mechanical properties than other build orientations. But the mechanical behaviour for different infill patterns was similar. The increase in infill density leads to an increase in tensile properties in a quadratic manner. It does not depict the true microscopic behaviour inside the sample which is more prone to failure than the shell. Therefore, there is a need for full-field strain measurement, which correlates strain and deformation behaviour with the internal microstructure of FFF components.

Digital Volume Correlation (DVC) is an advanced measurement technique to measure the 3D deformation and strain of an object; DVC is similar to DIC but in a 3D space. DVC can use volumetric data such as X-ray CT or magnetic resonance imaging (MRI) data to measure deformation and strain [19], [20]. DVC was first developed by Bay *et al.* on a trabecular bone placed under compressed loading to study the internal strain[21]. DVC was initially used for biomechanical applications and later extended to solid mechanics[19]. Wang *et al*. used DVC for a porous 3D structure printed using stereolithography to find the deformation fields and relate the microstructure with the macrostructure [22]. Timpano *et al.* studied the full field internal displacement and the strain tensor of 100% infill density FFF sample with +45/-45° raster orientation [23]. The result shows the development of strains along the internal raster of printed sample. Despite initial work on the examination of FFF samples using the DVC method, further investigation using this technique is required.

The paper aims to study the effects of 20, 40, 60 and 80% infill percentage on a FFF part. This is achieved with the help of a Micro-CT machine and integrated testing stage to capture the

cross-sectional images of a specimen under tensile loading of 50N with a step loading of 150N. After collecting Micro-CT image data, the DVC method will correlate different infill percentages to map full-field volumetric deformation and strain fields. The study will provide great insight into the complex structure of FFF, and relation of microstructure with macrostructure behaviour can be established. Further, it can be used to support the validation Finite Element Analysis models for FFF specimen.

3.2 Methodology

3.2.1 3D Printing

A modified ASTM D638-14 type V, as shown in Figure 3-1(a), was modelled for the given analysis. A solid model is generated using the given dimensions in CAD software (Solidworks 2020, Dassault Systèmes, France). Then the file is imported into a 3D printing software (Prusa Slicer 2.2.0, Czech Republic) to define printing parameters like infill percentage and layer thickness described below in Table 3-1. Based on the parameters, specimens with 20, 40, 60 and 80 infill percentages are printed using an open-source 3D printer (Prusa i3 MK2, Czech Republic) by FFF. The filament used for printing is copper metal particle reinforced PLA (Metal filled PLA, CCTree-Mech Solutions LTD, Concord, Ontario). Figure 3-1(b) describes the cross-sectional view of the specimen and Figure 3-1(c) highlights the internal raster orientation between 20, 40, 60 and 80 infill percentages.

Table 3-1: 3D Printing Parameters.

Parameters	Copper Filled PLA
Layer Thickness	0.1 mm
Top/Bottom Layer	0.8 mm
Shell Thickness	0.4 mm
Infill %	20,40,60,80
Support	Raft
Orientation	+45°/-45°
Nozzle Temperature	200°C
Build Plate Temperature	60°C

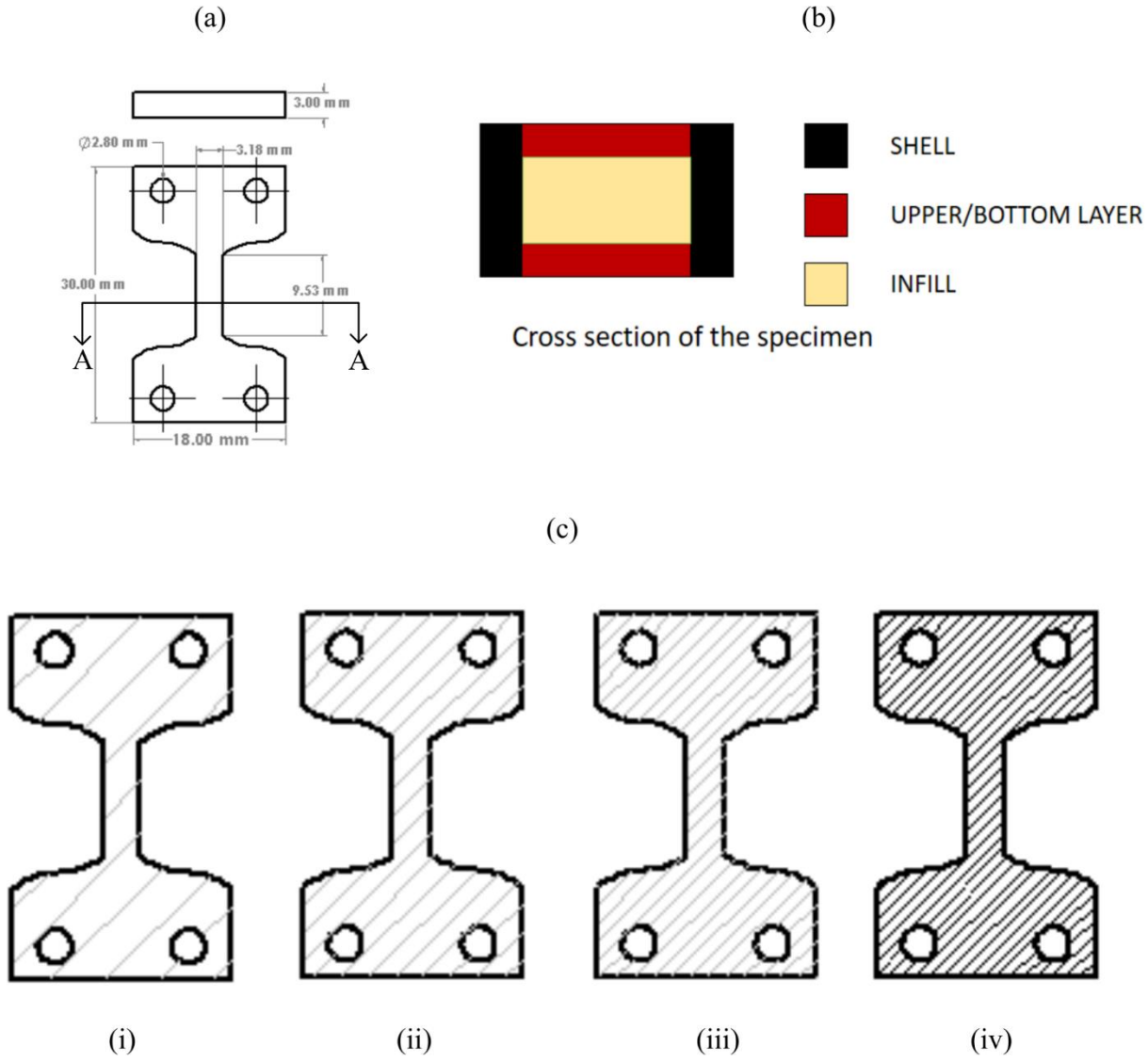

Figure 3-1: (a) Modified ASTM D638-14 type V Dimensions (b) shows the cross-section of geometry which includes shell, upper/bottom layer and infill region (c) Infill pattern of (i) 20% (ii) 40% (iii) 60% (iv) 80%.

3.2.2 Microscopic Image

A magnified image of a 3D printed part section with infill patterns was captured using a microscope (Elikliv DM4, China). Cross-section images were captured to verify the Micro-CT results and to provide initial insights into the cross-section of the FFF components. The narrow

section of the structure with 60% grid infill pattern was captured, as shown in Figure 3-2(a). The image was first converted into an 8-bit grayscale image, and using ImageJ (National Institutes of Health, Bethesda, Maryland, USA) ROI manager, the pore boundary was drawn manually. Further, using overlay and mask in-built function, the final image with pores in the white and solid region in black was generated as shown in Figure 3-2(b). The porosity of the 2D image was calculated for a 60% grid infill pattern using image processing software CTAN (1.16, Bruker, Belgium).

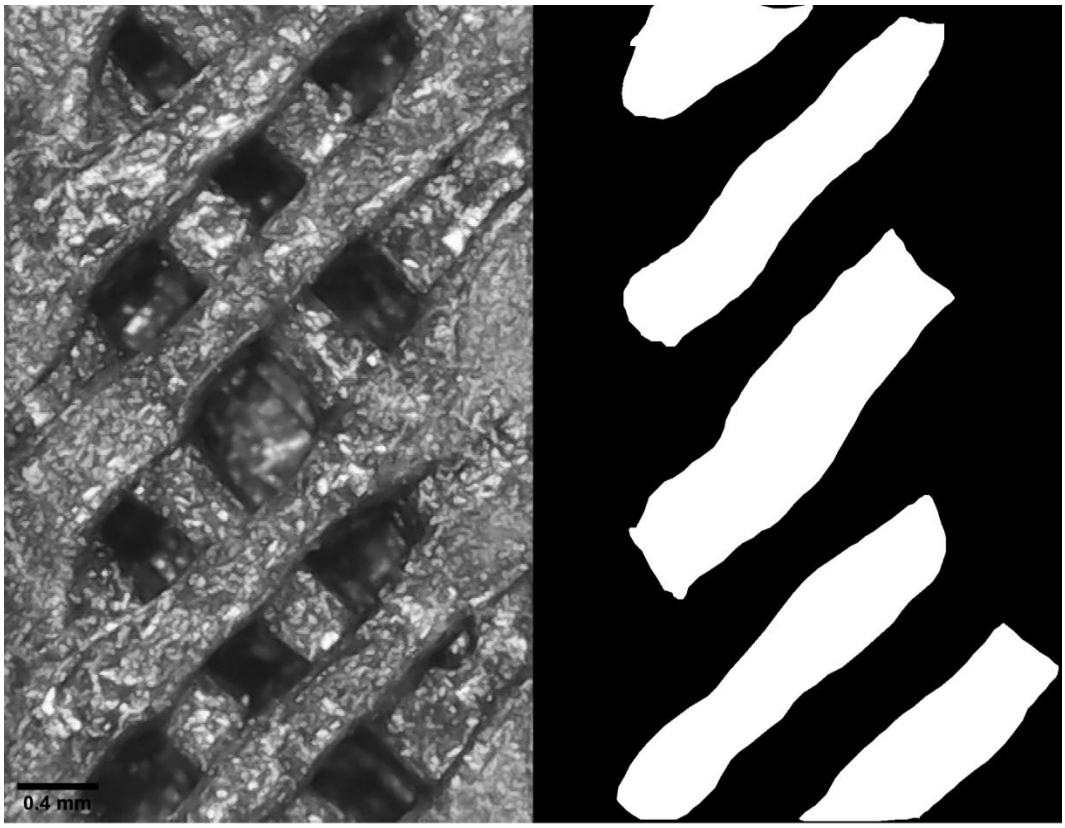

Figure 3-2: (a) Captured front view microscopic image of 60% infill part (b) Final masked image for calculating porosity.

3.2.3 Micro-CT Scans

X-ray Micro-CT was conducted using a desktop machine (Skyscan 1272 microCT, Bruker, Belgium). The specimen was mounted on the material testing stage (Tension and Compression stage, Bruker, 440N) inside the Micro-CT machine. Various parameters need to be set before the acquisition of a 3D image. Based on the specimen dimension and expected deformation, a pixel size of 5.4 μm has been selected with a resolution of 1468 x 1468 x 1561 pixels. This gives an effective field of view of 7.93 mm x 7.93 mm x 8.42 mm. Only voltage settings will be defined based on which current is automatically calculated. A voltage of 70KV is selected, and a 1mm aluminum filter is applied based on recommended settings for the SkyScan 1272 machine. The added aluminum filter eliminates artifacts and noise from forming in the sample images. Frame averaging of 4 with 2x2 binning mode has been selected. During the acquisition of images from Micro-CT, multiple images can be captured at each rotation step, averaged out to give the final image known as frame averaging, which leads to increase in the signal to noise ratio. Binning is the process of combining pixels to form a larger pixel, for 2x2 binning mode, a matrix of 2x2 pixels is combined to create a single pixel which leads to increase in signal to noise ratio. The rotation step corresponds to the increments the sample will be rotated for each scan. The rotation step affects the total scan time. Based on the recommendation by the manufacturer, a rotation step of 0.4° has been selected. A scan rotation of 360° is set, which defines the total rotation of the sample throughout the acquisition. The scan settings for the Micro-CT are summarized in Table 3-2.

Table 3-2: Micro-CT Scan parameters.

Micro-CT Parameter	Setting
Source Voltage	70 kV
Source Current	1 mm
Resolution	1468 px x 1468 px x 1561 px
Pixel size	5.4 μm
Filter	1 mm Al
Binning	2 x 2
Frame Averaging	4
Rotation step	0.4°

Material Testing Stage (440 N integrated test stage, MTS2, Bruker, Belgium) parameters are adjusted after setting up the specification of scans. First, the load cell platen is fully extended. The sample is loaded into the sample holder, and then the sample holder is placed over the chuck in MTS, as shown in Figure 3-3. For the tensile test, the MTS is operated in tensile mode, and the load is increased slightly. Batch scanning is done to obtain multiple scans of the same object during deformation. A preload of 50N was applied so that the sample remained rigid, and a step load of 150N was applied. A delay of 180s is used to ensure consistent results between loading steps.

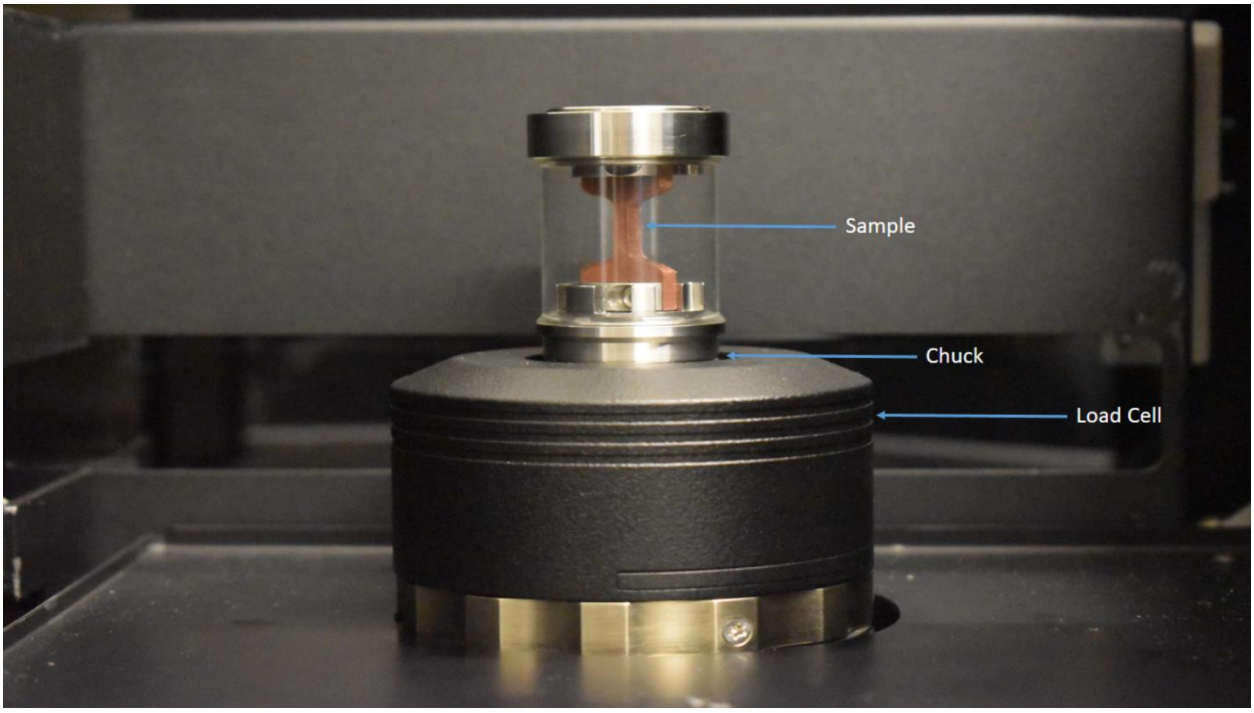

Figure 3-3: Setup view of Material testing stage inside the Micro-CT.

After the scans, reconstruction of Micro-CT data begins. A reconstruction software (Nrecon version 1.7.1.0, Bruker, Belgium) is used for processing and reconstruction of the acquired images. Various filters can be applied based on the artifacts to remove them. Ring artifact correction of 4 and beam hardening correction of 50% was used. Smoothing or blurring can be used to reduce noise in the image. Figure 3-4 shows the reconstruction of Micro-CT data from the specimen. The small volume of interest (VOI) region is captured and reconstructed to get the top view slices of VOI. It shows how the slice plane is generated from the specimen which would help to understand Figure 3-5. Figure 3-5 shows cross-sectional view of 20, 40, 60 and 80 infill percentages specimen. This allows for specimen characteristics such as air gap, material distribution and particle distribution to be investigated. This figure also shows the different raster formation in different infill percentages. Image registration software (DataViewer, Bruker, Belgium) was used to reorient the image boundary line with the axis. The software takes the cross-

sectional image stack as input and provides three views of the sample i.e. Coronal, Sagittal and Transverse plane. It allows to reorient the image in one plane and automatically reorients in other plane.

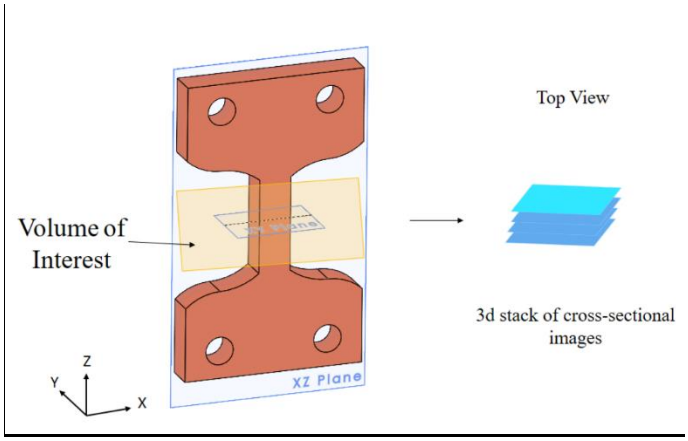

Figure 3-4: Schematic of image reconstruction from Micro-CT.

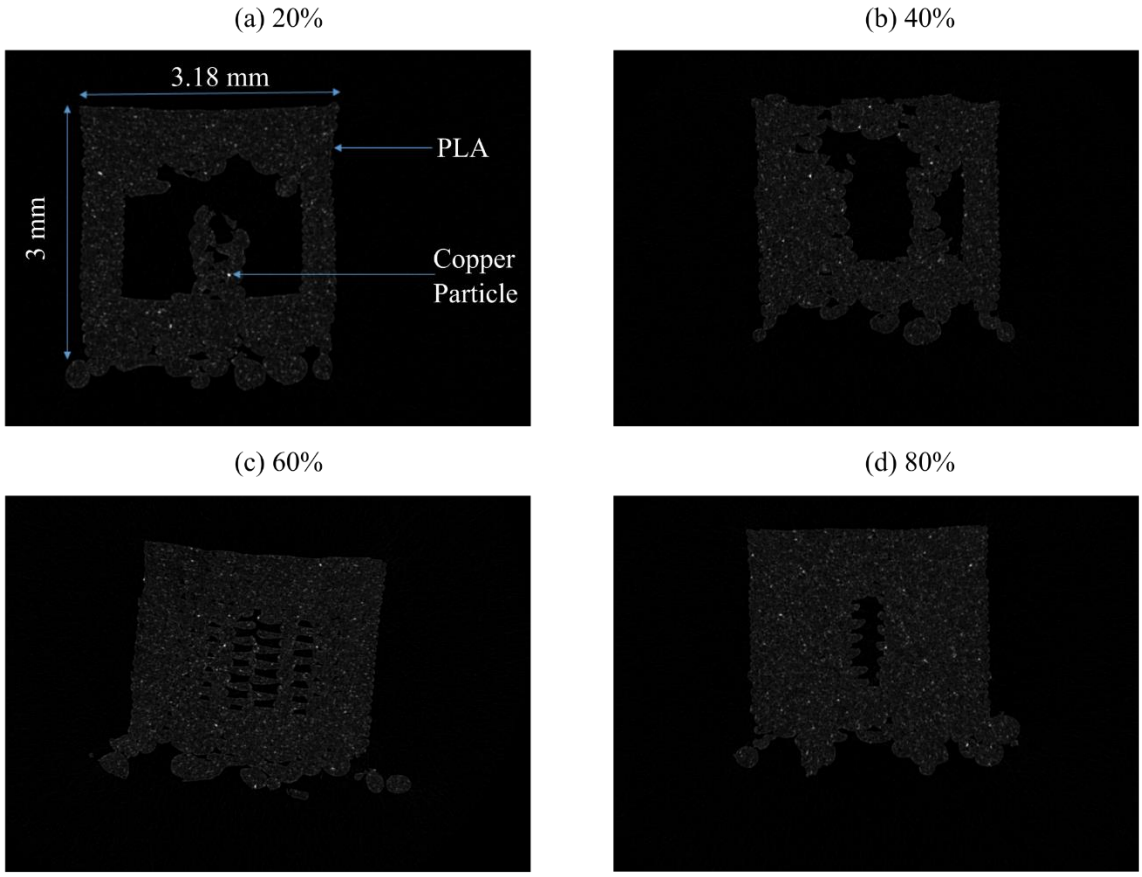

Figure 3-5: Cross sectional top view images using micro-CT of 3D printed dog bone structure with (a) 20% (b) 40% (c) 60% and (d) 80% infill.

3.2.4 Porosity and Particle Distribution Analysis

Pre-processing of the acquired images was done to understand the particle size distribution and porosity of the samples. The above results will help in the analysis of the specimen. CTAn (Bruker, Belgium) software was used for all the image pre-processing. For the porosity analysis, the images are reconstructed to obtain the Front View using Dataviewer software, as seen in Figure 3-6. The front view allows for the porosity of the samples to be investigated in the same orientation as the specimen were fabricated. Front view makes it easier to do the image processing and further distinguish between the shell and infill region. This shows the process of image reconstruction for

further pre-processing analysis. The images are further sliced to get the front view and examine the only raster part for the analysis using software (Dataviewer, Bruker, Belgium), as seen in Figure 3-6 and Figure 3-7(a). The image contains both the infill and shell region, and to obtain the porosity measurement, only the infill region is required. So, the region of interest is defined manually, which is denoted by red colour to get the infill region, as shown in Figure 3-7(b). Then a median filter of radius 3 is applied to the region of interest to filter out noise, as seen in Figure 3-7(c), and then a threshold of 6 is used to obtain the final image, as shown in Figure 3-7(d). White is the region of material, and black is the porous area. A built-in "3D analysis module" in CTAn was used to find the porosity of the sample.

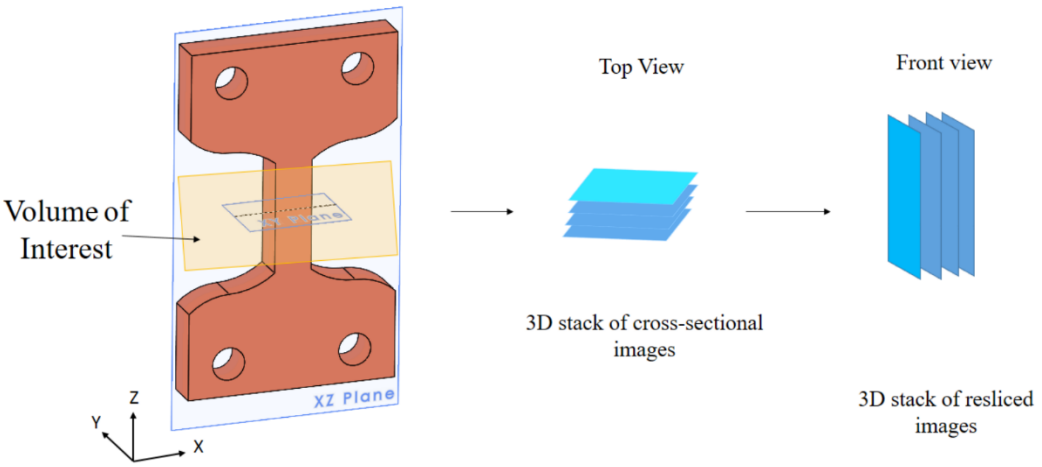

Figure 3-6: Schematic of 3D stack of resliced Images. This figure shows the volume of interest of the sample and the resulting image stack of the volume of interest. The dataset was then resliced to provide images in the front plane of the specimen.

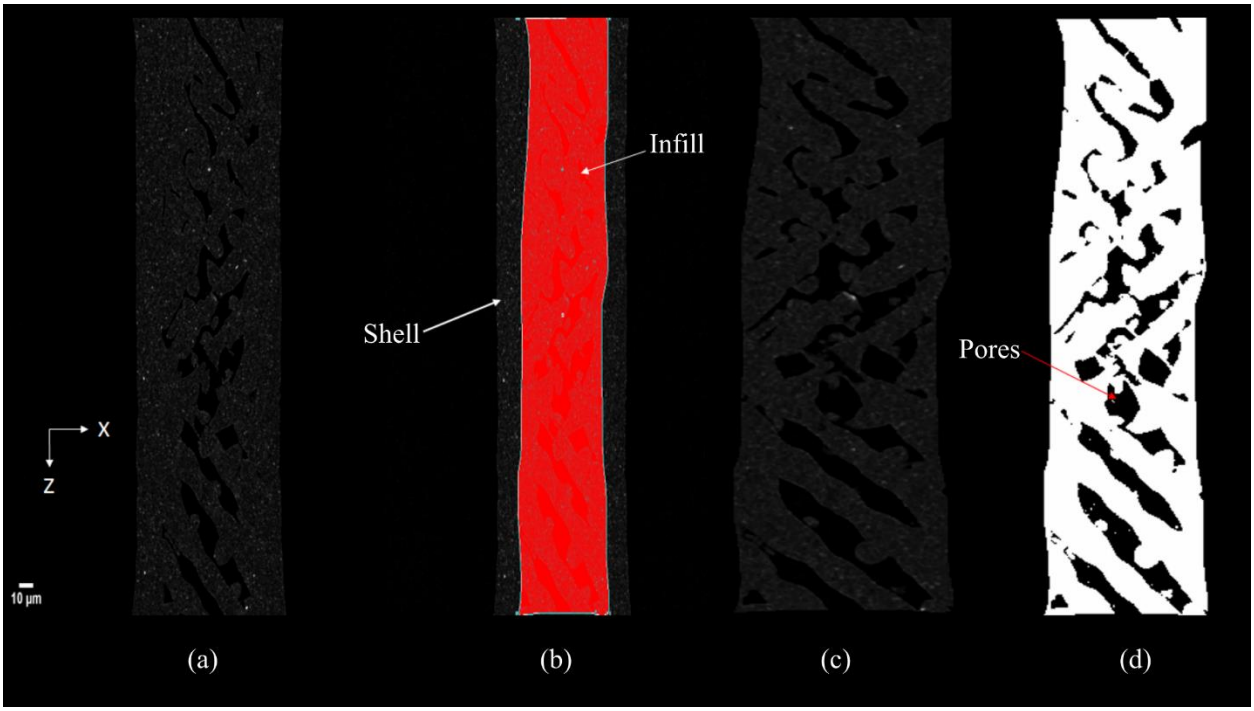

Figure 3-7: Processing steps for calculating porosity using Micro-CT images (a) Reconstruct the images for top view (b) ROI for infill region whose porosity calculation needs to be done (c) Median filter of 3 to clear out noise (d) Threshold of 6 to get the final image with porous region denoted by black.

Figure 3-8 demonstrates the image processing steps for the FFF sample. Figure 3-8(a) shows the original image of the sample, Figure 3-8(b) shows the identified copper particles and Figure 3-8(c) shows the PLA matrix material. A histogram was generated for the particle distribution, as shown in Figure 3-8(d). In general, 0 indicates porous spaces where X-rays did not hit the specimen and 255 means 100% X-ray beams were either absorbed or deflected. The denser the material is, it is tended more toward 255 since absorption will be greater. The objective is to segment both PLA and copper material to find the sample's porosity, particle size and count, respectively. Since copper has higher density than PLA material, a threshold of 42 was applied which gave the copper material in white, as shown in Figure 3-8(b). Different threshold range

helps to provide a distribution of different materials like threshold range of 14 to 42 gave the PLA materials in white as shown in Figure 3-8(c). Using built-in 3D particle analyser, copper particle distribution was found.

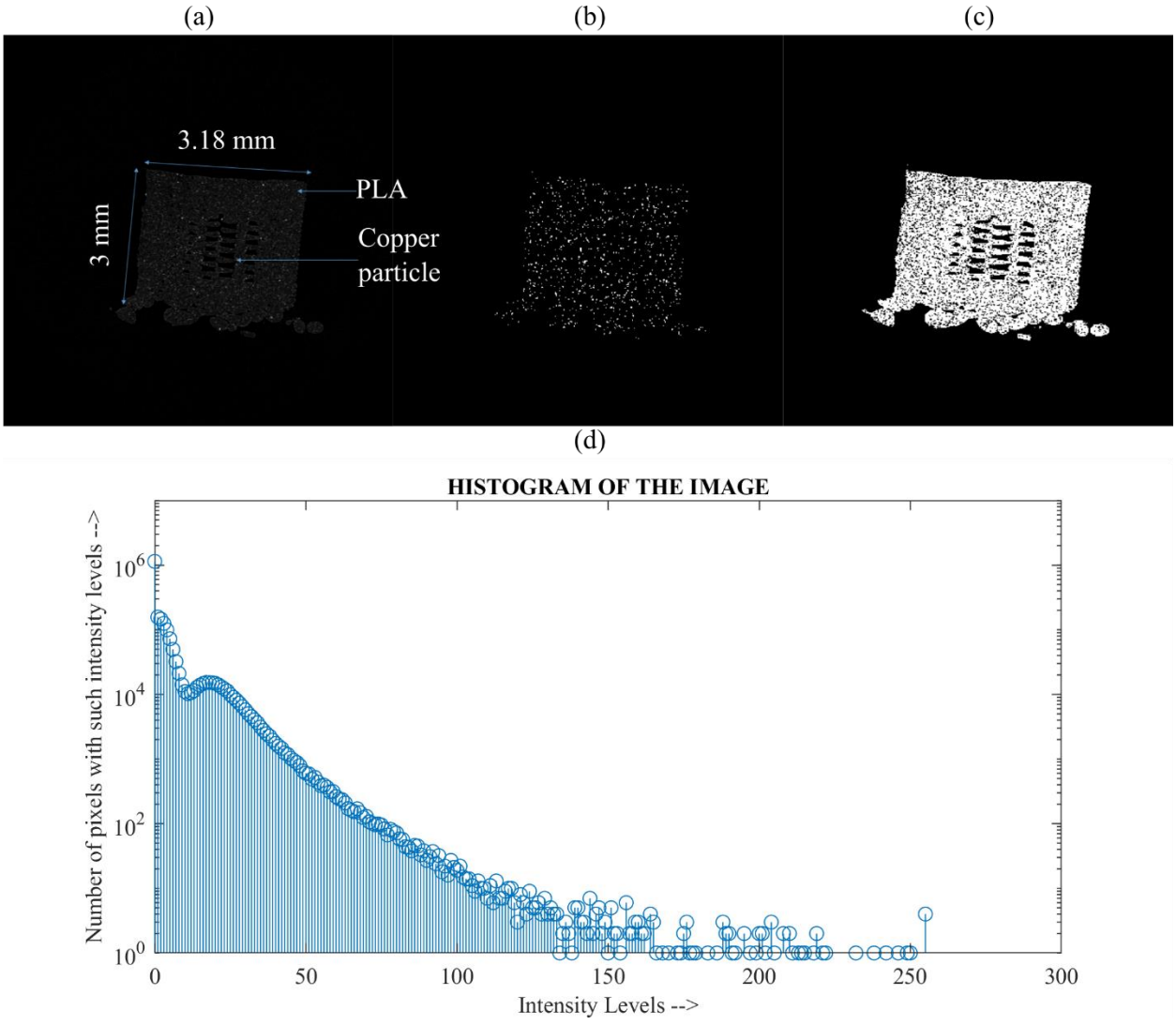

Figure 3-8: (a) Cross sectional top view image 60% infill (b) Copper material distribution using threshold of 42 (c) Threshold image showing PLA material in white colour (d) Histogram of the cross sectional image.

3.2.5 DVC Analysis of FFF Samples

For DVC, a MATLAB-based program (ALDVC 1.0) was used [24]. The program compares the original and deformed images to find the 3D deformation and strain values of the specimen. A server computer (precision T5600, Dell, Round Rock, Texas) with a RAM of 112 GB and two Intel Xeon CPU E5-2680 2701 Mhz 8 core processors has been used for DVC analysis.

Several parameters need to be defined to find volumetric deformation and strains. First is the subset size, a large subset of 128 cubic voxels is initially assumed based on the expected deformation and is iterated to a lower subset based on the best correlation. After the selection of subset size, different voxel spacing or step sizes are used to find the best correlation. Based on this, a final subset size of 64 cubic voxels and 32 (50%) voxel spacing was utilized. For initial guess estimation, zero normalized cross-correlation is used for local correlation since it is most suitable for small deformations, and the finite difference method is used for global correlation, which is the recommended method by the software. The DVC analysis parameters used in this study are summarized in Table 3-3. For strain measurement, the finite difference method is used based on infinitesimal strain.

Table 3-3: Digital Volume Correlation parameter values.

Parameter	Values
Subset size	64 cubic voxels
Subset spacing	32 voxels
Initial Guess Estimation	Zero Normalized cross correlation
Strain Measurement	Infinitesimal strain

3.3 Results and Discussion

3.3.1 Porosity & Particle Distribution

From the pre-processing of the CT images, as shown in Figure 3-9(a) of 60 % infill 3D printed part, it was found that the porosity is 33.97% which is less than the expected porosity of 40%. This might be due to various reasons, the tolerance for the Prusa i3 mk2 printer is insufficient for printing the narrow section of dog bone which is just 2.38 mm in width. Also, it might be because of printing parameters like the speed of the printing or the nozzle size of the printer [25][26]. The current study does not focus on the printing parameters and their optimization. Sofiane *et al.* worked with 100% infill 3D printed Nylon and found large porosity variation across the samples using Micro-CT data analysis [27].

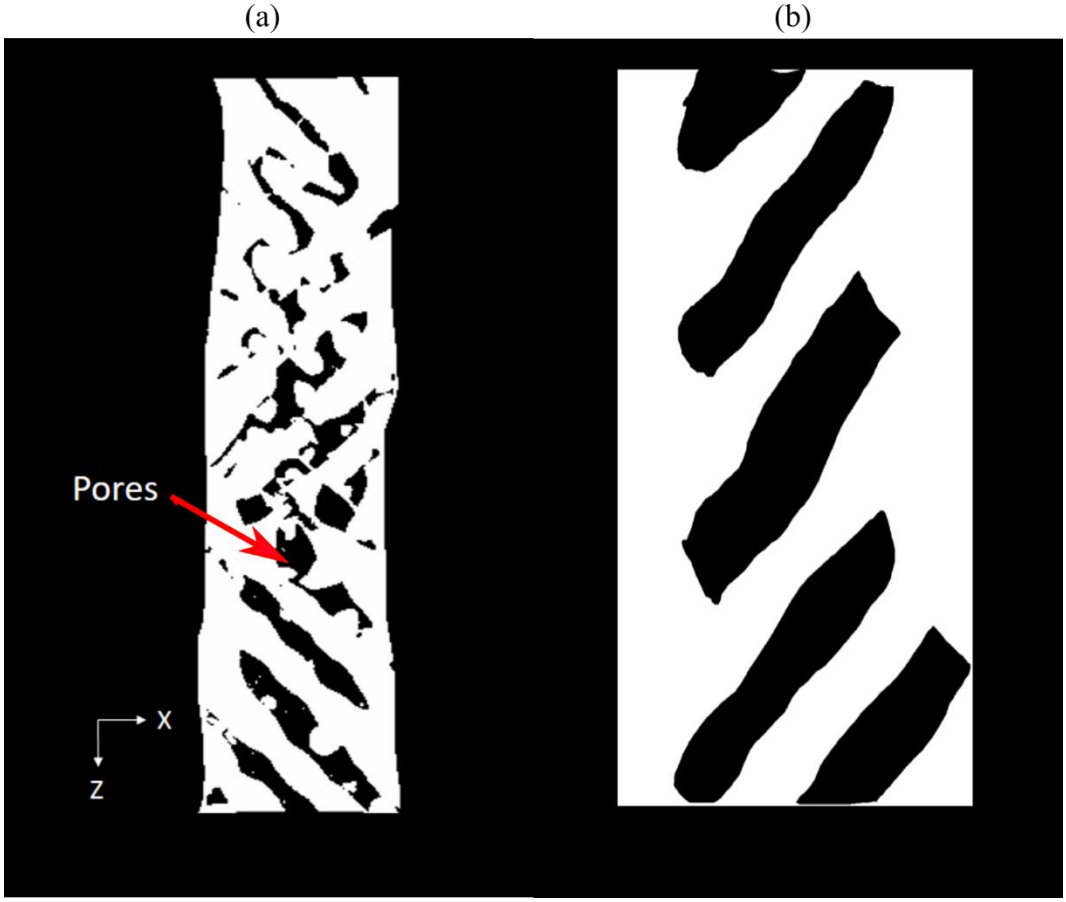

Figure 3-9: (a) Pore distribution on a resliced plane (b) Pore distribution of microscopic image.

To further verify the porosity results, a microscopic image, Figure 3-9(b), of the 60% infill pattern was captured and processed to calculate porosity. The porosity was found to be 31.69% which is in the range of Micro-CT image results. The main difference is because microscopic images only capture a single layer of 3D printed parts for processing, which might not hold true for the whole stack of layers; that is why Micro-CT scanned images are advantageous for internal feature measurements.

As seen in the Figure 3-10, a histogram of particle distribution is generated. The figure depicts the frequency of the particle size range. It is visible that copper particle diameter between

the range of 10-20 µm has the highest frequency, and after that high percentage of copper particle diameter in the range of 20-30 µm. Copper particle size distribution is significant because this particle acts as a correlation marker for the DVC process, which helps detect tiny movements in the loaded parts. The features should be small enough to capture small movements under loading conditions. For the resolution of 5.4 µm, the particles in the 10-30 µm range will be sufficient for markers to detect movements [28]. Above 100 µm diameter particles are less than 2% of total particles and are believed to be present because of coagulation of small particles after nozzle heating which cannot be resolved using the above image processing techniques and is out of scope for the current research.

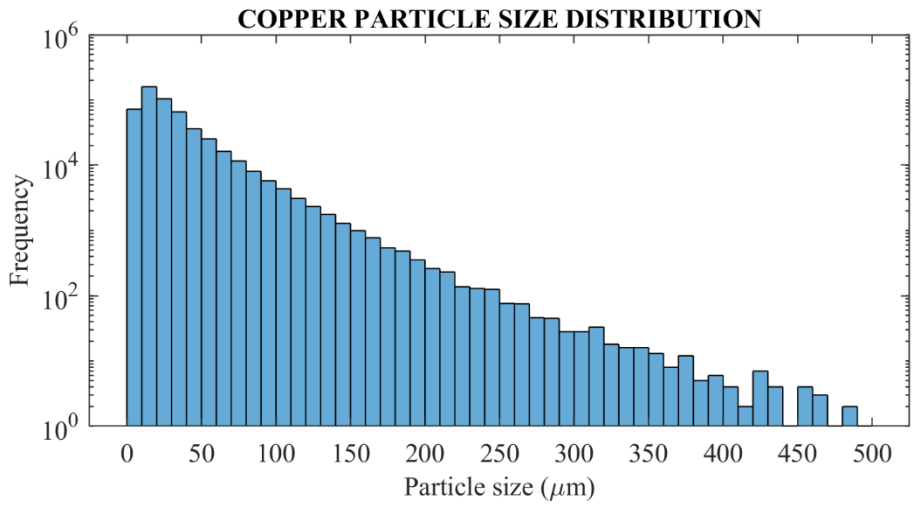

Figure 3-10: Copper particle distribution for 60% infill specimen.

3.3.2 Deformation and Strain Fields

The DVC results provide extensive information on the behaviour using the displacement and strain maps. Figure 3-11 shows the displacement along the axis of the applied force from 50N to 150N for each infill percentage specimen. As the infill percentage increases from 20 to 80 percent, the magnitude of displacement decreases. This can be explained by the fact that the

increase in infill percentage increases the strength, hence as strength increases displacement decreases. The displacement from the load cell side decreases towards the other the side of the specimen. As can be seen from the images the left side of the specimen has more displacement compared to the right side, which might be because of small misalignment of the sample in the testing stage. The point of this experiment is to prove the validity of DVC so strain results would be analyzed keeping the angular force in consideration.

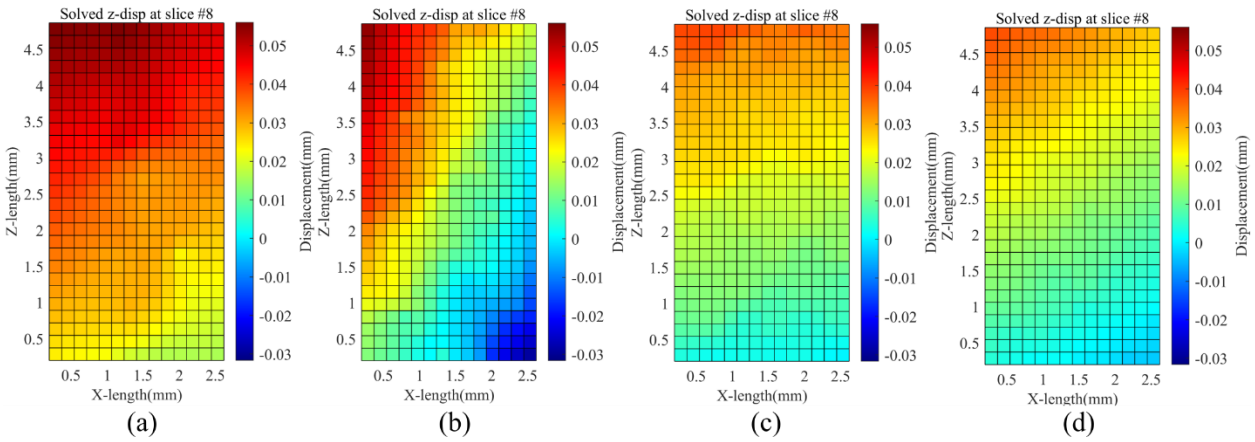

Figure 3-11: Z-Displacement field across X-Z plane for (a) 20% (b) 40% (c) 60% & (d) 80% infill specimen for 150 N of applied force.

Similar to displacement, Figure 3-12 shows the longitudinal strain (ε_{xx}) along the XZ plane for different infill percentages. The strain is negative across all the infill percentages from 20% to 80% apart from some part along the raster having a positive strain which might be because of uneven force distribution along the axis during tensile setup. The ε_{xx} strain decreases with an increase in infill percentage because of the additional material in the cross-section. A uniform negative strain can be seen along the shell region of the specimens. The negative strain implies that the shell is contracting along the x-axis due to extension along the z-axis which completely follows the Poisson's ratio effect.

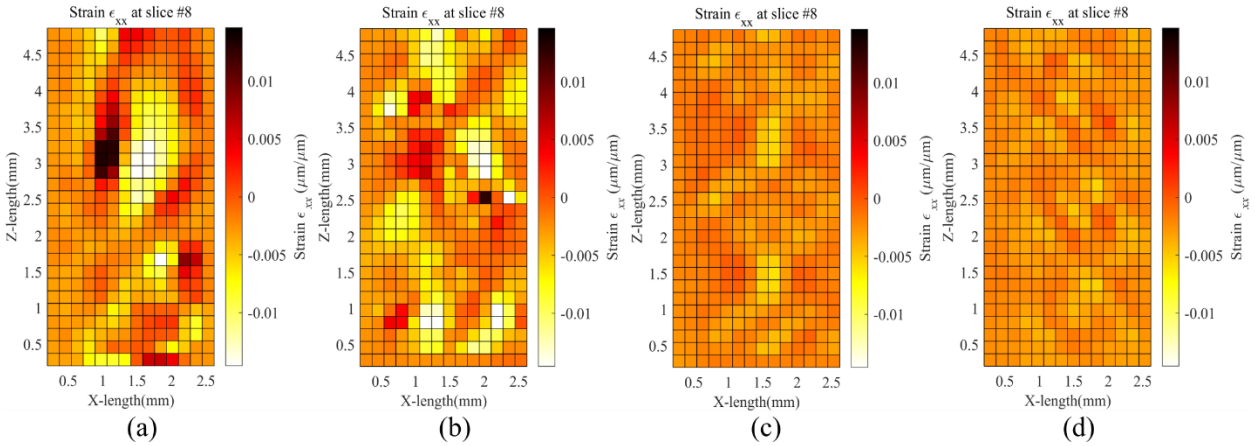

Figure 3-12: Volumetric Strain ε_{xx} across XZ plane for (a) 20 % (b) 40% (c) 60% & (d) 80% infill.

Figure 3-13 below shows the volumetric strain ε_{yy} along the X-Z plane. It has the same behaviour as ε_{xx} strain. The strain values are negative along the X-Z plane for all infill percentage with some positive strain values along the raster for similar reasons as mentioned above. Also, the strain decreases with increasing infill percentage. The negative strain values indicate that the sample is contracting along the y-axis. There is also high negative strain across the borders which indicates stress zones. It makes sense as the stress zone has a discontinuity because of raster connecting with the side walls. Timpano *et al.* in their study found ε_{xx} and ε_{yy} strain values to be negative, indicating the shrinking of the sample due to extension along the z-axis [23].

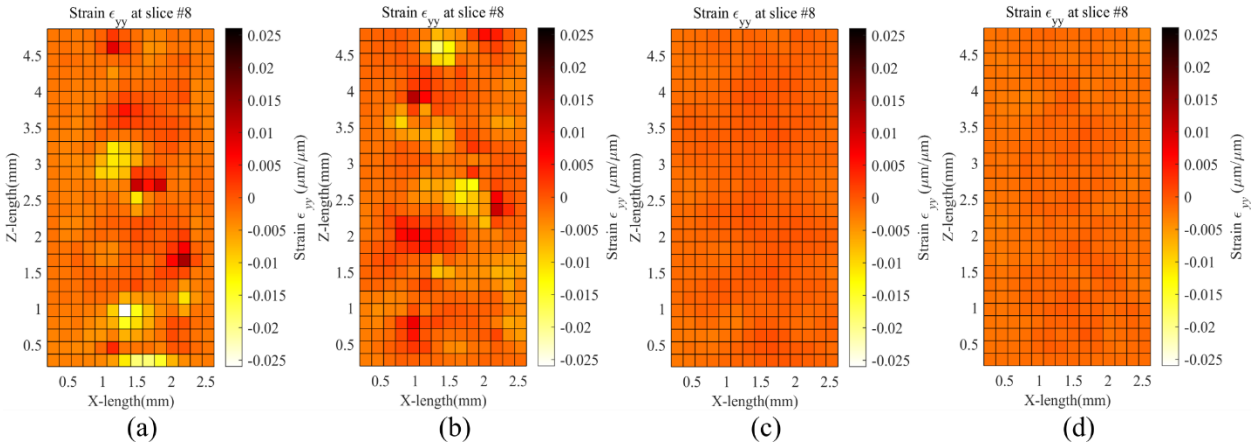

Figure 3-13: Volumetric Strain ε_{yy} across XZ plane for (a) 20 % (b) 40% (c) 60% & (d) 80% infill.

Figure 3-14 compares the Micro-CT image with the strain map and explains how infill distribution affects the resulting strain. Figure 3-14(i) shows the Micro-CT images obtained for the 20, 40, 60, and 80 infill samples. Figure 3-14(ii) shows the ε_{zz} across the different infill percentages i.e. the direction of strain. As the infill percentage increases from 20 to 80, a decrease in strain is observed since there is more material to reinforce the object. It also shows the region of high internal strain. The high strains forms along +45/-45 bands which correspond with the raster orientation. As can be seen from the figure, the strain bands are smoother as the infill percentage increases which might be because as the infill percentage decreases, the raster might be less precise for the dogbone structure. Also, there may be gaps or discontinuity along the raster bands as the infill percentage decreases. The high strains are also visible at the junction of the raster with the shell of the structure. The cracks initiation can also be detected with the strain map which under the current loading condition is not possible. These maps can be generated for multiple slices across the thickness of the specimen and can help capture strain for anisotropy of the FFF specimen. Figure 3-14(iii) shows the strain distribution of ε_{zz} across the Z-length marked by dotted lines in Figure 3-14(i). The peak strain has an almost periodic behaviour for each infill

percentage, the peak strain is associated with the raster band and lower strain almost tends to zero are the gaps between the raster bands. Since 20% infill would have significantly less raster bands as compared to 80%, the latter has more peaks. The peak strain for 20% infill is around 0.038 and for the 80% is around 0.012 which is a decrease of 316.6%. Timpano *et al.* in their study for 100% infill copper filled PLA sample, found similar +45/-45 bands along the raster orientation but predominantly +45 strain bands for ε_{zz} strain [23]. They also had similar cyclic strain peaks across the sample length, but the loading condition was different. They used 100N preload with step loading of 150N and 200N. Wang *et al.* built the specimen using stereolithography and performed a compression test [22]. This work showed the volumetric deformation and strain fields developed on a porous structure which has unit cell as hourglass-shaped, which would not be possible using DIC. Hourglass shape is two trapezoid prism with the smaller face of both side connected to each other. They found high tensile strain zone at the top/bottom edge of the hourglass and high compressive and shear strain zones on the side walls. Further, identifying damage forms for the structure. This shows how DVC can be used to map displacement and strain for anisotropic structures like FFF.

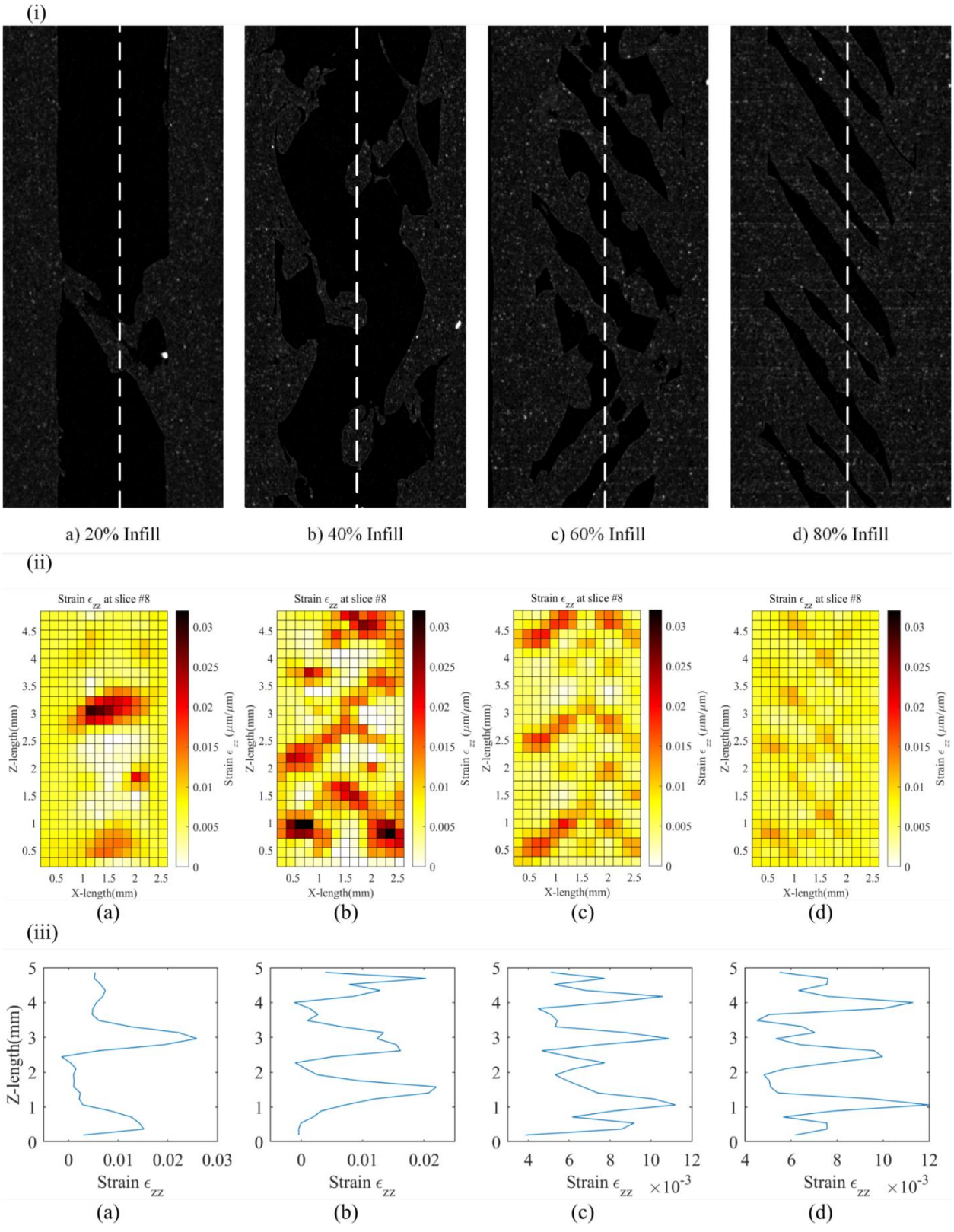
(i)
a) 20% Infill
b) 40% Infill
c) 60% Infill
d) 80% Infill
(ii)
Strain ϵ_{zz} at slice #8
Z-length(mm)
X-length(mm)
Strain ϵ_{zz} ($\mu m/\mu m$)
(a)
(b)
(c)
(d)
(iii)
Z-length(mm)
Strain ϵ_{zz}
Strain ϵ_{zz} $\times 10^{-3}$
(a)
(b)
(c)
(d)

Figure 3-14: (i) X-Z plane view of reconstructed 150N MicroCT data (ii) Volumetric Strain ε_{zz} across XZ plane (iii) Strain ε_{zz} across the Z-length for (a)20% infill (b) 40% infill (c) 60% infill (d) 80% infill.

The Table 3-4 provides the average strain and its standard deviation for 20, 40, 60 and 80 % infill specimen calculated using Microsoft Excel. The strain values generated from the ALDVC software over the Volume of Interest (VOI) was imported into Microsoft Excel. The VOI of the sample is 2.9 mm x 2.4 mm x 5.1 mm. The average strain and standard deviation in-built formula is used to calculate the average strain over the VOI. The average strain of 20% infill is found to be lower than 40% infill which might be due to high empty space with zero strain value in VOI which reduces the average strain. For 60% and 80% infill the average strain is almost same, but the standard deviation for 60% is high which indicates the peak strain for 60% is greater than 80%.

Table 3-4: Average strain value across the VOI region.

Infill percentage	Average Strain
20	0.0072 ± 0.0034
40	0.0086 ± 0.0057
60	0.0071 ± 0.0030
80	0.0072 ± 0.0013

The above results are only based for different infill percentages, which can also be used to understand how much infill percentage would be efficient for the loading condition as well as cost savings. Also, the results can be used to understand the effect of different print parameters volumetrically like the effect of layer thickness, shell thickness as well as temperature. This would

also help in understanding the internal behavior of complex 3D printed structure which is not possible with the DIC measurement technique. The results of the DVC is compared with the analytical model in the Appendix A.

Gonabadi *et al.* studied the effect of process parameters like infill pattern and infill density for the PLA samples using DIC [18]. The results showed full-field surface strain fields, however meaningful data could not be extracted from the strain maps. The strain distribution showed some strain localizations which is not correlated to the micromechanical properties of each process parameters. Similarly, Saleh *et al.* used DIC in the study for mechanical characterization of 3D printed rigid and flexible continuous wire polymer composites [29]. A full field internal strain field would have given more comprehensive analysis of the sample characteristics as opposed to a full field surface strain. Also, the Micro-CT model of the sample could be used to find the volume fraction of the constituents with better accuracy as compared to optical microscopy.

3.4 Conclusion

Tensile tests were conducted on 20, 40, 60 and 80 infill percentage FFF copper filled PLA specimen while the samples were positioned within a Micro-CT scanner. The specimen was manufactured according to the modified ASTM D638-14 type V. The specimen was scanned in Micro-CT under a preload of 50N and step load of 150N. The data was further processed and analysed to find porosity as well as copper particle distribution in the sample. The ALDVC software performed DVC analysis on 20, 40, 60, 80 infill percentage samples to measure the internal displacement and strain fields. This work established that as the infill percentage decreases displacement increases due to less materials. For the volumetric strain ε_{zz}, a high strain pattern was observed along the +45/-45 raster orientation. Thus, it can be used for understanding the

internal complex behaviour of FFF specimen. Furthermore, the data can be used to validate the finite element analysis as well as analytical models for FFF specimen.

3.5 References

[1] S. Singh, G. Singh, C. Prakash, and S. Ramakrishna, "Current status and future directions of fused filament fabrication," *Journal of Manufacturing Processes*, vol. 55. Elsevier Ltd, pp. 288–306, Jul. 01, 2020, doi: 10.1016/j.jmapro.2020.04.049.

[2] L. Jyothish Kumar and C. G. Krishnadas Nair, "Current trends of additive manufacturing in the aerospace industry," in *Advances in 3D Printing and Additive Manufacturing Technologies*, Springer Singapore, 2016, pp. 39–54.

[3] P. Wu, J. Wang, and X. Wang, "A critical review of the use of 3-D printing in the construction industry," *Automation in Construction*, vol. 68. Elsevier B.V., pp. 21–31, Aug. 01, 2016, doi: 10.1016/j.autcon.2016.04.005.

[4] J. S. Chohan and R. Singh, "Enhancing dimensional accuracy of FDM based biomedical implant replicas by statistically controlled vapor smoothing process," *Prog. Addit. Manuf. 2016 11*, vol. 1, no. 1, pp. 105–113, Apr. 2016, doi: 10.1007/S40964-016-0009-4.

[5] I. El-Katatny, S. H. Masood, and Y. S. Morsi, "Error analysis of FDM fabricated medical replicas," doi: 10.1108/13552541011011695.

[6] D. Wu, A. Spanou, A. Diez-Escudero, and C. Persson, "3D-printed PLA/HA composite structures as synthetic trabecular bone: A feasibility study using fused deposition modeling," *J. Mech. Behav. Biomed. Mater.*, vol. 103, p. 103608, Mar. 2020, doi: 10.1016/J.JMBBM.2019.103608.

[7] G. W. Melenka, B. K. O. Cheung, J. S. Schofield, M. R. Dawson, and J. P. Carey, "Evaluation and prediction of the tensile properties of continuous fiber-reinforced 3D printed structures," *Compos. Struct.*, vol. 153, pp. 866–875, 2016, doi: 10.1016/j.compstruct.2016.07.018.

[8] H. He and K. Molnár, "Fabrication of 3D printed nanocomposites with electrospun nanofiber interleaves," *Addit. Manuf.*, vol. 46, p. 102030, Oct. 2021, doi: 10.1016/J.ADDMA.2021.102030.

[9] M. Mohammadizadeh and I. Fidan, "Tensile Performance of 3D-Printed Continuous Fiber-Reinforced Nylon Composites," *J. Manuf. Mater. Process. 2021, Vol. 5, Page 68*, vol. 5, no. 3, p. 68, Jun. 2021, doi: 10.3390/JMMP5030068.

[10] L. Vásárhelyi, Z. Kónya, Kukovecz, and R. Vajtai, "Microcomputed tomography–based characterization of advanced materials: a review," *Materials Today Advances*, vol. 8. Elsevier Ltd, p. 100084, Dec. 01, 2020, doi: 10.1016/j.mtadv.2020.100084.

[11] S. K. Boyd, "Micro-computed tomography," *Adv. Imaging Biol. Med. Technol. Softw. Environ. Appl.*, pp. 3–25, 2009, doi: 10.1007/978-3-540-68993-5_1/COVER.

[12] S. Sommacal, A. Matschinski, K. Drechsler, and P. Compston, "Characterisation of void and fiber distribution in 3D printed carbon-fiber/PEEK using X-ray computed tomography," *Compos. Part A Appl. Sci. Manuf.*, vol. 149, p. 106487, Oct. 2021, doi: 10.1016/J.COMPOSITESA.2021.106487.

[13] S. Yu, H. Bale, S. Park, J. Y. Hwang, and S. H. Hong, "Anisotropic microstructure dependent mechanical behavior of 3D-printed basalt fiber-reinforced thermoplastic composites," *Compos. Part B Eng.*, vol. 224, p. 109184, Nov. 2021, doi:

10.1016/J.COMPOSITESB.2021.109184.

[14] L. Wang, W. M. Gramlich, and D. J. Gardner, “Improving the impact strength of Poly(lactic acid) (PLA) in fused layer modeling (FLM),” *Polymer (Guildf).*, vol. 114, pp. 242–248, Apr. 2017, doi: 10.1016/J.POLYMER.2017.03.011.

[15] J. Torres, J. Cotelo, J. Karl, and A. P. Gordon, “Mechanical Property Optimization of FDM PLA in Shear with Multiple Objectives,” *JOM 2015 675*, vol. 67, no. 5, pp. 1183–1193, Mar. 2015, doi: 10.1007/S11837-015-1367-Y.

[16] A. Sutradhar, J. Park, D. Carrau, and M. J. Miller, “Experimental validation of 3D printed patient-specific implants using digital image correlation and finite element analysis,” *Comput. Biol. Med.*, vol. 52, pp. 8–17, Sep. 2014, doi: 10.1016/j.compbiomed.2014.06.002.

[17] R. J. Zaldivar, D. B. Witkin, T. McLouth, D. N. Patel, K. Schmitt, and J. P. Nokes, “Influence of processing and orientation print effects on the mechanical and thermal behavior of 3D-Printed ULTEM® 9085 Material,” *Addit. Manuf.*, vol. 13, pp. 71–80, Jan. 2017, doi: 10.1016/J.ADDMA.2016.11.007.

[18] H. Gonabadi, A. Yadav, and S. J. Bull, “The effect of processing parameters on the mechanical characteristics of PLA produced by a 3D FFF printer,” *Int. J. Adv. Manuf. Technol. 2020 1113*, vol. 111, no. 3, pp. 695–709, Oct. 2020, doi: 10.1007/S00170-020-06138-4.

[19] A. Buljac *et al.*, “Digital Volume Correlation: Review of Progress and Challenges,” *Exp. Mech.*, vol. 58, no. 5, pp. 661–708, Jun. 2018, doi: 10.1007/s11340-018-0390-7.

[20] B. Pan and B. Wang, “Some recent advances in digital volume correlation,” *Opt. Lasers*

Eng., vol. 135, p. 106189, Dec. 2020, doi: 10.1016/J.OPTLASENG.2020.106189.

[21] B. K. Bay, T. S. Smith, D. P. Fyhrie, and M. Saad, "Digital volume correlation: Three-dimensional strain mapping using X-ray tomography," *Exp. Mech. 1999 393*, vol. 39, no. 3, pp. 217–226, 1999, doi: 10.1007/BF02323555.

[22] B. Wang, L. Sun, and B. Pan, "Mapping internal deformation fields in 3D printed porous structure with digital volume correlation," *Polym. Test.*, vol. 78, Sep. 2019, doi: 10.1016/j.polymertesting.2019.105945.

[23] C. S. Timpano and G. W. Melenka, "Digital volume correlation analysis of polylactic acid based fused filament fabrication printed composites:," *https://doi.org/10.1177/00219983211020500*, May 2021, doi: 10.1177/00219983211020500.

[24] J. Yang, L. Hazlett, A. K. Landauer, and C. Franck, "Augmented Lagrangian Digital Volume Correlation (ALDVC)," *Exp. Mech.*, vol. 60, no. 9, pp. 1205–1223, Nov. 2020, doi: 10.1007/s11340-020-00607-3.

[25] B. Pan, "Recent Progress in Digital Image Correlation," *Exp. Mech.*, vol. 51, no. 7, pp. 1223–1235, Sep. 2011, doi: 10.1007/S11340-010-9418-3/FIGURES/6.

[26] I. Buj-Corral, A. Bagheri, and M. Sivatte-Adroer, "Effect of Printing Parameters on Dimensional Error, Surface Roughness and Porosity of FFF Printed Parts with Grid Structure," *Polym. 2021, Vol. 13, Page 1213*, vol. 13, no. 8, p. 1213, Apr. 2021, doi: 10.3390/POLYM13081213.

[27] S. Guessasma, S. Belhabib, and H. Nouri, "Effect of printing temperature on microstructure,

thermal behavior and tensile properties of 3D printed nylon using fused deposition modeling," *J. Appl. Polym. Sci.*, vol. 138, no. 14, p. 50162, Apr. 2021, doi: 10.1002/APP.50162.

[28] C. S. Timpano and G. W. Melenka, "Artificial seeding for micro-computed tomography image contrast enhancement for digital volume correlation," *Compos. Part B Eng.*, vol. 215, p. 108809, Jun. 2021, doi: 10.1016/J.COMPOSITESB.2021.108809.

[29] M. A. Saleh, R. Kempers, and G. W. Melenka, "A comparative study on the electromechanical properties of 3D-Printed rigid and flexible continuous wire polymer composites for structural health monitoring," *Sensors Actuators A Phys.*, vol. 328, p. 112764, Sep. 2021, doi: 10.1016/J.SNA.2021.112764.

Chapter 4 Investigation of Carbon-Aramid Hybrid Braided Composites Using DVC

4.1 Introduction

Composite materials are being used widely in many applications such as robotics, aviation, biomechanics, and construction. Braided composites are a subset of textile composite materials, that feature long continuous fibre in an interwoven structure [1]. Braided composites are commonly used for pressure vessels, columns, bicycle and shafts [2]–[4]. Braids can be categorized into two main types: 2D braids and 3D braids. The more common 2D braids feature fibres interlaced together along the longitudinal axis in one plane. 3D braids are preforms in which yarn runs in all the directions of the braids. This study will focus on only 2D braids. Due yarn undulations caused by the braiding process, braided composites are tougher and less stiff than the traditional laminates [1], [5]. The braids are further categorized based on braiding pattern, the three most common braiding pattern are: diamond (1/1), regular (2/2) and Hercules (3/3) [6]. Diamond are braids in which one yarn overlap one yarn; the regular are braids in which one yarn overlaps two yarns and is the most highly used among the three and the last one is Hercules which are braids in which one yarn overlaps three yarns [7]. A maypole braider is used to produce 2D braids with the aforementioned patterns [6], [8]. Materials generally used for braids are glass, carbon or aramid fibres. Carbon fibres generally have a high tensile modulus but low damage tolerance and low elongation. Due to which, researchers are incorporating other materials to compensate some of the properties of carbon fibres. Carbon-aramid hybrid composite has been a good alternative as aramid increases the damage tolerance and provides higher elongation[9]. Since the structure of braided composite is complex, there is a need for non-destructive techniques to understand the internal

microstructure. One technique best suited to examine the complex microstructure of braided composites is micro-CT.

Micro-CT is a non-destructive method that uses X-rays to image the internal microstructure of an object [10]. The X-ray beams are ejected through the X-ray tube towards the sample. X-rays are attenuated based on the density of the material. The X-rays are collected by a detector which generates the 2D projections of the sample. The sample is rotated 180 or 360 degrees to acquire sufficient projections from different angles to resolve the 3D geometry. After the projections are collected, an image reconstruction process is used to give a stack of the cross-sectional image of the sample. The Micro-CT process has been used to characterize braided composites, quantify damage in braided tubes and identify cracks. For example, Melenka *et al.* in their study used Micro-CT to identify and measure braid yarn fibres of regular 2x2 cellulose fibres embedded in a bio-based resin for two samples with 45° and 55° braid angles [11]. They also found other fibre properties such as orientation angles, fibre diameter, etc using micro-CT data. Gu *et al.* used micro-CT to construct the damage volume and quantitatively measure the torsional damage for a braided carbon/epoxy tube [12]. Similarly, Shi *et al.* for their low-velocity impact experiment on an inter-ply biaxial-uniaxial braided tube employed Micro-CT to evaluate the crack locations as well as to characterize the damage mechanism [13]. Presently, limited research has been done in terms of hybrid braids or hybrid laminates using Micro-CT. Yin *et al*. investigated carbon-aramid hybrid woven composites using micro-CT for crack initiation and failure mechanisms [14]. The authors were able to find different mechanical behaviour based on which of the hybrid fibre among carbon and aramid was in the loading direction. Currently, few studies have examined the internal strain fields of braided composites, in particular, hybrid-braided composites.

The manufacturing of a laminated or tube braid consists of layers of braids stacked together with matrix material, traditional measuring techniques like strain gauges do not provide enough information for braided composites [15]. Some of typical failures like delamination, fibre breakage can happen at any point on the specimen which cannot be detected using strain gauge which is why a full-field deformation and strain is required. Digital Image Correlation (DIC) is a contact-free optical measurement technique to measure a specimen's outer surface deformation and strain fields [16]. A speckle pattern is applied to the specimen and optical cameras are used to track marker displacement. Zheng *et al*. investigated the behaviour of carbon-aramid 3D braided composites under axial tensile loading using DIC [17]. Two hybrid configuration for 3D braids were studied, one in which carbon fibre was axial fibre and the other one had Aramid fibre as axial fibre. The study found that the hybrid 3D5d braided composites with carbon fibre as axial yarns showed the highest tensile strength and modulus. Similarly, aramid fibre as axial yarn showed maximum ultimate strength and Poisson's ratio. Cerbu *et al.* used DIC for hybrid carbon-aramid composites under tensile and bending loading to obtain the mechanical characteristics for numerical simulation as well as analytical modelling [9]. Leung *et al.* studied a tubular braided composite using a stereo DIC technique and an optical microscope and measured the change in braid radius and braid angle during tension [18]. Unit cells in 3 regions of the tube surface were studied. This is important to capture failures in the braids which cannot be measured accurately with the conventional techniques like strain gauge. Armanfard *et al*. used 3D-DIC to evaluate the behaviour of carbon fibre, glass fibre and aramid braided composite tubes under combined tension-torsion loading [19]. 3D-DIC uses two cameras to capture the in the plane and out of the plane strain which is not possible with 2D-DIC. It was found that with increasing torsional load under combined loading, buckling initiates at the maximum shear stress point in the braid. In all the

previously mentioned studies, the external surface of the braid was examined. With braided composites the behaviour inside the layers can be different from the surface behaviour. Defects such as delamination, crack initiation could not be studied when using a surface measurement technique like 3D-DIC. Therefore, alternative measurement techniques are required which can be used to understand the internal deformation and strain behaviour of the specimen.

Digital Volume Correlation (DVC) is an advanced measurement technique to measure the 3D deformation and strain of an object; DVC is similar to DIC but in a 3D space allowing for the full 3D strain tensor to be obtained for a material. DVC can use volumetric data from X-ray CT or magnetic resonance imaging (MRI) data to measure deformation and strain [20], [21]. It was first developed by Bay *et al.* to examine internal strain of trabecular bone placed under compressed loading [22]. Initially, DVC was used for biomechanical applications and later extended to solid mechanics [23]. Holmes *et al.* used DIC as well DVC for mechanical characterization of woven fabric [24]. The results showed that DVC can be used to identify delamination as well as onset of cracking based on out-of-plane strain and can be further used to develop a better analytical model. Mehdikhani *et al.* investigated the micro as well as meso damage analysis of carbon fibre composites using DVC [25]. They used the texture contrast of fibres as the speckle pattern for tracking displacement. Liu *et al.* studied the failure of 3D 4-step braided SiC/SiC composites under flexural loading using DIC as well DVC [26]. The author was able to observe different failure modes such as matrix cracking, fibre breakage and inter- & intra- bundle debonding. Currently, all research has focused on a single braided materials and hybrid braids have yet to be investigated with the DVC method.

In order for accurate measurements to be obtained with the DVC process sufficient contrast is required to obtain correlation between datasets. One way to improve image contrast is to include

markers or particles within a material. With DVC, few authors have included tracking particles within samples to improve the correlation while the majority of studies relied on natural features of the material to act as trackers. Timpano *et al.* used different material particles of diameter ranging from 10 µm to 100 µm to investigate the effect on DVC analysis for an epoxy sample [27]. In this work, 25 µm copper particles were found to be most suitable for greatest accuracy of DVC analysis. Croom *et al.* used speckle pattern for syntactic foam specimen by suspending hollow glass microballoons (GMB) in elastomer resin matrix [28]. The size of GMB's were 30 to 95 um for 10-90% distribution. Gonzalez *et al.* in their study used two Polydimethylsiloxane (PDMS) samples, one with silica glass beads and the other with zirconia marker particle [29]. They studied the effect of different particles on the DVC analysis. There has been no direct comparison between a natural contrast and seeded particles for best the correlation results. Therefore, the study will compare the results of natural contrast with seeded particles. The study will follow Timpano *et al.* work which uses 25 µm copper seeded particles as these worked best for correlation.

The paper aims to study the Carbon-Aramid hybrid braided composite under tension using the DVC measurement technique. The Carbon-Aramid hybrid braided composites were impregnated within a PDMS matrix. Additionally, this work will compare the DVC results for a copper particle vs non-copper added to the hybrid braid samples to enhance image contrast. The specimen is loaded in tension with a loading of 25N with step loading of 50N, 75N and 100N under Micro-CT to collect cross-sectional images. The images are processed further using an open-source DVC software package, ALDVC [30], to generate full-field volumetric deformation and strain fields. This will help in understanding of internal behaviour of hybrid braided composite as well as importance of tracking particle for accurate measurement results. The results will be further compared with an analytical model and further validate finite element model for braided specimen.

4.2 Methodology

4.2.1 Manufacturing

The two samples were prepared based on the geometry as shown in Figure 4-1. In this image, the sample dimensions of 30mm x 15 mm are shown. End tabs were also bonded to the test specimen as shown in Figure 4-1 using epoxy. The end tabs were made up of 1.58 mm thickness phenolic sheet. The holes were made using a drill press with the drill bit diameter of 2.8 mm. End tabs were included to prevent tear-out of the braided composite sample during testing.

One sample included tracking particles while the other sample did not include tracking particles so that the effect of including tracking particles can be examined for the DVC analysis of carbon-aramid hybrid braided composites. The reinforcement phase is a red Carbon-aramid Hybrid braided sleeve Biaxial ±45° with a 1” diameter (Rockwest companies, San Diego, CA). The matrix phase for the sample is Polydimethylsiloxane ((PDMS), SYLGARD 184 silicone Elastomer, DOW, Michigan). The PDMS comes as a two-part base and cure, which are mixed 10:1 by weight ratio. PDMS was used as this is a flexible reinforcement phase and so that displacement and strain can be detected within the micro-CT machine. In the first sample, copper particles (Sigma Aldrich, United States) ranging 10-25 µm in diameter were mixed with the PDMS matrix with a weight percentage of 5% using the procedure developed by Timpano *et al.* [27]. The copper seeded particles are a higher density material as compared to epoxy which could be easily seen in Micro-CT and are used as trackers for calculating the internal displacement and strain [27]. The second sample was manufactured without the addition of seeding particles.

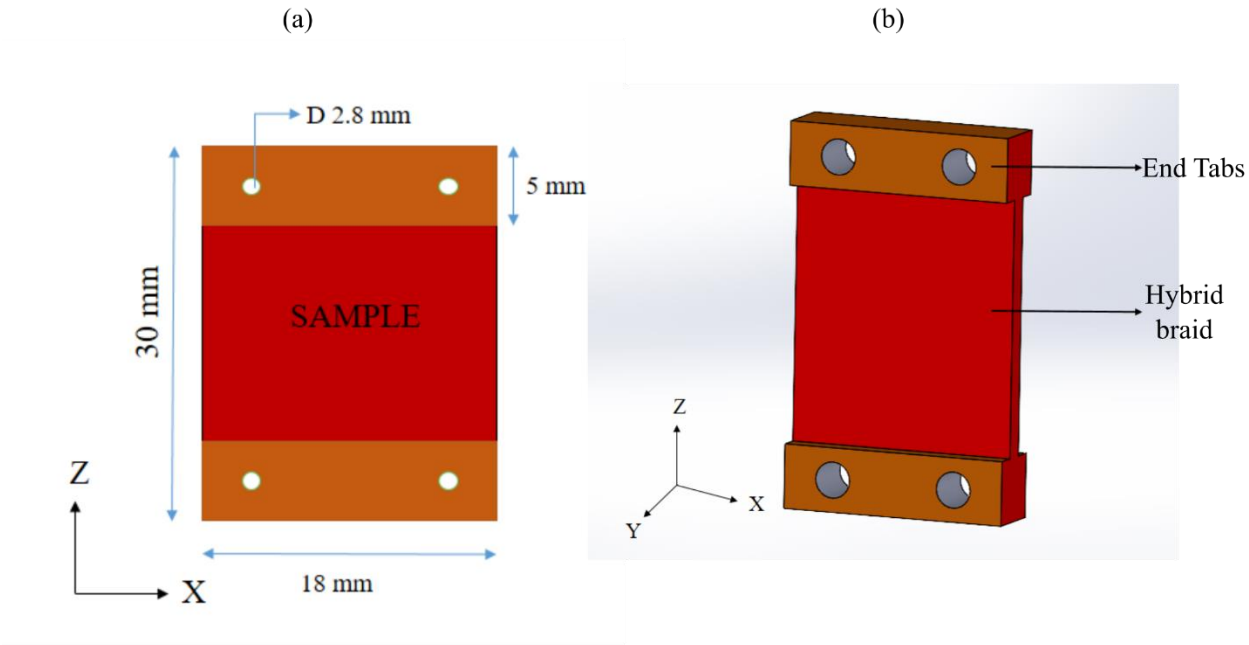

Figure 4-1: (a) 2D sample where the blue portion is Carbon-aramid braids, orange portion is end tabs, the holes are used to fix the specimen in the MTS using screws. (b) 3D view of the sample.

The sample is manufactured using a hand lay-up vacuum bagging technique as shown in Figure 4-2. This method uses atmospheric pressure to apply force on the laminate until the epoxy cures. The process involves applying a release film (LOCTITE® FREKOTE 770-NC™, Henkel Canada Corporation, Mississauga, Ontario) so that the samples do not adhere with the glass plate after curing. Then the PDMS is applied over the braids, with or without copper particles. A layer of peel ply (Airtech Bleederlease, Composites Canada, Canada) is applied which provides an easy release between the braids and the breather. Two layers of breather (Airtech Airweave, Composites Canada, Canada) are added over it which remove the excess resin. The vacuum bag is placed on top of all the layers to make an airtight seal. The vacuum hose is connected from the vacuum bag to the motor which creates a vacuum inside the bag and in turn creates a pressure of 101 KPa (1 atmosphere) over the braids. The vacuum bagging technique is applied for an hour and further

transferred to an oven (Oven Model 5851, NAPCO, USA) to accelerate the curing of the PDMS. The oven is pre-heated to 100 °C and the whole system is kept inside the oven for 30 minutes for full cure.

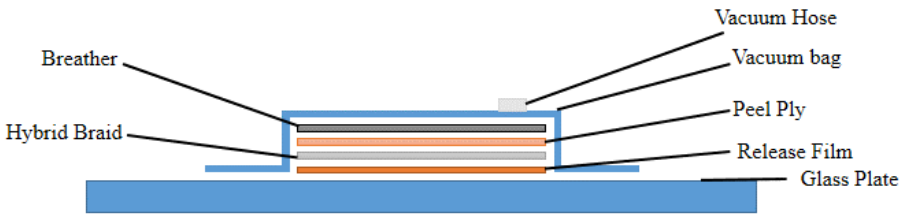

Figure 4-2: Vaccum Bagging Manufacturing for the hybrid braid sample

4.2.2 Micro-CT Scans

The braided samples were scanned using a desktop Micro-CT machine (Skyscan 1272 Micro-CT, Bruker Belgium). Mechanical testing of the samples was provided using the material testing stage (Tension and Compression stage, Bruker, 440N). For the acquisition of 3D images, first, the pixel size of the images is set as 8.6 µm with a resolution of 2452 x 2452 x 1471 pixels based on the specimen size and the expected deformation. The effective field of view is 21.09 mm x 21.09 mm x 12.65 mm. Next, the voltage setting of the system is set at 70KV and the current is set automatically based on the voltage setting. A filter of 1 mm Aluminum is applied which helps to remove the noise and the artifacts from the acquisition of images. Frame averaging of 5 with 2x2 binning was also selected in improve the signal to noise ratio of the images [27]. Table 4-1 summarizes the micro-CT parameters used for the samples.

Table 4-1: Micro-CT Scan Parameters.

Micro-CT Parameter	Setting
Source Voltage	70 kV
Source Current	1 mm
Resolution	2452 x 2452 x 1471 pixels
Pixel size	8.4 μm
Filter	1 mm Al
Binning	2 x 2
Frame Averaging	5
Rotation step	0.4°

Internal loading of the hybrid braid samples was provided using an integrated testing stage that applies load to samples within the Micro-CT machine as shown in Figure 4-3. The Material Testing Stage (MTS) consists of a load cell which measures the force applied to the test sample. The MTS also includes a linear actuator that can apply either tension or compression to the sample. The sample is loaded into the sample holder and further loaded into the chuck in MTS. Initially, a preload of 25N was applied to each sample. Following the initial preload load steps of 50N, 75N and 100 N were applied. A subsequent Micro-CT scan was performed at each loading step in a batch scanning mode for the software to take multiple loading scans of the sample. Between each loading condition, a delay of 180s was applied to ensure there are no errors caused by the MTS loading process before subsequent Micro-CT scans. A similar tensile loading procedure has been applied by Timpano & Melenka to evaluate the internal strain of fused filament fabricated dogbone samples [31].

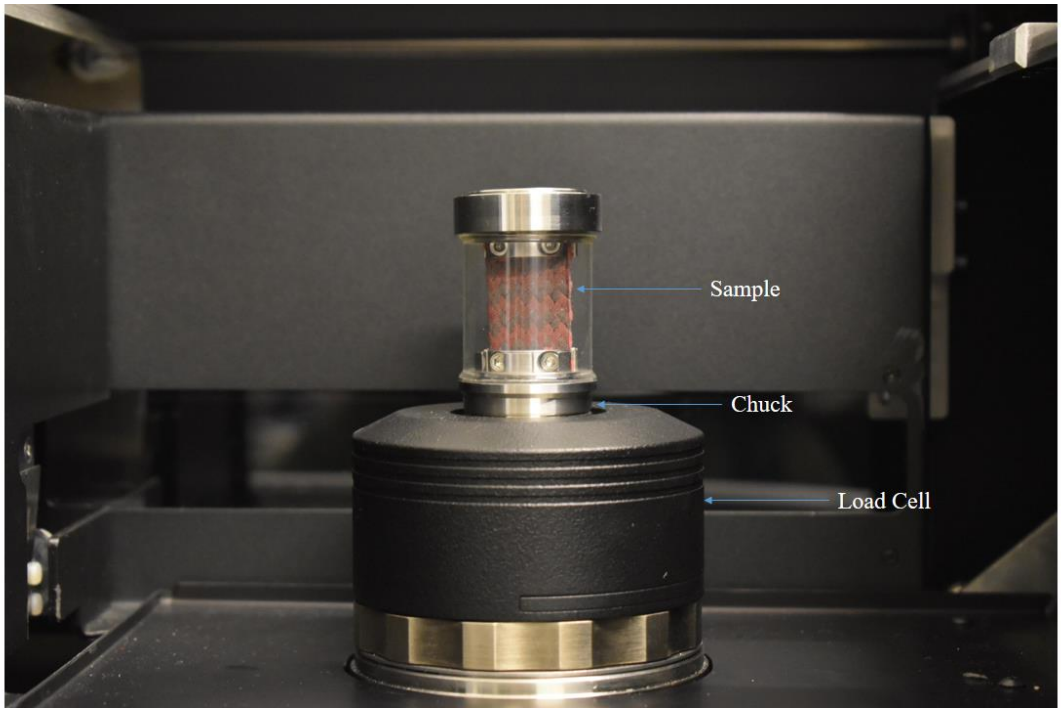

Figure 4-3: Setup View of Material Testing Stage inside Micro-CT. The sample holder holds the sample, chuck holds the sample holder & connects to the load cell and load cell is used to apply forces in tension or compression.

After the scans, reconstruction of Micro-CT data begins. Reconstruction software (Nrecon version 1.7.1.0, Bruker, Belgium) is used for processing and reconstruction of the acquired images. Various filters can be applied based on the noise to remove them. In this work, a ring artifact correction of 10 and beam hardening correction of 50% was used for the sample with copper particles while no beam hardening was required for the sample without copper particles as shown in Figure 4-4. Figure 4-4 (a) shows the braid sample with included copper particles and Figure 4-4(b) shows the braid sample where no copper particles were included. Smoothing or blurring can be used to reduce noise in the image. A Gaussian smoothing of value 5 was applied for sample without copper particles. Table 4-2 shows the different NRecon settings for copper specimen and non-copper specimen.

Table 4-2: NRecon Reconstruction Settings.

NRECON Parameters	With Copper	Without Copper
Ring artifact correction	10	10
Beam Hardening	50 %	0 %
Gaussian Smoothing	0	5

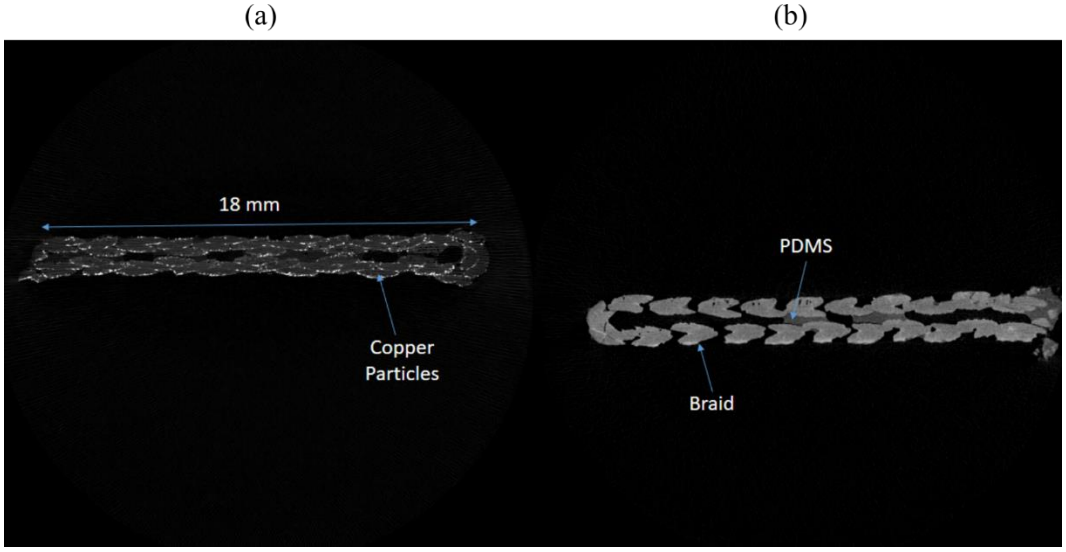

Figure 4-4: Micro-CT reconstructed image for (a) copper and (b) non-copper specimen. It shows the cross sectional view of the specimen with a clear distinction of braid, PDMS and metal particles.

4.2.3 Pre-Processing

Pre-processing of the copper filled Carbon-aramid hybrid braids shown in Figure 4-5(a) was done to find the copper particle size distribution. The distribution helps to understand the particles that will be used as tracker for DVC. Image processing software, CTAn (Version 1.16.9,

Bruker, Belgium), was used for all the image pre-processing. With the help of software, a median filter of radius 3 was applied to minimize the noise in the image. On histogram of an image as shown in Figure 4-5(c), 0 signifies that the X-ray beams did not hit any object while 255 signifies that 100% X-ray beams were absorbed or deflected. Since the density of copper particles are greater than the density of hybrid braid so it absorbs or deflects more X-ray beams, hence higher value on a histogram. Based on this, threshold of 99 was applied which produced copper particles in white as shown in Figure 4-5(b). Further using in-built 3D particle analyser tool, copper particle distribution was found.

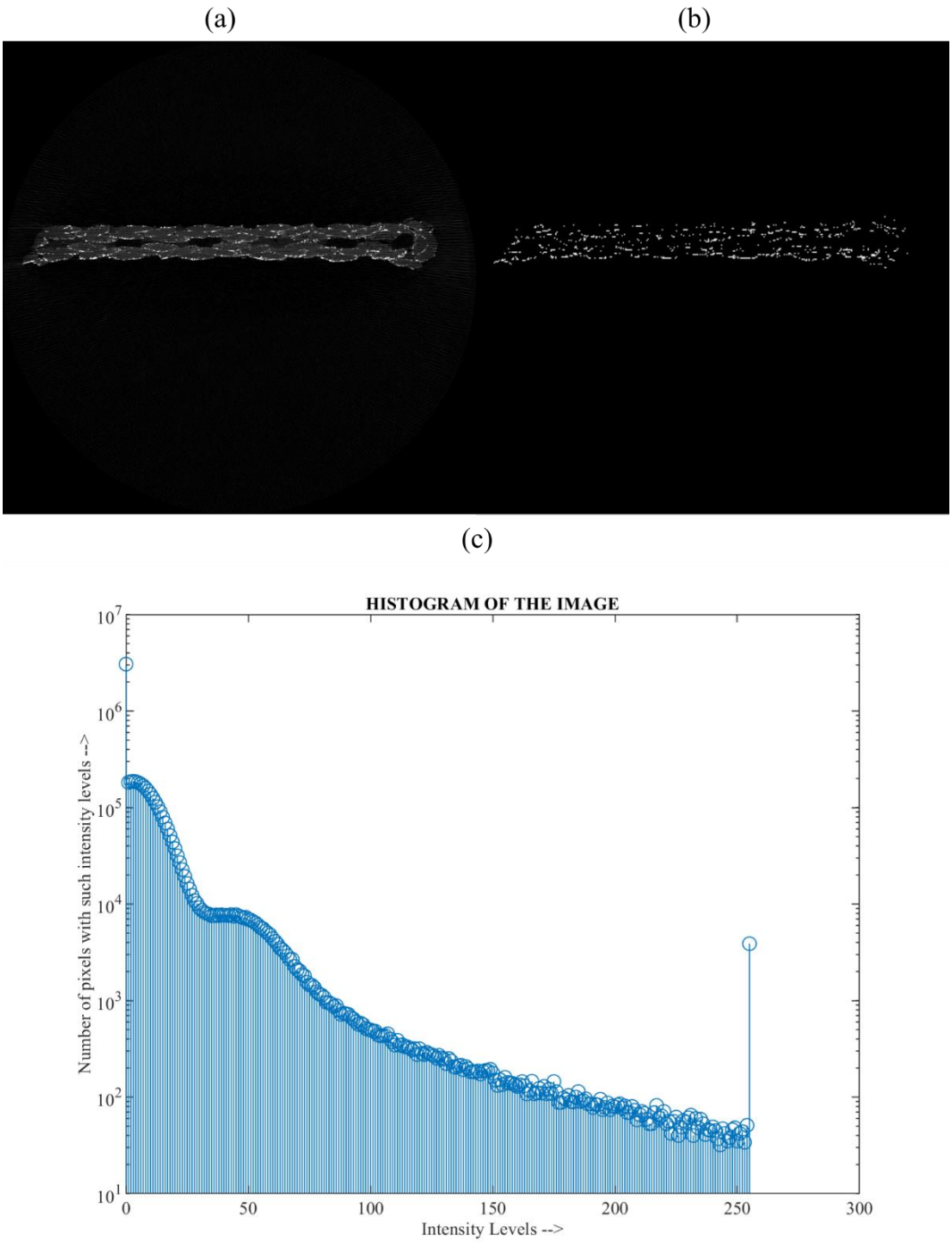

Figure 4-5: (a) Cross-Sectional Image of 25N loading copper specimen (b) Copper particles after thresholding (c) Histogram of Image.

4.2.4 Braid Angle Measurement

The angle of the braids is an important parameter which dictates the mechanical strength of the specimen. It can be measured through multiple ways; first is using the specimen image captured using camera and second is using the projections generated through Micro-CT. For the current study, the image of specimen captured with camera was used. ImageJ with an in-built tool was used to measure the braid angle of the specimen.

4.2.5 DVC Analysis of Carbon-Aramid Samples

An open-source MATLAB-based program (ALDVC 1.0) was used to perform DVC analysis of the hybrid braided composite samples as shown in Figure 4-6 [30]. The program compares the original and deformed images to find the 3D deformation and strain values of the specimen. A server computer (Precision T5600, Dell, Round Rock, Texas) with a RAM of 112 GB and two Intel Xeon CPU E5-2680 2701 Mhz 8 core processors has been used for DVC analysis.

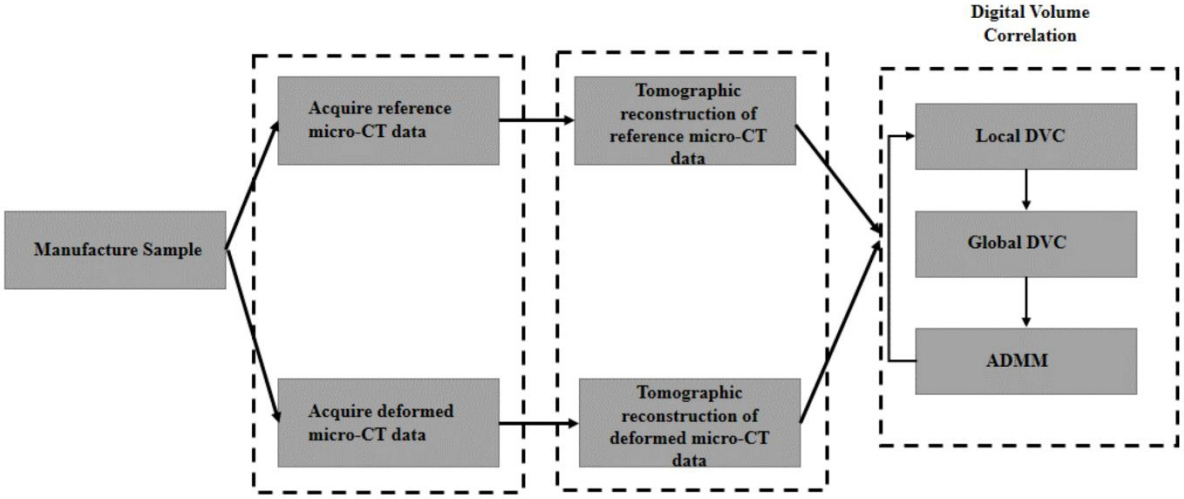

Figure 4-6: Schematic of digital volume correlation method.

Various parameters need to be defined to find volumetric deformation and strains. First is the subset size, a large subset of 128 cubic voxels is assumed based on the expected deformation and is iterated to a lower subset based on the best correlation. After the selection of subset size, different voxel spacing or step sizes are used to find the best correlation. Based on this, a final subset size of 64 cubic voxels and 16 (25%) voxel spacing was utilized as shown in Figure 4-7. The red squares is the subset size of 64 cubic voxels in a 2D image and the yellow squares shows the subset size with 25% voxel spacing between the subset. For initial guess estimation, zero normalized cross-correlation is used for local correlation since it is most suitable for small deformations, and the finite difference method is used for global correlation, which is the recommended method by the software [30]. The DVC analysis parameters used in this study are summarized in Table 4-3. For strain measurement, the finite difference method is used based on infinitesimal strain. Infinitesimal strain formulation was selected as the deformation of the solid structure is very small in comparison to body dimensions. The strain tensor for the infinitesimal is shown by Equation (4-1) where E is the strain tensor, u is the displacement and x is the direction. Equation (4-2) shows the final strain tensor matrix.

$$E_{ij} = \frac{1}{2}\left(\frac{\partial u_i}{\partial x_j} + \frac{\partial u_j}{\partial x_i}\right) \; i = 1,2,3; j = 1,2,3 \tag{4-1}$$

$$\varepsilon = \begin{bmatrix} E_{11} & E_{12} & E_{13} \\ E_{21} & E_{22} & E_{23} \\ E_{31} & E_{32} & E_{33} \end{bmatrix} \tag{4-2}$$

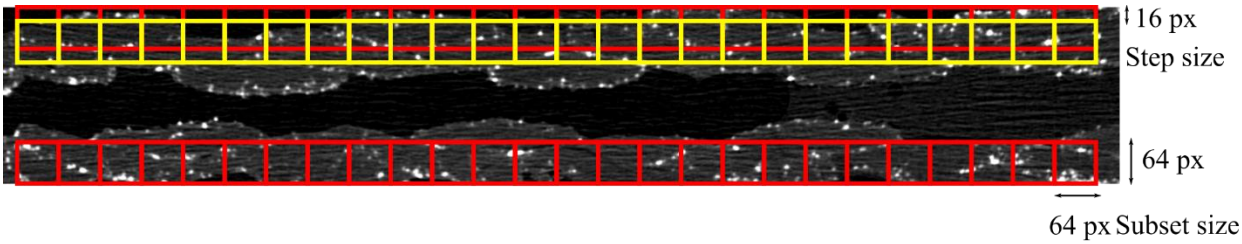

Figure 4-7: Subset size and step size reference in braided composite Micro-CT data for DVC.

Table 4-3: Digital volume correlation parameters.

Parameter	Values
Subset size	64 cubic voxels
Subset spacing	16 voxels
Initial Guess Estimation	Zero Normalized cross correlation
Strain Measurement	Infinitesimal strain

4.3 Results

4.3.1 Copper Particle Distribution

A histogram of copper particle distribution is generated as shown in Figure 4-8. As can be seen, approximately 41.29% of particles were found to have a diameter of 25.8 µm. 18% of particles were found to be in the range of 60-70 µm and 11% of particles were found in the range of 70-80 µm. The remaining 30% of particles are 80 µm and above in diameter. The copper particles used in this work have diameters that range from 10-25 µm. The particle distribution shown in Figure 4-8 is due to the coagulation of small copper particles which cannot be resolved with the image processing software used. The coagulation is high in the composite because the metal particles concentrate at the corners of the braid and within braid yarns which can be seen in

Figure 4-7. The copper particle size distribution is necessary to understand as they form the contrast markers for tracking displacement using DVC.

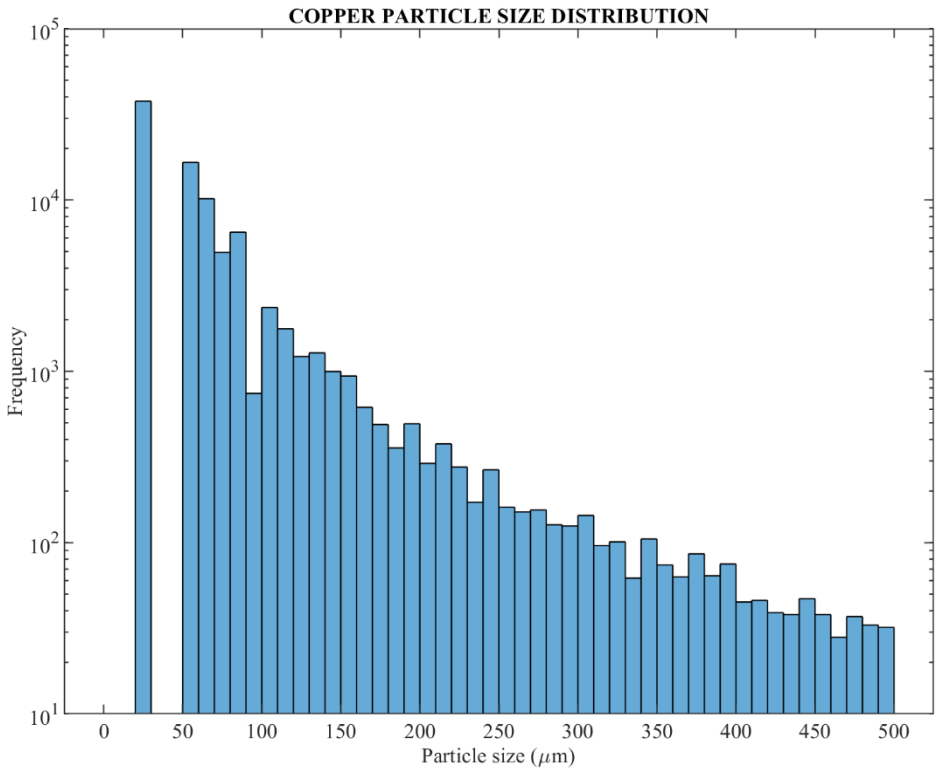

Figure 4-8: Copper Particle Size Distribution.

4.3.2 Copper vs Non-Copper Particle Specimen Results

Table 4-4 shows ε_{xx} and ε_{zz} average strain and standard deviation of the whole volume of interest for copper as well as non-copper samples. The values were extracted through ALDVC and the average strain were calculated in Microsoft Excel. ε_{xx} and ε_{zz} were examined for this particular sample since ε_{zz} represents strain in the longitudinal direction of the sample and ε_{xx} represents transverse strain. ε_{yy} represents the strain in the thickness direction of the sample. As can be seen from the table, the magnitude of average strain increases with increase in load for both ε_{xx} and ε_{zz} strain for copper as well as non-copper particle specimen. The average strain for ε_{xx} and ε_{zz} for

copper particles are almost in the same range of average strain for non-copper particles. However, the standard deviation for non-copper specimen is higher as compared to the copper particle sample. This could be because the natural texture of the Carbon Aramid specimen might provide sufficient contrast to act as natural trackers for DVC. In particular, for the cases where the expected displacement is small compared to specimen geometrical dimensions. As the correlation size decreases, the noise increases and correlation factor decreases. A smaller subset size might not capture enough natural details with non-copper specimen to give a good correlation in turn leading to higher standard deviation.

Table 4-4: Average and standard deviation strain values across the volume of interest.

	Copper Seeded Strain		Non-Copper Seeded Strain	
LOAD	STRAIN ε_{xx}	STRAIN ε_{zz}	STRAIN ε_{xx}	STRAIN ε_{zz}
50N	-0.0058 ± 0.0036	0.0016 ± 0.0012	-0.0069 ± 0.0125	0.0014 ± 0.0157
75N	-0.0136 ± 0.0080	0.0036 ± 0.0026	-0.0146 ± 0.0225	0.0033 ± 0.0251
100N	-0.0214 ± 0.0123	0.0055 ± 0.0043	-0.0235 ± 0.0278	0.0048 ± 0.0306

The Table 4-5 shows the bad subset percentage for copper and non-copper specimen using ALDVC for different loads. Bad subset refers subsets where no correlation can be obtained. This can be due to multiple reason, first if the specimen does not have enough features or natural

contrast to track displacement. The other reason might be because of IC-GN iteration convergence which is a minimization algorithm used in DIC and DVC to find best correlation. So, if the number of iterations reaches the maximum iterations set by the user, the subset fails to find any good correlation. Table 4-5 shows a stark difference of bad subset percentage for copper vs non-copper. Both samples had the same loading and manufacturing process but one sample included copper particles while the other did not. The 50N load has a 0% bad subset for copper particle specimen while non-copper has 52.66%. Furthermore as the load increases, the number of bad subset percentage increases. This data further supports how particle seeding improves the DVC results as compared to the non-seeding specimen. The natural texture of materials might not be good enough for an accurate result of the specimen examined in this work. The standard deviation of strain for non-copper particle specimen as shown in Table 4-4 comes to be high, can be associated with bad subset percentage. As the bad subset percentage increases, the correlation factor drops for the subset and becomes less accurate which leads to error and high standard deviation for strain maps. Timpano *et al.* found 1.8% error with 25µm copper particle for 64 cubic voxels subsets size [27]. The other particles with different size and material had higher error percentage but still under 15% error. As compared with non-copper specimen in our study, the error percentage starts over 50% while the highest error percentage was 13.52% for copper specimen with 100N loading. This shows the effectiveness of copper particles over natural contrast.

Table 4-5: Bad subset percentage for copper and non-copper specimen across multiple loadings.

Load	Copper	Non-Copper
50N	0 %	52.66 %
75N	12.79 %	60.24 %
100N	13.52 %	65.66 %

Figure 4-9(a) shows the slices used for displacement and strain maps for copper specimen. The Slice #2 and Slice #8 lies within the braid fibres while slice #6 is for the matrix portion of the structure. Similarly, Figure 4-9(b) shows the slices used for displacement and strain maps for non-copper specimen. The Slice #2 and Slice #8 lies within the braid fibres while slice #4 is for the matrix part of the structure. Detailed comparison of ε_{zz} strain maps for copper and non-copper specimen are shown in Figure 4-10-Figure 4-12. Figure 4-10 shows the cross-sectional CT image for copper particle specimen for different slices as well as the strain for each loading. Figure 4-11 shows the cross-sectional CT image for non-copper particle specimen for different slices and the strain for each loading. Finally, Figure 4-12 shows the graph for strain ε_{zz} across the *x*-length from the middle of *z*-length where *z*=2.5 mm across the slices of copper and non-copper specimen. As can be seen from Figure 4-10 and Figure 4-11 clear strain bands are visible for copper specimen across the direction of yarn while these strain fields are not as visible for the non-copper specimen. Also, in the Figure 4-12 (a), the ε_{zz} strain across the *x*-length has periodicity and as the load increases, the strain on the specimen increases for the copper specimen. While the non-copper specimen, in the Figure 4-12 (b), the ε_{zz} strain across the *x*-length does not have periodicity, the peaks for different loading reach maxima across different *x*-length. All the discussion points conclude that for the specimen with seeded particles helps in better correlation which results to

more accurate displacement as well as strain fields. Therefore, the particle seeded sample will be further examined in this manuscript.

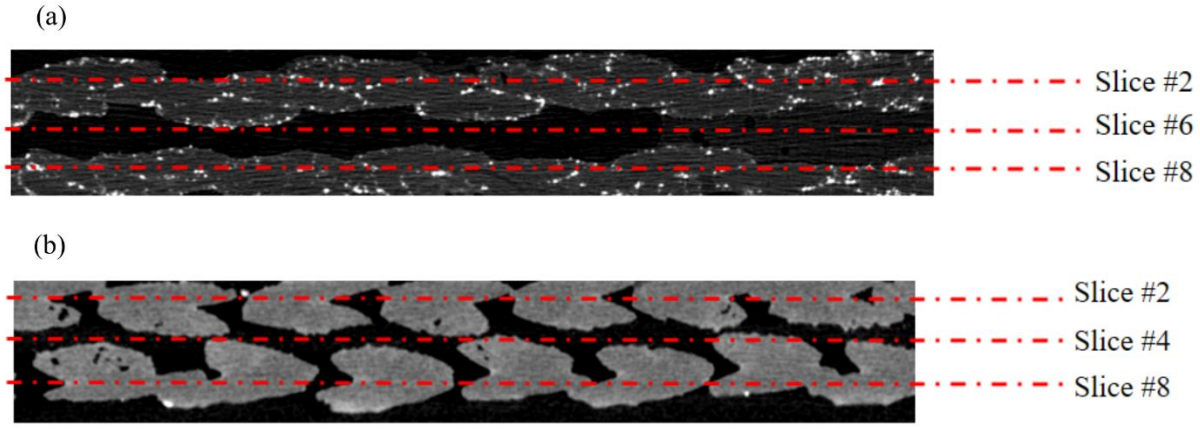

Figure 4-9: Cross-sectional top view Micro-CT image highlighting the slices used for generating displacement and strain map for (a) copper specimen (b) non-copper specimen.

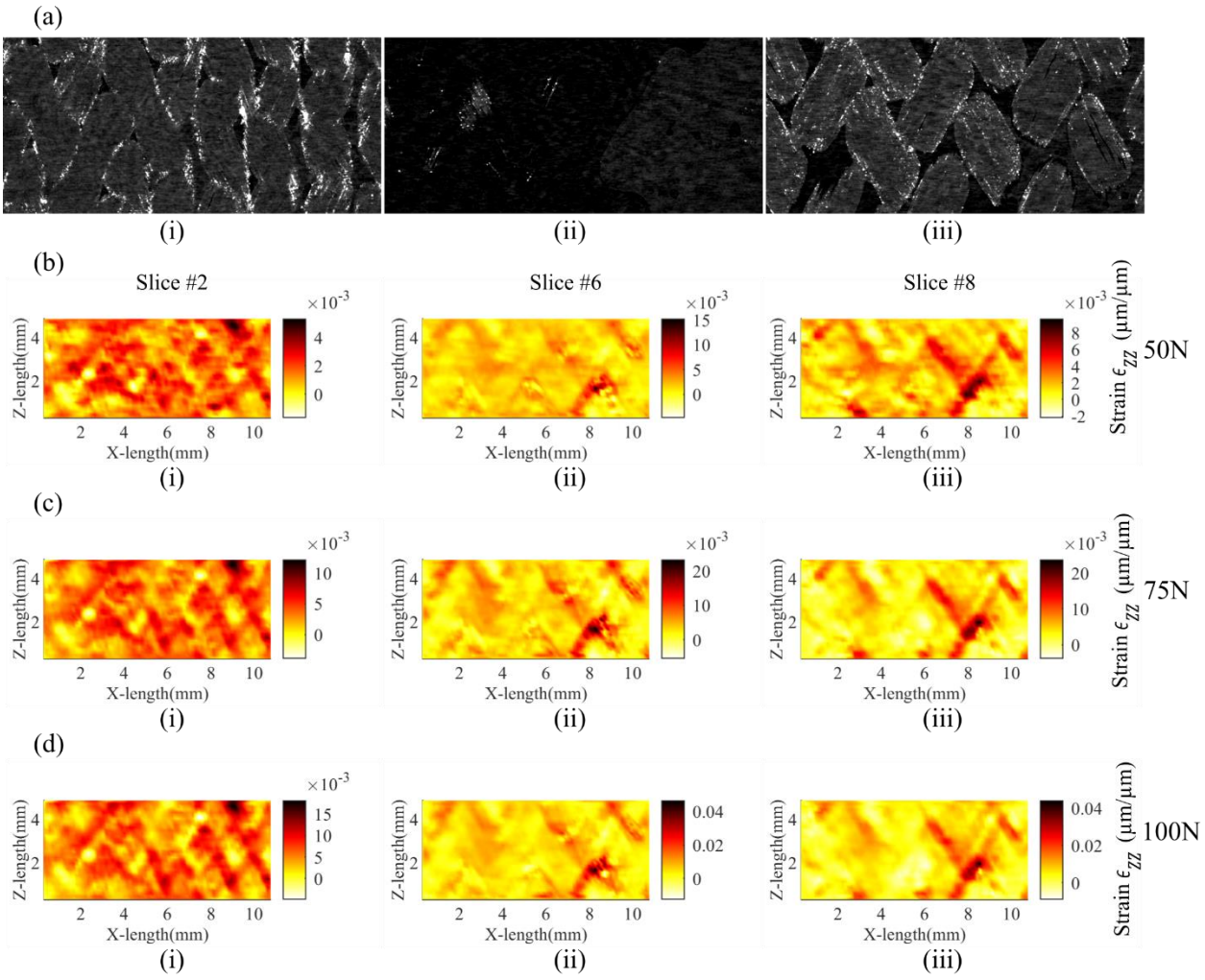

Figure 4-10: (a) Cross-sectional Micro-CT image of copper specimen at different slices. ε_{zz} strain map for (b) 50N (c) 75N and (d) 100N loading cases across the slice of copper specimen.

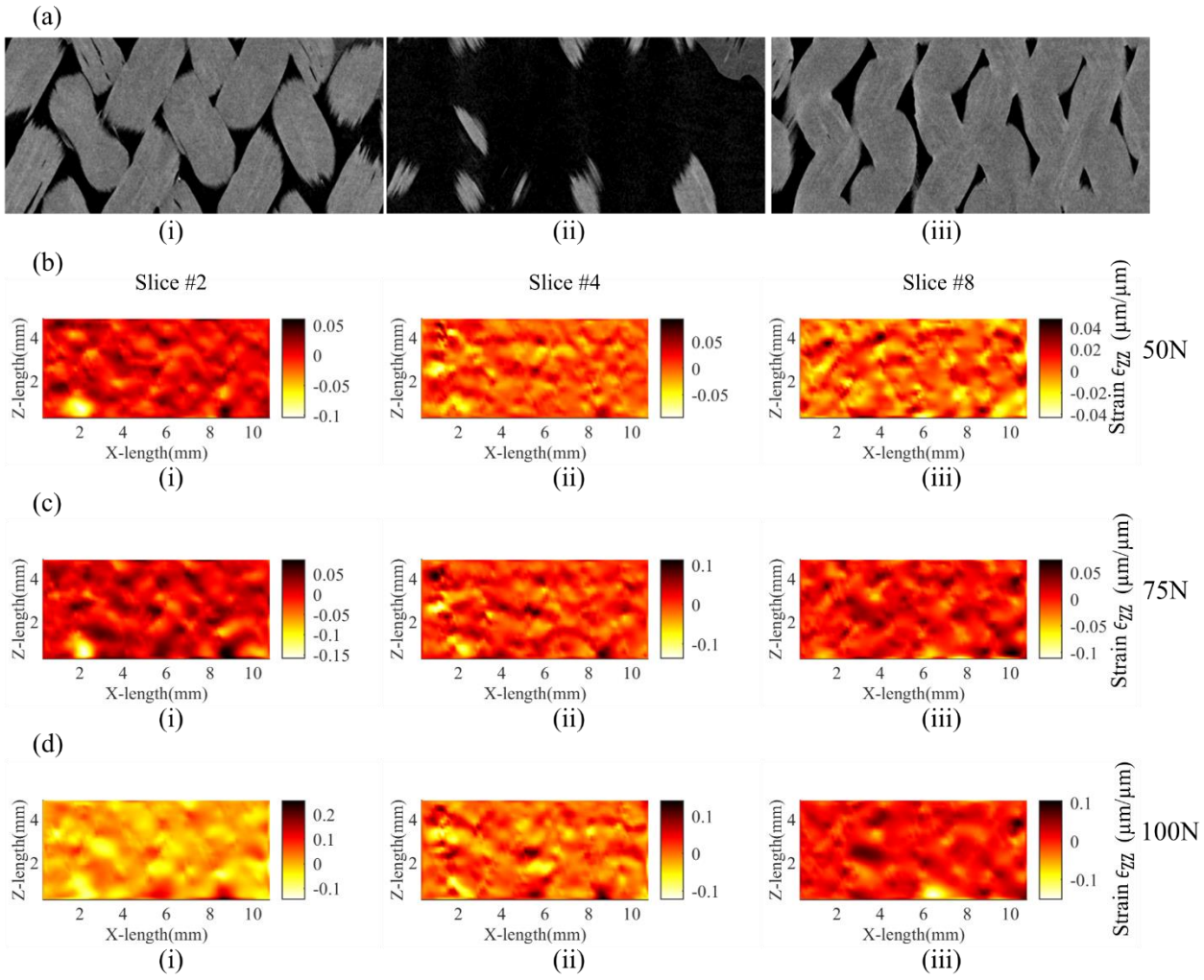

Figure 4-11: (a) Cross-sectional Micro-CT image of non-copper specimen at different slices. ε_{zz} strain map for (b) 50N (c) 75N and (d) 100N loading cases across the slice of non-copper specimen.

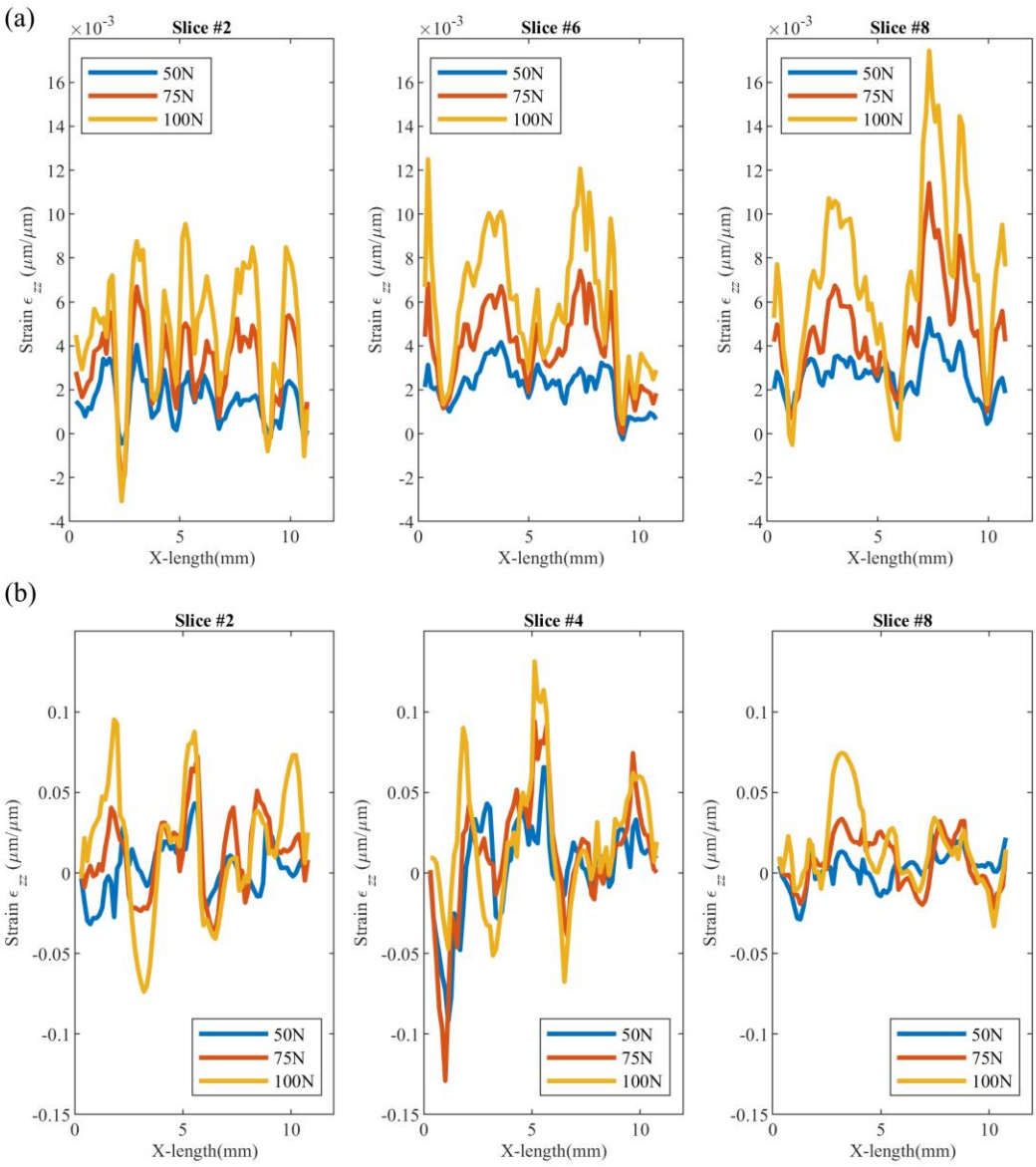

Figure 4-12: Strain ε_{zz} across the X-length from the middle of Z-length across the slices of (a) copper specimen (b) non-copper specimen.

4.3.3 Displacement & Strain Map

The data collected from the DVC provides a large quantity of information with the displacement and strain maps of the structure. The Figure 4-9(a) shows the slice locations used for displacement as well as strain maps. Slice #2 and Slice #8 lies on the fibre while slice #6 is for the

resin part of the structure. The displacement maps of the sample are shown in Figure 4-13. The front view of each slice is shown in Figure 4-13(a). The Figure 4-13(b)-(d) shows the *x*-displacement behaviour along the *x*-*z* slices of the structure for loadings of 50N, 75N and 100N with a preload of 25N. As the load step increases, the magnitude of the displacement along the *x*-direction also increases. The expected *x*-displacement is because of the intertwining of braid yarns, when in tension the braid angle of the yarn becomes smaller in turn giving both *x* and *z* displacement components.

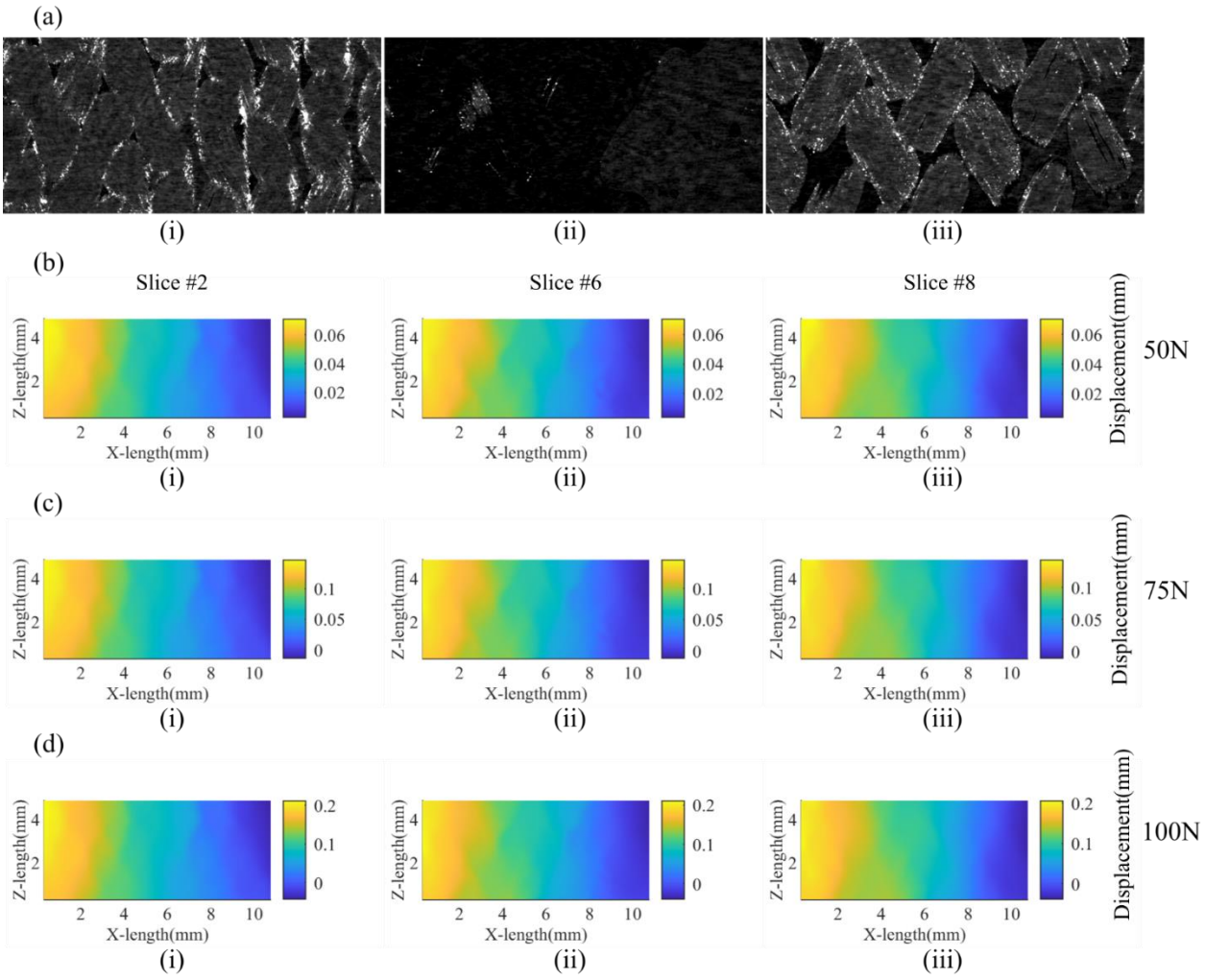

Figure 4-13: (a) Cross-sectional Micro-CT image of copper specimen at different slices. X-Displacement map for (b) 50N (c) 75N and (d) 100N loading cases across the slice of copper specimen.

The Figure 4-14 below shows the *z*-displacement of the specimen for different *x*-*z* plane slices with increasing loads. As the load increases from 25N to 100N, the magnitude of *z*-displacement also increases. Similar to the *x*-displacement, there is more visible displacement on the left side of slice as compared to the right side. There is uneven distribution of displacement for slice #6 and slice #8 under different loads, which may be because of more gaps in the braid yarns.

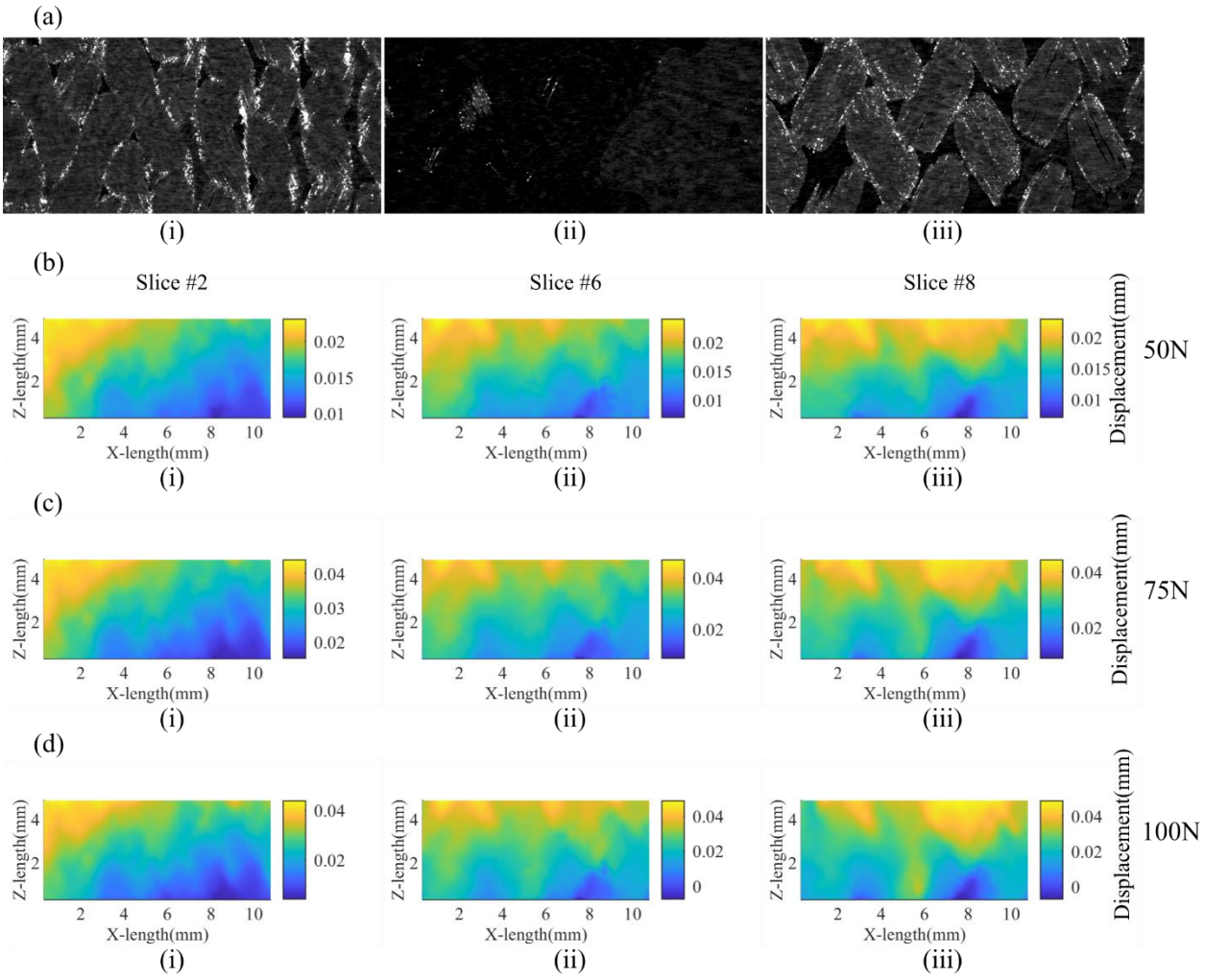

Figure 4-14: (a) Cross-sectional Micro-CT image of copper specimen at different slices. Z-Displacement map for (b) 50N (c) 75N and (d) 100N loading cases across the slice of copper specimen.

Only ε_{xx} and ε_{zz} strain maps were considered for discussion, not ε_{yy}, because the thickness in the *y*-direction is small as compared to the other dimensions. Further the loading direction is in *x-z* plane, therefore ε_{yy} is not significant for this analysis. The Figure 4-15 shows the ε_{xx} strain map for different loading conditions compared with the respective slices. As the force is increased from 25N to 100N, the magnitude of strain increases for each slice of the specimen. Negative strain

bands are formed along the braid yarn direction of the specimen. The Figure 4-16 shows the ε_{xx} strain over the *x*-length from the middle of z-length. The peaks and trough have a periodic behaviour with multiple loadings for each slice. The slice #2 has the highest negative strain of approximately 0.065 and across different slices, the magnitude of peak strain decreases. Also, it can be concluded that the peak strain increases with the increasing load.

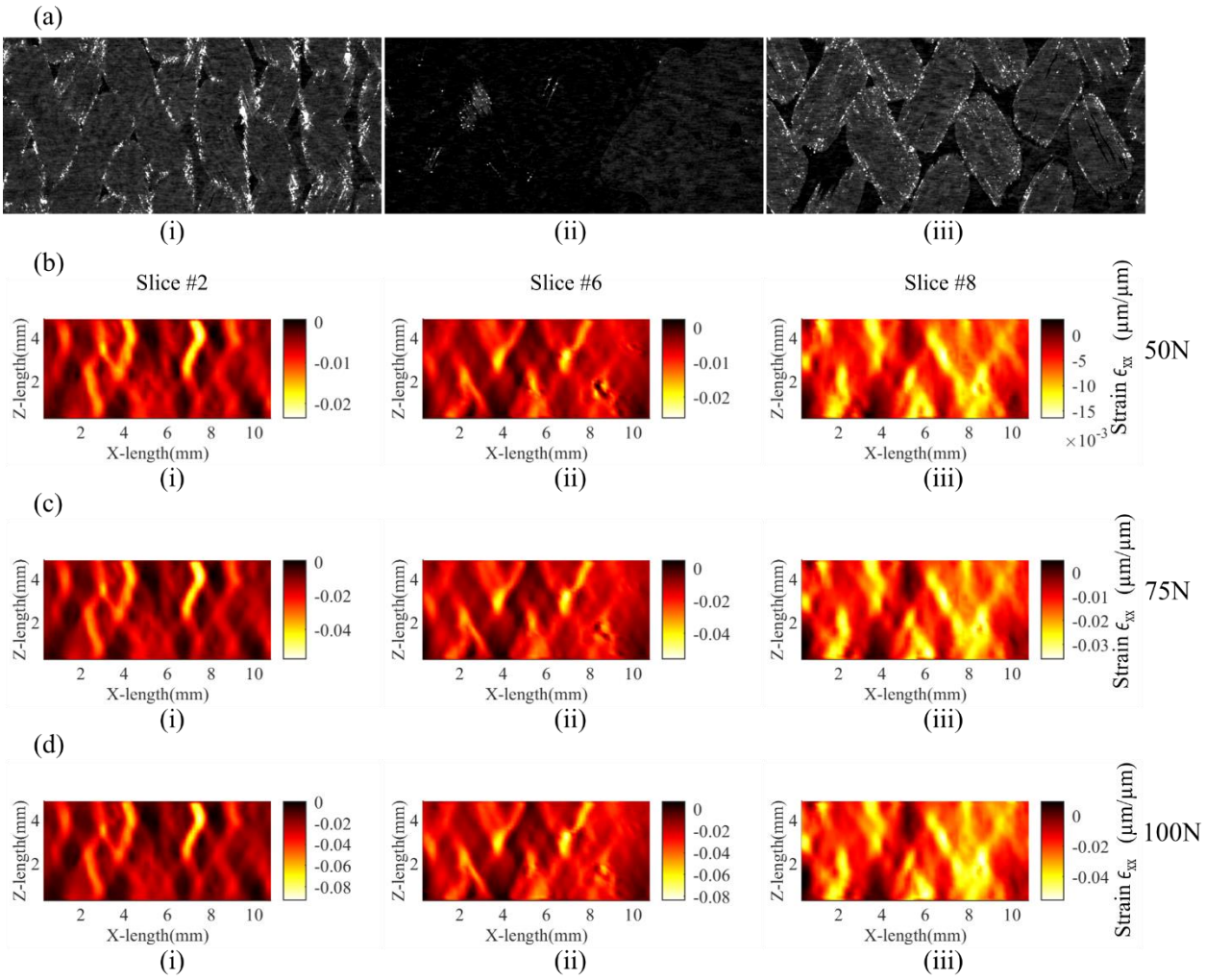

Figure 4-15: (a) Cross-sectional Micro-CT image of copper specimen at different slices. ε_{xx} Strain map for (b) 50N (c) 75N and (d) 100N loading cases across the slice of copper specimen.

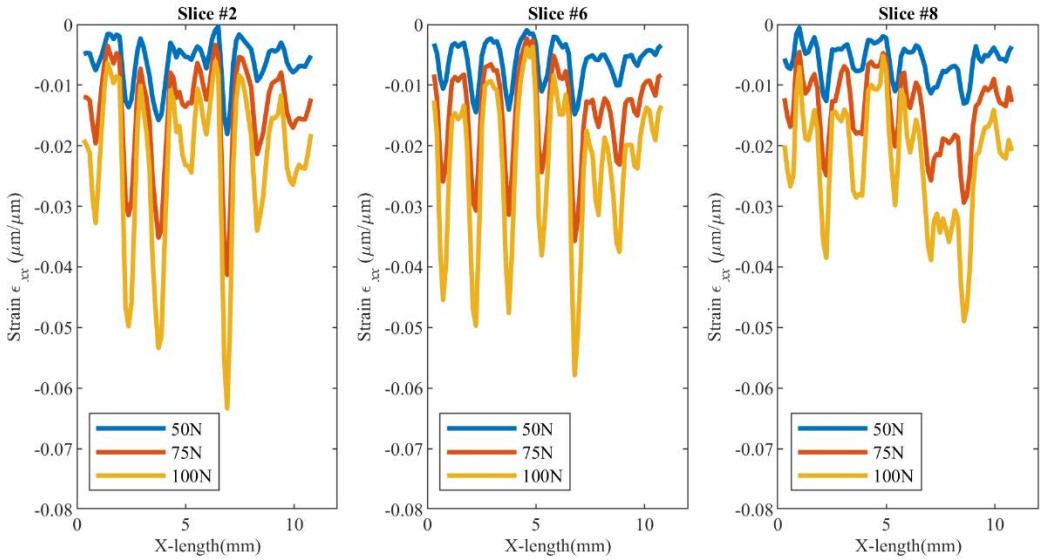

Figure 4-16: Strain ε_{xx} across the X-length from the middle of Z-length across the slices of copper specimen.

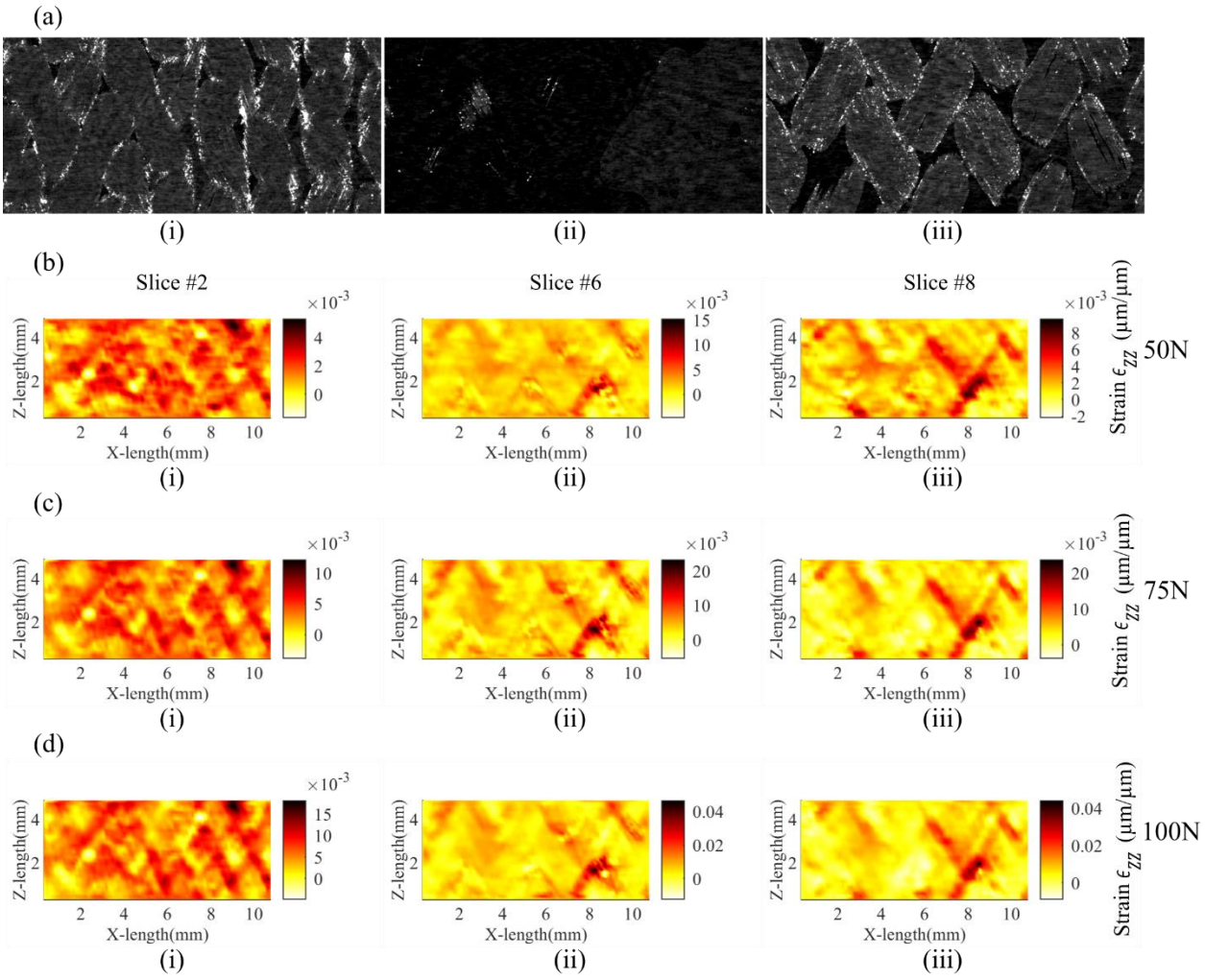

Figure 4-17: (a) Cross-sectional CT image of copper specimen at different slices. ε_{zz} Strain map for (b) 50N (c) 75N and (d) 100N loading cases across the slice of copper specimen.

The Figure 4-17 shows the ε_{zz} strain for three different cross-sectional *x-z* plane slices for 50N, 75N and 100N loading conditions. As can be seen from the figure, the strain increases with the increase in load. Also, a positive strain bands are observed along the direction of the braid yarns. High region of strain can be found along the strain bands. The strain band formation in slice #8 is different in the left side as compared to the right side, which might be because of the out of plane movement of the sample from the left side. The Figure 4-18 shows the ε_{zz} strain across the

x-length from the middle of *z*-length. For the slice#2, the peaks and troughs along *x*-length has a periodic behaviour. Also, the intensity of strain increases with increase in load. Slice #6 covers the matrix region with limited braids, which leads to less strain peaks over the *x*-length but higher magnitude. Slice #8 has a high strain region in the lower left region of the slice which can be observed in the graph with the peak strain (µm/µm).

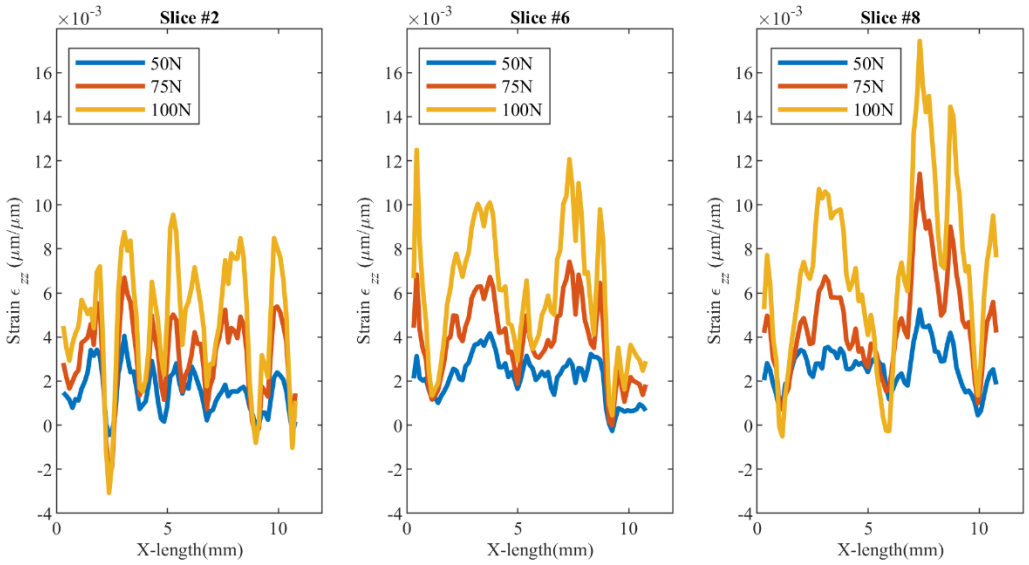

Figure 4-18: Strain ε_{zz} across the X-length from the middle of Z-length across the slices of copper specimen.

Cerbu *et al.* in his DIC study of carbon-aramid woven composite under tensile loading found similar surface z-displacement but more uniform and linear distribution of displacement [9]. For the axial strain, the strain bands were in horizontal direction with a very small width distributed similarly across the specimen. The whole sample had similar small strain distribution to each other for multiple loadings. The author did not discuss the results with regards to the displacement and strain map generated through DIC. Melenka & Carey in their study of diamond and regular tubular braided composite using 3D-DIC found similar high axial strain band formations along the

direction of braids [32]. The strain variation along the sample height also showed similar periodicity with the peak of strain coinciding at the intersection of braids. Similarly for the transverse strain, the strain bands were prominent along the direction of braid yarns. Also, the field of view for their paper was much larger as compared to the current study. The smaller VOI leads to better examination of strains in localized regions as compared to Melenka and Carey's study.The results obtained from the Micro-CT and DVC process shown in Figures 15 and 17, strain developed is different for different layers and not necessarily have a similar pattern across the slices. The results from this work show that strain fields within the braided samples can be examined for different layers which is not possible with a conventional 2D or 3D DIC process.

Most of the studies working on braided composite with DVC are focused more on the damage and failure investigation than the discussion of strain map across the specimen. The input of DVC results is still limited as the authors mostly rely on the Micro-CT datasets to find damage within a sample. Holmes *et al.* use of DVC is limited for mechanical characterization of woven fabric [24]. The damage characteristics rely more on the Micro-CT data than the DVC itself. Mehdikhani *et al.* used DVC for crack detection and damage initiation in carbon fibre reinforced composite [25]. They were able to see high strain line along the specimen where cracks were generated. The distribution of strain for the author was different from the results seen for Carbon-Aramid hybrid braided sample in this study, because of different specimen standard and different fibre orientation composite. The focus of their study was more towards damage mechanism while in this study objective is towards understanding the strain distribution within hybrid braids. Presently, no other paper was found understanding the strain distribution in-depth for textiles and braided composites.

The results from the DVC can be different from other papers because of the matrix used for the sample. PDMS has low mechanical properties as compared to the epoxy resins generally used in composites. PDMS was selected for the matrix in this study due to the load capacity of the MTS integrated testing stage. Epoxy makes the composite specimen brittle and stiff which is not the same with PDMS. Because of this behavior of PDMS, the results do not find any presence of matrix cracking. In terms of hybrid braided fibres, the difference in density is very less for carbon and aramid fibres leading to similar attenuation coefficient. Because of which it is difficult to differentiate them through Micro-CT data.

The above results are representative results that the DVC method offers. More data can be extracted from the results depending upon the study focus. For instance, all the strain fields indicated in Equation (4-2) for each slice can also be generated for the sample. Further this data creates nodal points which can be imported into finite element analysis (FEA) software for mesh generation. It can help improve the FEA models for the braided composites as well as internal microstructure of the braided specimen. Also, with a smaller pixel size of Micro-CT scans, a unit cell can be studied under loading and a better model can be generated. The results from DVC are compared with the analytical model in Appendix B.

4.4 Conclusions

Carbon-Aramid hybrid braided composite specimen with PDMS as the matrix was manufactured with the help of vacuum bagging and heated in oven. The samples were loaded in a Micro-CT under tension using inbuilt material testing stage. A preload of 25N and step load of 50N, 75N and 100N was applied. Using Micro-CT, the data for each loading is collected.

The image stack of reconstructed data under different loading was used for measuring full-field strain and displacement using DVC. Samples with copper particle and non-particle specimen

was compared to understand the effectiveness of particles in DVC. It was found that with the introduction of copper particles in the specimen, there was a drastic increase in the percentage of good correlation for all the subsets in the volume. Comparing both seeded particle and natural contrast, seeded particle gives the better results. Further, the displacement field were generated across different slices of the specimen which showed increased in displacement with increase in loading. For the ε_{xx} strain fields, high negative strain bands were observed along the direction of fibres. For the ε_{zz} strain fields, high positive strain bands were formed along the direction of fibre. The strain bands were less prevalent as out-of-plane displacement was observed. It also highlights the anisotropy of the material since the displacement and strain field generated was not same for different slices. This shows the usefulness of DVC over other measuring techniques such as conventional DIC or strain gauges since neither method could obtain the strain data through the thickness of a composite material.

4.5 References

[1] J. P. Carey, "Introduction to braided composites," *Handb. Adv. Braided Compos. Mater. Theory, Prod. Test. Appl.*, pp. 1–21, Jan. 2017, doi: 10.1016/B978-0-08-100369-5.00001-5.

[2] D. S. Brookstein, "Processing advanced braided composites," *Adv. Compos. Process. Technol.*, pp. 33–36, 1988.

[3] N. Casale, D. Bristow, and C. M. Pastore, "Design and fabrication of a braided composite monocoque bicycle frame," *High-tech fibrous Mater. (ACS Symp. Ser. 457)*, 1991, doi: 10.1021/BK-1991-0457.CH006.

[4] W. Hao, Z. Huang, L. Zhang, G. Zhao, and Y. Luo, "Study on the torsion behavior of 3-D

braided composite shafts," *Compos. Struct.*, vol. 229, p. 111384, Dec. 2019, doi: 10.1016/J.COMPSTRUCT.2019.111384.

[5] G. W. Melenka and J. P. Carey, "Experimental analysis of diamond and regular tubular braided composites using three-dimensional digital image correlation:," *https://doi.org/10.1177/0021998317695418*, vol. 51, no. 28, pp. 3887–3907, Feb. 2017, doi: 10.1177/0021998317695418.

[6] G. W. Melenka *et al.*, "Manufacturing processes for braided composite materials," *Handb. Adv. Braided Compos. Mater. Theory, Prod. Test. Appl.*, pp. 47–153, Jan. 2017, doi: 10.1016/B978-0-08-100369-5.00003-9.

[7] G. W. Melenka and C. Ayranci, "Advanced measurement techniques for braided composite structures: A review of current and upcoming trends," doi: 10.1177/0021998320903105.

[8] C. Ayranci and J. Carey, "2D braided composites: A review for stiffness critical applications," *Compos. Struct.*, vol. 85, no. 1, pp. 43–58, Sep. 2008, doi: 10.1016/J.COMPSTRUCT.2007.10.004.

[9] C. Cerbu, S. Ursache, M. F. Botis, and A. Hadăr, "Simulation of the Hybrid Carbon-Aramid Composite Materials Based on Mechanical Characterization by Digital Image Correlation Method," *Polym. 2021, Vol. 13, Page 4184*, vol. 13, no. 23, p. 4184, Nov. 2021, doi: 10.3390/POLYM13234184.

[10] L. Vásárhelyi, Z. Kónya, Kukovecz, and R. Vajtai, "Microcomputed tomography–based characterization of advanced materials: a review," *Materials Today Advances*, vol. 8. Elsevier Ltd, p. 100084, Dec. 01, 2020, doi: 10.1016/j.mtadv.2020.100084.

[11] G. W. Melenka and A. Gholami, “Fiber identification of braided composites using micro-computed tomography,” *Compos. Commun.*, vol. 27, p. 100813, Oct. 2021, doi: 10.1016/J.COCO.2021.100813.

[12] Y. Gu *et al.*, “Torsion damage mechanisms analysis of two-dimensional braided composite tubes with digital image correction and X-ray micro-computed tomography,” *Compos. Struct.*, vol. 256, p. 113020, Jan. 2021, doi: 10.1016/J.COMPSTRUCT.2020.113020.

[13] L. Shi, Z. Wu, X. Cheng, Z. Pan, and Y. Yuan, “Transverse impact response of hybrid biaxial/uniaxial braided composite tubes,” *Eng. Struct.*, vol. 244, p. 112816, Oct. 2021, doi: 10.1016/J.ENGSTRUCT.2021.112816.

[14] H.-F. Yin, W. Zhou, P.-F. Zhang, and L.-H. Ma, “Flexural progressive damage and failure behavior of carbon-aramid/epoxy hybrid woven composites,” doi: 10.1177/0021998320962187.

[15] R. A. Naik, P. G. Ifju, and J. E. Masters, “Effect of Fiber Architecture Parameters on Deformation Fields and Elastic Moduli of 2-D Braided Composites,” *http://dx.doi.org/10.1177/002199839402800705*, vol. 28, no. 7, pp. 656–681, Jul. 2016, doi: 10.1177/002199839402800705.

[16] B. Pan, K. Qian, H. Xie, and A. Asundi, “Two-dimensional digital image correlation for in-plane displacement and strain measurement: a review,” *Meas. Sci. Technol.*, vol. 20, no. 6, p. 062001, Apr. 2009, doi: 10.1088/0957-0233/20/6/062001.

[17] Y. Zheng *et al.*, “Tensile response of carbon-aramid hybrid 3D braided composites,” *Mater. Des.*, vol. 116, pp. 246–252, Feb. 2017, doi: 10.1016/J.MATDES.2016.11.082.

[18] C. K. Leung, G. W. Melenka, D. S. Nobes, and J. P. Carey, “The effect on elastic modulus of rigid-matrix tubular composite braid radius and braid angle change under tensile loading,” *Compos. Struct.*, vol. 100, pp. 135–143, Jun. 2013, doi: 10.1016/J.COMPSTRUCT.2012.12.038.

[19] A. Armanfard and G. W. Melenka, “Experimental evaluation of carbon fibre, fibreglass and aramid tubular braided composites under combined tension–torsion loading,” *Compos. Struct.*, vol. 269, p. 114049, Aug. 2021, doi: 10.1016/J.COMPSTRUCT.2021.114049.

[20] A. Buljac *et al.*, “Digital Volume Correlation: Review of Progress and Challenges,” *Exp. Mech.*, vol. 58, no. 5, pp. 661–708, Jun. 2018, doi: 10.1007/S11340-018-0390-7/FIGURES/25.

[21] B. Pan and B. Wang, “Some recent advances in digital volume correlation,” *Opt. Lasers Eng.*, vol. 135, p. 106189, Dec. 2020, doi: 10.1016/J.OPTLASENG.2020.106189.

[22] B. K. Bay, T. S. Smith, D. P. Fyhrie, and M. Saad, “Digital volume correlation: Three-dimensional strain mapping using X-ray tomography,” *Exp. Mech. 1999 393*, vol. 39, no. 3, pp. 217–226, 1999, doi: 10.1007/BF02323555.

[23] A. Buljac *et al.*, “Digital Volume Correlation: Review of Progress and Challenges,” *Exp. Mech.*, vol. 58, no. 5, pp. 661–708, Jun. 2018, doi: 10.1007/s11340-018-0390-7.

[24] J. Holmes, S. Sommacal, Z. Stachurski, R. Das, and P. Compston, “Digital image and volume correlation with X-ray micro-computed tomography for deformation and damage characterisation of woven fibre-reinforced composites,” *Compos. Struct.*, vol. 279, p. 114775, Jan. 2022, doi: 10.1016/J.COMPSTRUCT.2021.114775.

[25] M. Mehdikhani *et al.*, “Digital volume correlation for meso/micro in-situ damage analysis in carbon fiber reinforced composites,” *Compos. Sci. Technol.*, vol. 213, p. 108944, Sep. 2021, doi: 10.1016/J.COMPSCITECH.2021.108944.

[26] C. Liu, Y. Chen, D. Shi, J. Marrow, X. Jing, and X. Yang, “In situ investigation of failure in 3D braided SiCf/SiC composites under flexural loading,” *Compos. Struct.*, vol. 270, p. 114067, Aug. 2021, doi: 10.1016/J.COMPSTRUCT.2021.114067.

[27] C. S. Timpano and G. W. Melenka, “Artificial seeding for micro-computed tomography image contrast enhancement for digital volume correlation,” *Compos. Part B Eng.*, vol. 215, p. 108809, Jun. 2021, doi: 10.1016/J.COMPOSITESB.2021.108809.

[28] B. P. Croom *et al.*, “Interlaboratory Study of Digital Volume Correlation Error Due to X-Ray Computed Tomography Equipment and Scan Parameters: an Update from the DVC Challenge,” *Exp. Mech.*, vol. 61, no. 2, pp. 395–410, Feb. 2021, doi: 10.1007/S11340-020-00653-X/FIGURES/10.

[29] J. Gonzalez and J. Lambros, “A Parametric Study on the Influence of Internal Speckle Patterning for Digital Volume Correlation in X-Ray Tomography Applications,” *Exp. Tech.*, vol. 40, no. 5, pp. 1447–1459, Oct. 2016, doi: 10.1007/S40799-016-0145-2/FIGURES/11.

[30] J. Yang, L. Hazlett, A. K. Landauer, and C. Franck, “Augmented Lagrangian Digital Volume Correlation (ALDVC),” *Exp. Mech.*, vol. 60, no. 9, pp. 1205–1223, Nov. 2020, doi: 10.1007/s11340-020-00607-3.

[31] C. S. Timpano and G. W. Melenka, “Digital volume correlation analysis of polylactic acid based fused filament fabrication printed composites:,”

https://doi.org/10.1177/00219983211020500, May 2021, doi: 10.1177/00219983211020500.

[32] G. W. Melenka and J. P. Carey, "Experimental analysis of diamond and regular tubular braided composites using three-dimensional digital image correlation," *J. Compos. Mater.*, vol. 51, no. 28, pp. 3887–3907, Dec. 2017, doi: 10.1177/0021998317695418/ASSET/IMAGES/LARGE/10.1177_0021998317695418-FIG2.JPEG.

Chapter 5 Conclusions and Future Work

5.1 Conclusions

The thesis investigated the internal microstructure using Digital Volume Correlation for composite material. A copper filled PLA manufactured using FFF was investigated in Chapter 3 and Carbon-Aramid Hybrid braided composite was investigated in Chapter 4.

Four copper filled PLA samples with different infill percentage of 20, 40, 60 and 80 were printed using FFF. The specimen was manufactured according to the modified ASTM D638-14 type V. The specimens were loaded in Micro-CT with a preload of 50N and step load of 150N. The porosity percentage and copper particle distribution was calculated for the reconstructed micro-CT data using image processing techniques. The porosity percentage for 60% infill was lower than expected 40% for both microscope data as well micro-CT data. The reason might be because of the printing parameters such as layer height and printing speed which are not optimized. Further, using DVC, the displacement map of internal layers for each infill percentage was generated. It showed with the increase in infill percentage the displacement for the sample decreases. The volumetric strain,ε_{zz}, shows presence of high strain was observed along the direction of raster angle i.e +45/-45 orientation.

Similarly, the method was explored to understand carbon-aramid hybrid braided composites. Two carbon-aramid braided composite samples were manufactured using vacuum bagging technique and further kept at 100° C in an oven to cure it in an hour. One sample as seeded with copper particles with a size of 25 µm and other was not seeded with any particle. Both the samples were loaded in tension on material testing stage which is inbuilt in Micro-CT. The sample was pre-loaded with 25N and step loads of 50N, 75N and 100N. The scan data were collected for each loading. The image stack of reconstructed data was processed to get the particle distribution

of the sample and also to generate full field internal displacement and strain fields. Copper seeded sample and non-seeded sample was compared with each other to find the effectiveness of the particles in DVC. It was found that the copper seeded particle gave the best results for each loading condition as compared to non-seeded sample. The sample without particle had above 50% bad subset for each loading while for the copper seeded specimen had less than 15% bad subset at the highest 100N loading. Also, the strain ε_{zz} values from the non-seeded specimen had a large standard deviation as compared to seeded sample. The plot of strain vs the sample length was not periodic and also the strain was found to be higher for lower loading conditions in non-seeded sample. This shows that the seeded particle specimen gives better results in DVC. Also, X-displacement map and Z-displacement map was generated. With the increase in loading the displacement increased for the copper seeded specimen. For the ε_{xx} strain fields, high negative strain bands were observed along the direction of fibres. For the ε_{zz} strain fields, high positive strain bands were formed along the direction of fibre. Also, there was presence of out-of-plane displacement because of which the strain bands were less prevalent. The strain fields were similar but not the same for different slices of the specimen, which shows the anisotropy and non-homogeneity of the composite material. This proves the usefulness of DVC over other surface measuring techniques for examining the internal displacement and strain behavior of the complex materials.

5.2 Future Work

The thesis focused on the application of Digital Volume Correlation for generating internal displacement and strain fields for composites. It is still in the developing phase so more research needs be done to further increase the usage in the mechanical field.

With the FFF composites, the current study focused only on the different infill percentage under loading. There are lot of process parameters which can be investigated such as effects of different layer height, printing pattern, printing speed etc. It will help to better understand the microstructure under loading. Also, other Additive Manufacturing methods such as stereolithography can have huge advantage with DVC analysis because of their complex structure.

In terms of textile and braided composites, chapter 4 only focused on flat hybrid braided composites under tensile loading. The tensile loading was limited to elastic region of the composite. The plastic region under tensile region can be explored to understand the progressive failure of hybrid braided composites. Also, the current study was a single flat braid but multiple braids in multiple configurations can be explored to understand the interaction between layers.

Hounsfield Unit (HU) is a relative quantitative measurement of radio density used in CT scans. The HU scale of different materials are known and can be used for segmentation of different materials in the sample such as copper in PLA.Both FFF composites as well as hybrid braided composites was explored under tensile loading. Other loading conditions such as compression, bending can be explored to understand its internal behaviour. Another potential research would be comparing all the available DVC softwares and have a comparative analysis. This will help the new researchers in the field as a guidance for the softwares suitable for their objectives.

DVC results can be further used in the FEA analysis as well as analytical modelling. The thesis dwell into some of the analytical model and its comparison with the DVC results. But, a comprehensive study can be explored to develop analytical models which takes into consideration various parameters for it to be more accurate. Also, FEA models can be improved based on the DVC data and can be modelled close to real experimental values.

Appendix A FFF Analytical Modeling

A.1 Volume Average Stiffness Method

Melenka *et al*. in their paper used Volume Average Stiffness method for continuous Kevlar fibre reinforced 3D printed structures to find the effective elastic properties [1]. A similar approach can be used for the sample used in the current experiment with minor modifications to model to examine the sample elastic behaviour.

The first step is to calculate the micromechanical properties of the solid and infill region. The model developed by Rodriguez *et al.* was used to calculate the constants [2]. Here E_{11}, Equation (A-1), is the longitudinal modulus, E_{22}, Equation (A-2), is the transverse modulus, G_{12}, Equation (A-3), is the shear modulus and ν_{12}, Equation (A-4) is the major Poisson's ratio for the 3D printed components. The mechanical properties used for PLA extracted from the paper by Torres *et al.* in the modelling are given in Table A-1 [3]. The equations give the micromechanical properties of infill and solid layers. The symbol ρ_1 signifies the void density of each component. For the infill region, ρ_1 was found to be 0.3397 based on the porosity calculation from Micro-CT data. And for the solid region, a porosity of 5% was assumed. M. Ivey *et al*. found the void fraction for 100% infill PLA/CF to be around 12.1±2% which is close to the value of our assumption [4]. Also, it needs to be considered the infill pattern is 90° rectilinear. M. Saleh *et al*. in their study found the void percentage for 100% infill Cu wire reinforced PLA to be 2.15%, though the printing pattern was different which is unidirectional for their study [5]. Y. Ibrahim *et al*. also found void percentage for continuous cu wire PLA sample with different parameters, one of which is PLA with Cu wire and 0.6mm nozzle [6]. The value was 5.58% which is quite close to our assumed value.

Table A-1: Mechanical properties of PLA.

Material Property	Values
Elastic Modulus (E)	3.5 GPa
Shear Modulus (G)	1.287 GPa
Poisson's Ratio (ν)	0.36

$$E_{11} = (1 - \rho_1)E \tag{A-1}$$

$$E_{22} = \left(1 - \rho_1^{1/2}\right)E \tag{A-2}$$

$$G_{12} = G\frac{(1 - \rho_1)\left(1 - \rho_1^{1/2}\right)}{(1 - \rho_1) + \left(1 - \rho_1^{1/2}\right)} \tag{A-3}$$

$$\nu_{12} = (1 - \rho_1)\nu \tag{A-4}$$

$$\nu_{21} = (1 - \rho_1^{1/2})\nu \tag{A-5}$$

After determining the micromechanical properties, the compliance matrix is calculated with the found values for transversely isotropic materials. [T], Equation (A-8), denotes rotation matrix which is calculated to transform solid and infill region. Rotations are defined using equations (A-6) and (A-7). $\left[S'_{xyz}\right]$ is the new stiffness matrix relative to the global coordinate system. θ is the angle of solid and infill layers.

$$[S] = \begin{bmatrix} \frac{1}{E_1} & -\frac{\nu_{21}}{E_2} & -\frac{\nu_{31}}{E_3} & 0 & 0 & 0 \\ -\frac{\nu_{12}}{E_1} & \frac{1}{E_2} & -\frac{\nu_{32}}{E_3} & 0 & 0 & 0 \\ -\frac{\nu_{13}}{E_1} & \frac{\nu_{23}}{E_2} & \frac{1}{E_3} & 0 & 0 & 0 \\ 0 & 0 & 0 & \frac{1}{G_{23}} & 0 & 0 \\ 0 & 0 & 0 & 0 & \frac{1}{G_{13}} & 0 \\ 0 & 0 & 0 & 0 & 0 & \frac{1}{G_{12}} \end{bmatrix} \quad \text{(A-6)}$$

$$S_{XYZ} = [T]^T \left[S'_{xyz}\right][T] \quad \text{(A-7)}$$

$$[T] = \begin{bmatrix} c^2 & s^2 & 0 & 0 & 0 & 2cs \\ s^2 & c^2 & 0 & 0 & 0 & -2cs \\ 0 & 0 & 1 & 0 & 0 & 0 \\ 0 & 0 & 0 & c & s & 0 \\ 0 & 0 & 0 & -s & c & 0 \\ -cs & cs & 0 & 0 & c^2 & -s^2 \end{bmatrix} \quad \text{(A-8)}$$

$$c = \cos(\theta) \quad \text{(A-9)}$$

$$s = \sin(\theta) \quad \text{(A-10)}$$

The third part is the stiffness averaging equation, $[C^G]$ Equation (A-11) uses the volume fraction of each component to determine the contribution and to find the mechanical properties. Further it is inversed as shown in equation and the effective elastic constants, Equation (A-13), of the specimen are determined.

$$[C^G] = V_{fshell}[C_{shell}] + V_{finfill-\theta}\left[C_{infill-\theta}\right] + V_{finfill+\theta}\left[C_{infill+\theta}\right] + V_{fsolid-\theta}[C_{solid-\theta}] + V_{fsolid+\theta}[C_{solid+\theta}] \quad \text{(A-11)}$$

$$S^G = [C^G]^{-1} \quad \text{(A-12)}$$

$$E_x = \frac{1}{S_{11}^g}, \quad E_y = \frac{1}{S_{22}^g}, \quad E_z = \frac{1}{S_{33}^g} \quad \text{(A-13)}$$

$$E_x = \frac{\sigma}{\epsilon} \quad \text{(A-14)}$$

$$\sigma = \frac{F}{A} \quad \text{(A-15)}$$

Solving the above equations, Table A-2 shows the comparison of strain results found using DVC and analytical model. There are many flaws with the analytical model, it assumes the bonding to be perfect between layers and also does not consider process parameters like raster type. Also, the results obtained from DVC are from the experiments directly. The above model gives out the effective strain for the whole specimen unlike DVC which plots the strain map layer by layer. These demonstrates how the analytical model are ineffective for FFF and with DVC lies a huge potential to better understand internal structure as well as further improve these analytical models. Finite element models, such as the constitutive model by Somireddy *et al.* are better suited for the examination of the internal structure of FFF parts and can be readily compared with DVC analysis [7].

Table A-2: Comparison of Strain values with analytical model.

Infill percentage	Average Strain (ALDVC)	Average Strain (Analytical Model)
20	0.0072 ± 0.0034	0.0093
40	0.0086 ± 0.0057	0.0085
60	0.0071 ± 0.0030	0.0068
80	0.0072 ± 0.0013	0.0058

A.2 References

[1] G. W. Melenka, B. K. O. Cheung, J. S. Schofield, M. R. Dawson, and J. P. Carey, "Evaluation and prediction of the tensile properties of continuous fiber-reinforced 3D printed structures," *Compos. Struct.*, vol. 153, pp. 866–875, 2016, doi: 10.1016/j.compstruct.2016.07.018.

[2] J. F. Rodríguez, J. P. Thomas, and J. E. Renaud, "Mechanical behavior of acrylonitrile butadiene styrene fused deposition materials modeling," *Rapid Prototyp. J.*, vol. 9, no. 4, pp. 219–230, 2003, doi: 10.1108/13552540310489604/FULL/PDF.

[3] M. A. Saleh, R. Kempers, and G. W. Melenka, "A comparative study on the electromechanical properties of 3D-Printed rigid and flexible continuous wire polymer composites for structural health monitoring," *Sensors Actuators A Phys.*, vol. 328, p. 112764, Sep. 2021, doi: 10.1016/J.SNA.2021.112764.

[4] M. Ivey, G. W. Melenka, J. P. Carey, and C. Ayranci, "Characterizing short-fiber-reinforced composites produced using additive manufacturing," vol. 3, no. 3, 2017, doi:

10.1080/20550340.2017.1341125.

[5] M. A. Saleh, R. Kempers, and G. W. Melenka, “3D printed continuous wire polymer composites strain sensors for structural health monitoring,” 2019, doi: 10.1088/1361-665X/aafdef.

[6] Y. Ibrahim, G. W. Melenka, and R. Kempers, “Fabrication and tensile testing of 3D printed continuous wire polymer composites,” doi: 10.1108/RPJ-11-2017-0222.

[7] M. Somireddy, A. Czekanski, and C. V. Singh, “Development of constitutive material model of 3D printed structure via FDM,” *Mater. Today Commun.*, vol. 15, pp. 143–152, Jun. 2018, doi: 10.1016/J.MTCOMM.2018.03.004.

Appendix B Carbon-Aramid Analytical Modelling

B.1 Classical Laminate Plate Theory (CLPT)

The analysis for the specimen is done using Classical Laminate Plate Theory (CLPT). CLPT is an analytical model to predict the residual stress as well as strain of each layer of composite laminate under mechanical or temperature loads. There are many assumptions for the model: Laminate is assumed to be under plane stress, displacement of the specimen is very less compared to the laminate thickness, each lamina is assumed to be elastic orthotropic and the bond between the layers are perfect. CLPT models have been used by Carey and Ayranci to examine braided composite structures [1][2]. Further, to ease the complexity of hybrid models, we assumed each material as a single lamina instead of the inter-ply hybrid lamina. The laminate is assumed to be stacked in the order as shown in Figure B-1 (a); The braid angle was found to be 30° for the specimen using the method discussed in methodology section. +30° lamina of carbon, -30° lamina of Kevlar, layer of PDMS, -30° lamina of Kevlar and +30° lamina of carbon [3].

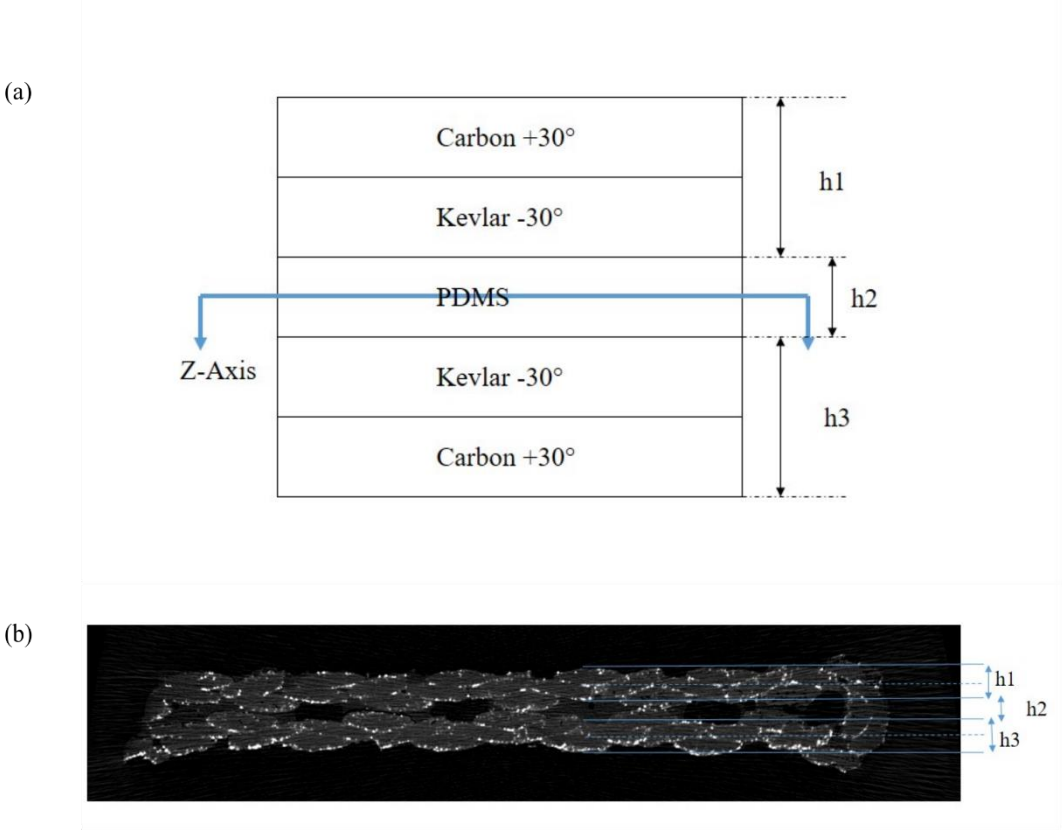

Figure B-1: Laminate stack assuming hybrid braid materials as an individual lamina.

As shown in Figure B-1 (b), the thickness of each layer was measured using the cross-sectional CT image using CTan software. The value of h1 and h3 was found to be 619.2 µm while the matrix region h2 was 481.6 µm. Further, the thickness of carbon and Kevlar lamina are assumed to be same so the thickness of each fibre layer is 310 µm.

Micro-Mechanical models are used to find properties of each of the different material lamina. The mechanical properties of each of the materials are shown in Table B-1 [4]–[6]. The rule of mixtures as well as rules of reciprocal was used as shown in Equation (B-1) – Equation (B-4).

$$E_1 = E_{1f}V_f + E_mV_m \tag{B-1}$$

$$\nu_{12} = \nu_f V_f + \nu_m V_m \tag{B-2}$$

$$\frac{1}{E_2} = \frac{V_f}{E_{1f}} + \frac{V_m}{E_m} \tag{B-3}$$

$$\frac{1}{G_{12}} = \frac{V_f}{G_{12f}} + \frac{V_m}{G_m} \tag{B-4}$$

Where E_1 is the longitudinal modulus of the lamina, E_{1f} is the longitudinal modulus of the fibres, V_f and V_m are the Volume fibre fraction & Volume matrix fraction respectively. The value of V_f is assumed to be 0.6 and the value of V_m is assumed to be 0.4[7]. E_m is the modulus of the matrix. Simillarly, ν_{12} is the Poisson's ratio of the lamina, ν_f & ν_m are the Poisson's ratio of the fibre and matrix respectively. E_2 is the transverse modulus of the lamina, G_{12} is the shear modulus of the lamina and G_{12f} and G_m is the shear modulus of the fibre & matrix respectively. Table B-2 shows the calculated mechanical properties of each material lamina. These calculations will be used to estimate the micro-mechanical properties and effective lamina properties of the Carbon-Aramid braided composite examined in this study.

Table B-1: Mechanical Properties of Fibres and Matrix [4]–[6].

Property	Kevlar 49	T-300 Carbon	PDMS
Longitudinal Modulus, E_{1f}, GPa	131	230	2.05×10^{-3}
Transverse Modulus, E_{2f}, GPa	7	15	2.05×10^{-3}
Axial Shear Modulus, G_{12f}, MPa	21	27	0.68×10^{-3}
Poisson's Ratio, ν_{12f}	0.33	0.12	0.4950

Table B-2: Mechanical properties of different material lamina.

Property	Kevlar/PDMS Lamina	Carbon/PDMS Lamina
E_1 (GPa)	78.6	138
E_2 (MPa)	11.25	11.27
G_{12} (MPa)	2.72	2.72
ν_{12}	0.3960	0.3180

A reduced stiffness matrix as shown in Equation (B-5) is calculated for all the laminas using E_1, E_2, G and ν values.

$$[Q] = \begin{bmatrix} Q_{11} & Q_{12} & Q_{13} \\ Q_{21} & Q_{22} & Q_{23} \\ Q_{31} & Q_{32} & Q_{33} \end{bmatrix} \quad \text{(B-5)}$$

Transformed stiffness matrix $[\bar{Q}]$ for each ply is calculated using [Q] and the transformation matrix [T], Equation (B-6), which is dependent on the angle of the ply as shown in Equation (B-7).

$$[T] = \begin{bmatrix} m^2 & n^2 & 2mn \\ n^2 & m^2 & -2mn \\ -mn & mn & m^2 - n^2 \end{bmatrix} \text{ where m=cos(θ), n=sin(θ)} \quad \text{(B-6)}$$

$$[\bar{Q}]_\theta = [Q][T] \quad \text{(B-7)}$$

The mid plane is defined as z=0, and based on that a coordinate system. Based on this system, [A], [B] and [D] are calculated, as shown in Equation (B-8)- Equation (B-10), where [A] is extensional stiffness matrix which relates in-plane forces to in-plane strains, [B] is coupling stiffness matrix which couples the force and moment terms to the mid-plane strains and mid-plane curvatures and [D] is bending stiffness matrix which relates bending moments to plate curvatures.

$$A_{ij} = \sum_{k=1}^{n} \left[\bar{Q}_{ij}\right]_k (h_k - h_{k-1}) \; where \; i,j = 1,2,6 \quad \text{(B-8)}$$

$$B_{ij} = \frac{1}{2}\sum_{k=1}^{n} \left[\bar{Q}_{ij}\right]_k (h_k^2 - h_{k-1}^2) \; where \; i,j = 1,2,6 \quad \text{(B-9)}$$

$$D_{ij} = \frac{1}{3}\sum_{k=1}^{n} \left[\bar{Q}_{ij}\right]_k (h_k^3 - h_{k-1}^3) \; where \; i,j = 1,2,6 \quad \text{(B-10)}$$

The equation (B-11) is solved using mid-plane strain and curvatures, and the known values of forces and moments.

$$\begin{bmatrix} N_x \\ N_y \\ N_{xy} \\ M_x \\ M_y \\ M_{xy} \end{bmatrix} = \begin{bmatrix} [A] & [B] \\ [B] & [D] \end{bmatrix} \begin{Bmatrix} \epsilon_x \\ \epsilon_y \\ \gamma_{xy} \\ K_x \\ K_y \\ K_{xy} \end{Bmatrix} \quad \text{(B-11)}$$

Solving all of these using laminator software gives the global strain and stress developed on the laminate. The average strain value found over the lamina is shown in Table B-3 and compared with the copper specimen.

Table B-3: Comparison of average strain values of analytical model with the ALDVC.

Loading	ε_{xx}(Analytical model)	ε_{zz} (Analytical model)	ε_{xx} (ALDVC)	ε_{zz} (ALDVC)
50N	-0.0014	0.0042	-0.0058	0.0016
75N	-0.0021	0.0064	-0.0136	0.0036
100N	-0.0028	0.0085	-0.0214	0.0055

As can be seen from the Table B-3, there is a difference in the average strain calculated between the CLPT analytical model and ALDVC. This is because of all the assumptions stated above in the model, many of the factors have not been considered in the modelling. The bonding is assumed to be perfect but in actual they are imperfect. The undulations of yarns, pattern type and many more parameters has not been taken into consideration. ALDVC can plot strain map over the whole specimen layer by layer unlike the analytical model. But with the help of DVC, the

analytical model as well as the understanding of microstructure behavior can be further improved. Each of the variables for the analytical model can be studied to improve the results from model.

B.2 References

[1] C. Liu, Y. Chen, D. Shi, J. Marrow, X. Jing, and X. Yang, "In situ investigation of failure in 3D braided SiCf/SiC composites under flexural loading," *Compos. Struct.*, vol. 270, p. 114067, Aug. 2021, doi: 10.1016/J.COMPSTRUCT.2021.114067.

[2] J. Carey, A. Fahim, and M. Munro, "Predicting Elastic Constants of 2D-Braided Fiber Rigid and Elastomeric–Polymeric Matrix Composites," *http://dx.doi.org/10.1177/0731684404041715*, vol. 23, no. 17, pp. 1845–1857, Aug. 2016, doi: 10.1177/0731684404041715.

[3] G. Ghamkhar, M. S. Johari, H. H. Toudeshky, and M. Bodaghi, "An experimentally validated model for predicting the tensile modulus of tubular biaxial and triaxial hybrid braids," *Polym. Compos.*, Oct. 2022, doi: 10.1002/PC.27079.

[4] I. M. Daniel and O. Ishai, *Engineering mechanics of composite materials* , 2nd ed. New York: Oxford University Press, 2006.

[5] P. Parajuli *et al.*, "Mechanical characterization of bulk Sylgard 184 for microfluidics and microengineering Spincoat-fabricated multilayer PDMS-phosphor composites for thermometry Mechanical characterization of bulk Sylgard 184 for microfluidics and microengineering," *OPEN ACCESS J. Micromechanics Microengineering J. Micromech. Microeng*, vol. 24, p. 7, 2014, doi: 10.1088/0960-1317/24/3/035017.

[6] A. Müller, M. C. Wapler, and U. Wallrabe, "A quick and accurate method to determine the Poisson's ratio and the coefficient of thermal expansion of PDMS," *Soft Matter*, vol. 15, no.

4, pp. 779–784, Jan. 2019, doi: 10.1039/C8SM02105H.

[7] R. Talreja, “Composites: Polymer–Polymer,” *Encycl. Condens. Matter Phys.*, pp. 208–211, Jan. 2005, doi: 10.1016/B0-12-369401-9/00546-5.